UNIVERSITY OF CALIFORNIA, SAN DIEGO

Processing, Dynamic Deformation and Fragmentation of Heterogeneous Materials

(Aluminum-Tungsten Composites and Aluminum-Nickel Laminates)

A dissertation submitted in partial satisfaction of the requirements

for the degree of Doctor of Philosophy

in

Materials Sciences and Engineering

by

Po-Hsun Chiu

Committee in charge:

Professor Vitali F. Nesterenko, Chair
Professor Prabhakar R. Bandaru
Professor David J. Benson
Professor Renkun Chen
Professor Vlado A. Lubarda

2014

This Dissertation of Po-Hsun Chiu is approved and it is acceptable in quality and form for publication on microfilm and electronically:

Chair

University of California, San Diego

2014

TABLE OF CONTENTS

Signature Page iii

Table of Contents iv

List of Figures vii

List of Tables xv

Acknowledgements xvi

Vita xviii

Abstract of the Dissertation xx

Chapter 1 Introduction 1

Chapter 2 Background 7

2.1 Aluminum Matrix Composites as Reactive Materials 7

2.1.1 Synthesize of Aluminum Matrix Composites 8

2.1.2 Al-W Composites 12

2.1.3 Al-Ni Laminates 13

2.2 Combustion of Al Particles 15

2.3 Al-Ni Intermetallic Reactions 19

References 20

Chapter 3 Experimental Techniques 29

3.1 Sample Preparation 30

3.1.1 Al-W Composites 30
3.1.2 Al-Ni Laminates 32
3.1.3 Ball Milling 33
3.1.4 Cold Isostatic Pressing 34
3.1.5 Hot Isostatic Pressing 37
3.1.6 Annealing 39
3.2 Mechanical Testing 40
3.2.1 Quasi-static Compression Testing 40
3.2.2 Split Hopkinson Pressure Bar Compression Testing 41
3.2.3 Drop-weight Testing 43
3.2.4 Explosively Driven Fragmentation Tests 47
3.2.5 Thick-Walled Cylinder (TWC) Method 48
3.3 Characterization 51
3.3.1 High Speed Photography 51
3.3.2 Optical Microscopy (OM) 52
3.3.3 Scanning Electron Microscopy (SEM) 52
3.3.4 Microhardness Testing 54
3.3.5 X-ray Powder Diffraction 55
3.3.6 Particle Size Analysis-Laser Diffraction 57
Reference 59
Chapter 4 Results and Discussion 63
4.1 Al-W Particulate-reinforced Composites 63

4.1.1 Sample Preparation 63
4.1.2 Quasistatic Tests 68
4.1.3 Split Hopkinson Pressure Bar Compression Tests 69
4.1.4 Drop-weight Testing 71
4.1.5 Summary 78
4.2 Al-W Fiber-reinforced Composites 78
4.2.1 Sample Preparation 78
4.2.2 Quasistatic Tests 82
4.2.3 Split Hopkinson Pressure Bar Compression Tests 85
4.2.4 Drop-weight Testing 87
4.2.5 Explosively Driven Fragmentation Tests 92
4.2.6 Summary 103
4.3 Concentric Al-Ni Laminates 104
4.3.1 Sample Preparation 104
4.3.2 TWC Methods 107
4.3.3 Summary 117
4.4 Corrugated Al-Ni Laminates 118
4.4.1 Sample Preparation 118
4.4.2 TWC Methods 120
4.4.3 Summary 138
References 140
Chapter 5 Conclusions 145

LIST OF FIGURES

Figure 2.1 The illustration of the diffusion bonding process fabricating metal matrix composites. 10

Figure 2.2 Formation of metal powder by gas atomization [47]. 11

Figure 2.3 Phase diagram of Al-W system [55]. 13

Figure 2.4 Phase diagram of Al-Ni system [55]. 14

Figure 2.5 Al particles burning time versus particle diameters measured under various test techniques and conditions [54]. 17

Figure 3.1 The schematic diagram of strain rate regimes (in reciprocal seconds) and the techniques that have been developed for obtaining them. [1] 30

Figure 3.2 Types of investigated samples with different mesostructure 32

Figure 3.3 Illustrations of CIPing encapsulation for pressure assisted processing of heterogeneous materials; 36

Figure 3.4 Some examples of CIPed samples and the spacing between two black lines in the bottom rulers is 1mm: 37

Figure 3.5 (a) A schematic of the HIPing encapsulation to process hollow cylinder samples; (b) The cabinet style ABB Hot Isostatic Press. 39

Figure 3.6 The VAC OC-1 vacuum oven for annealing process 40

Figure 3.7 Illustration of striker bar, incident bar, transmitted bar, and sample in a split Hopkinson bar experiment with the high speed camera [8]. 42

Figure 3.8 Typical input, reflected, and transmitted signals from a split Hopkinson bar experiment [1]. 42

Figure 3.9 A Schematic diagram demonstrate the setup of the “soft” drop-weight testing [20]. 45

Figure 3.10 (a) Output signal of a PTFE-Al-W granular/porous composite tested in the conventional drop-weight test, the oscillatory noise is comparable to the signal of interest; (b) Output signal of a similar material tested in the “soft” drop-weight testing, the oscillatory noise significantly reduced compared to (a) [19]. 45

Figure 3.11 Instron DYNATUP 9250HV impact test instrument. 47

Figure 3.12 The schematic diagram shows the experimental setup of the explosively driven fragmentation tests performed in Cavendish Laboratory, Cambridge University, United Kingdom [21]. 48

Figure 3.13 Experimental setup of thick-walled cylinder (TWC) method [23]. The specimen is sandwiched between a thick Cu outer tube and a thin Cu inner tube. The outer Cu tube (driver tube) is accelerated by an explosive charge and axisymmetrically drives the radial collapse of the specimen. 49

Figure 3.14 The pure shear deformation of an element under axisymmetrically-driven, radial collapse in TWC test, r_i and r_f are its initial and final radii, respectively [23]. 50

Figure 3.15 Phantom V12 high speed camera operated during the drop weight test. 52

Figure 3.16 A diagram of the basic components of the scanning electron microscope [33].... 53

Figure 3.17 Schematic view of the indenter (pyramidal diamond with the square base) used in Vickers hardness tester and the resulting indentation on the specimen. [34]..... 55

Figure 3.18 Schematic of X-ray diffractometer [35]. 56

Figure 3.19 Diffraction of X-ray beams by a crystalline structure is described by the Bragg’s law [35]. 57

Figure 3.20 Scattering of a laser beam from large and small particles. [36]..... 58

Figure 4.1 SEM (BSE) images of the Al-coarse W CIPed only sample after 3 hours in the vacuum oven at 550°C. Intermetallic reaction between Al-W was found and locations X_1-X_8 is

where the EDX analysis was conduct showing W-rich (X_1-X_4) and Al-rich (X_5-X_8) reaction product with multiple cracks. 65

Figure 4.2 The HIP cycle for fabricating Al-W CIPed+HIPed samples. 66

Figure 4.3 The optical microstructure of (a) Al-coarse W; (b) Al-fine W CIPed only samples. 66

Figure 4.4 (a) SEM micrographs of (a) Al-coarse W; (b) Al-fine W CIPed only samples. 67

Figure 4.5 SEM micrographs of Al-coarse W particulate-reinforced granular/porous composites after different processing conditions: (a) CIPed at 48 MPa; (b) CIPed at 345 MPa and (c) CIPed at 345 MPa and HIPed at 200 MPa and 500°C for 25 minutes. 68

Figure 4.6 Stress-strain curves of CIPed-only, Al-W particulate-reinforced granular/porous composites after quasistatic tests. 69

Figure 4.7 Results of CIPed-only, Al-W particulate-reinforced granular/porous composites after Split Hopkinson Pressure Bar Tests. 70

Figure 4.8 Engineering stress and time curves for CIPed only, coarse and fine W-reinforced Al porous/granular composites at the similar porosity. The drop weight velocity is about 3m/s. 72

Figure 4.9 Series of high speed images of samples during drop weight tests at 0.5ms interval: (a) to (c): Al-fine W samples and (d) to (f): higher-porosity Al-coarse W samples. 72

Figure 4.10 Engineering stress and time curves for CIPed+HIPed, coarse and fine W-reinforced Al porous/granular composites and CIPed only, Al-coarse W samples. The drop weight velocity is about 7m/s. 73

Figure 4.11 Series of high speed images of samples during drop weight tests at the 0.5ms interval: (a) to (c): Al-fine W samples CIPed+HIPed, (d) to (f): Al-coarse W samples CIPed+HIPed, and (g) to (i), Al-coarse W samples CIPed only samples. 73

Figure 4.12 SEM micrographs of Al-coarse W samples after drop weight tests, (a) CIPed only and (b) CIPed+HIPed White particles are W and dark gray particles are Al. 75

Figure 4.13 SEM micrographs of CIPed only Al-fine W samples after drop weight tests. One of the force chains between the fine W particles observed inside the macrocrack was shown in larger magnification. White particles are W and dark gray particles are Al. 76

Figure 4.14 SEM micrographs of CIPed+HIPed only Al-fine W samples after drop weight tests. One of the force chains between the fine W particles observed inside the macrocrack was shown in larger magnification. White particles are W and dark gray particles are Al..... 77

Figure 4.15 (a) Tungsten wires required for one sample randomly distributed inside a glass tube with 15 mm diameter, similar to the sample diameter; (b) sample after CIPing; (c) sample after CIPing and HIPing. 79

Figure 4.16 Side view (a), front view (b) and (c) microstructure of the sample after two HIPing cycles. No reaction between Al and W was found after processing 81

Figure 4.17 Stress-strain curves of Al-W wires composite with CIPed Only and CIPed+HIPed after quasistatic tests..... 83

Figure 4.18 (a) The CIPed only sample after quasistatic tests with strain=0.50; (b) the cross section of the sample. No visible shear cracks were developed at this strain. 84

Figure 4.19 (a) The CIPed+HIPed sample after quasistatic tests with strain=0.51; (b) the cross section of the sample. Shear cracks were well developed at this strain in a sharp contrast with the CIPed only sample..... 84

Figure 4.20 The microstructure of the CIPed only sample (a) before quasistatic tests; (b) after quasistatic tests. Pores inside the Al matrix were compacted and closed, which led to the densification of the sample. 84

Figure 4.21 The microstructure of the CIPed+HIPed sample (a) before quasistatic tests; (b) after quasistatic tests. The aluminum matrix was deformed heavily and began to separate, which led to shear cracks..... 85

Figure 4.22 High speed images of Samples 1, 2, 3 and Samples H1, H2 H3 samples during Hopkinson Bar Tests. 86

Figure 4.23 Stress-strain (a) and strain rate-strain (b) curves of Samples 1, 2, 3 and Samples H1, H2 H3 under dynamic loading. Samples with higher hardness of Al matrix (Samples H1, H2 H3) demonstrated higher compressive strength and lower strain rate. 86

Figure 4.24 The stress-time curve of the CIPed only and CIPed+HIPed samples after drop weight tests. 87

Figure 4.25. Series of high speed images of samples during drop weight tests at 1ms interval: (a) to (c): Al- W wires CIPed only and (d) to (f): Al- W wires CIPed+HIPed samples. Pulverization of Al matrix can be observed in CIPed only samples and shear macrocracks can be seen in CIPed+HIPed samples. 88

Figure 4.26 (a) The CIPed only sample after drop weight tests with engineering strain 0.46; (b) the cross section of the sample. No visible shear cracks were developed at this strain. 89

Figure 4.27 (a) The CIPed+HIPed sample after drop weight tests with engineering strain 0.57; (b) the cross section of the sample. Shear cracks were developed at this strain. 89

Figure 4.28 The microstructure of the CIPed only sample (a) before drop weight tests; (b) after drop weight tests. Similar to quasistatic tests, pores inside the Al matrix were compacted and closed, which led to the densification of the sample. Yet shear microcracks began to develop between tungsten rods at this strain (0.46). 90

Figure 4.29 The microstructure of the CIPed+HIPed sample (a) before drop weight tests; (b) after drop weight tests. Similar to quasistatic tests, the Al matrix was deformed heavily and began to separate, which led to shear cracks. 90

Figure 4.30 The SEM image of the CIPed only sample: (a) before the drop weight test, and (b) after the drop weight test. Many pores in the Al matrix after CIPing were closed after drop weight tests. Besides the densification of Al matrix, some elongated and deformed Al particles can be observed. 91

Figure 4.31 The SEM image of the CIPed+HIPed sample: (a) before the drop weight test, and (b) after the drop weight test. The Al particles were not heavily deformed after CIPing and HIPing in comparison with high strain deformation after drop weight tests. 91

Figure 4.32 (a) One of the Al-W granular/porous composite rings before the test; (b) The fragments collected from one of the small rings (fine Al-W powder, CIPed only); (c) The SS 304 fragments after the test. 93

Figure 4.33 The PDV records of the small ring tests with SS304 and the CIPed Al-W samples with fine Al/coarse W powder as well as results of numerical simulations of Al/W samples; and 94

Figure 4.34 (a) the particle size distribution of the recovered fragments from the small-rings sample 1 and 2 (fine Al/coarse W powder composites). (b) the XRPD results of the small-ring sample 1 and 2. No intermetallic reaction between Al and W was found after tests. 95

Figure 4.35 The PDV records of samples with Al powder and W rods show similar free surface velocity profiles in all samples. 96

Figure 4.36 The XRD results of recovered fragments from (a) coarse Al-W wires, CIPed only and CIPed+HIPed; and (b) fine Al-W wires, CIPed only and CIPed+HIPed. They indicated that no intermetallic reaction occurred during tests. 97

Figure 4.37 The fragment size distribution of the recovered fragments from samples with W rods and (a) coarse (b) fine Al powder. The as-received coarse and fine Al powder were also analyzed and presented..... 98

Figure 4.38 SEM images of the CIPed only fine Al/coarse W powder sample: (a) before the test, and (b) one of the recovered fragments after the dynamic testing of the samples..... 99

Figure 4.39 SEM images of the CIPed only coarse Al-W rods sample: (a) before the test, and (b) one of the recovered fragments after the dynamic testing of the samples. 100

Figure 4.40 SEM images of the CIPed+HIPed coarse Al-W rods sample: (a) before the test, and (b) one of the recovered fragments after the dynamic testing of the samples. 100

Figure 4.41 SEM images of the CIPed only fine Al-W rods sample: (a) before the test, and (b) one of the recovered fragments after the dynamic testing of the samples..... 101

Figure 4.42 SEM images of the CIPed+HIPed fine Al-W rods sample: (a) before the test, and (b) one of the recovered fragments after the dynamic testing of the samples. 101

Figure 4.43 Al-Ni laminate cylinder samples with different mesostructures after pressure-assisted processing (CIPing) prior to dynamic testing. 105

Figure 4.44 Experimental setup for Thick Walled Cylinder Method..... 108

Figure 4.45 Global view of collapsed Ni-Al laminate cylindrical samples. The nearly cylindrical shape of the outer interface was maintained ensuring the global symmetry of plane strain deformation despite large variations in the mesostructures of the various samples.... 109

Figure 4.46 (a) the SEM image of the similar sample after the TWC testing where Ni is white and Al is gray. The red square indicates the area with the local reaction shown at larger magnification in (b). (b) Intermetallic reactions at the Ni and Al interface were observed at the outer apex regions of the buckling Ni foil. 111

Figure 4.47 (a) The mesostructure of the simulated partially collapsed concentric Al-Ni sample where Ni is blue and Al is red. It demonstrates the development of the instability in the inner layers; (b) the mesostructure of the laminated collapsed TWC sample (Al (red) and Ni (blue)) generated in the numerical simulations. 112

Figure 4.48 The influence of the layer size on the mechanism of plastic strain accommodation. (a) The mesostructure of Sample 2 with bilayer thickness 18.5 micron at different magnifications. (b) The mesostructure in Sample 3A with bilayer thickness 620 micron..... 114

Figure 4.49 Influence of the layer size on the mechanism of plastic strain accommodation in a fully bonded laminate in numerical simulations with the corresponding layer thicknesses similar to Figure 4.48. The deformed geometries are shown in (a) and (c) and the corresponding fringes of plastic strain in (b) and (d). 116

Figure 4.50 (a) The mesostructure of the Sample 3B in the region near one of the defects in the inner layer. The defect has influenced a deformation pattern only local region. Its size is similar to the size of the initial defect which is reflected in the deformed geometry (b) and in the corresponding fringes of plastic strains (c) in the simulated collapse of Sample 3B. 117

Figure 4.51 Cross-sectional micrographs of the swaged Ni-Al laminate tubes (a) SW-6A and (b) SW-7A before the TWC test. The higher magnification images, (c) and (d), correspond to SW-6A and SW-7A, respectively. The Ni and Al layers had a nominal thickness of 20 and 30 microns, respectively, in each sample and appear as white and dark grey, respectively.. 119

Figure 4.52 (a) The experimental setup for Thick Walled Cylinder Method [19], (b) a detailed view of the collapsed sample, and (c) the explosively sealed cavity. 121

Figure 4.53 Axial slices of the collapsed samples showing axial symmetry of the outside surface of deformed samples, similar maximum strains (0.69-0.71), and similar features on the inner surface (wedge extrusion).. 125

Figure 4.54 Two mesoscale mechanisms of the deformation accommodation in collapsed laminates samples – wedge extrusions and trans-layer shear bands spanning only a few layers are shown in (a), SW-6B and (b), SW-7C; a detailed view of the trans-layer shear band in SW-7A is shown in (c) and (d). 127

Figure 4.55 A detailed view of a local reacted trans-layer shear band in sample SW-6B (location is boxed in red). (b) A detailed view of the locations X1-X10 in the sample SW-6B (blue boxed region) where the EDX analysis was conducted showing Al-rich (X1-X4), Ni-rich (X5-X8), and Ni-Al (X9-X10) reaction products..... 129

Figure 4.56 Bent and deformed Ni layers (compare the geometry of Ni layers in the initial sample in Figure 4.51 (b)), showing melting and localized reaction at the interface with copper stopper tube. 130

Figure 4.57 (a) Examples of localized reaction in some of the extruded wedge-shaped regions in SW-6 C (regions in the red boxes) showing the presence of an intermetallic reaction and (b) a reacted wedge in SW-6B with locations for EDX analysis identified..... 131

Figure 4.58 The deformed mesostructure (a) showing the three major mechanisms of plastic strain accommodation: (1) the extrusion of wedged shaped regions outlined by the orange dashed line, (2) the development of trans-layer shear bands outlined by the green dashed line, and (3) the cooperative buckling shown in the area outlined by the yellow dashed box. 134

Figure 4.59 Comparison of elongated Al and Ni layers observed inside the trans-layer shear bands in the numerical simulation (a) and the experimental result corresponding to sample SW-7A (b). This elongation process may be the initial stage in the initiation of reaction within the shear bands shown in Figure 4.54(b) and Figure 4.55(a) [39]..... 135

LIST OF TABLES

Table 3.1 Characteristics of commercial powders and wire used in the research. 31

Table 4.1 Experimental results of sample properties after processing. 64

Table 4.2 Properties of Al-W wires samples after processing. 79

Table 4.3 Properties of solid Al-W wire mesh samples before dynamic testing. 82

Table 4.4 Microhardness of the Al matrix at each stage (as-received, before and after testing). 88

Table 4.5 Dimensions of the TWC samples before the TWC experiments. 120

Table 4.6 Dimensions of the TWC samples and effective strains after the TWC experiments. 122

ACKNOWLEDGEMENTS

My sincere gratitude goes to my advisor, Professor Vitali F. Nesterenko for his support, guidance and encouragement. His passion, prudence, and perseverance toward science greatly influence me professionally and personally. I am also grateful to my committee members, Professor Bandaru, Professor Benson, Professor Chen and Professor Lubarda for their comments and suggestions. I am especially indebted to Professor Lubarda for the opportunities he gave to work and learn as his teaching assistant.

The funding for the major part of this research is provided by the Office of Naval Research. Their support is highly appreciated. I would also like to acknowledge all my collaborators and coauthors, especially Dr. Karl Olney, Carl Lucchese, Kevin Gott, Dr. Chung-Ting Wei, Ryan Anderson, Dr. Fengchun Jiang, Dr. Chris Braithwaite, Matthew Serge and Professor Andrew Higgins. Without their help and contribution, this research would not be successful.

Chapter 1 contains part of the materials published in the paper DYMAT 9th International Conference on the Mechanical and Physical Behaviour of Materials under Dynamic Loading (2009) by Po-Hsun Chiu and V. F. Nesterenko and in Applied Physics Letters 102 (24) (2013) by Po-Hsun Chiu, K. L. Olney, A. J. Higgins, M. Serge, D. J. Benson, and V. F. Nesterenko. The dissertation author was the investigator and author of above papers.

Chapter 4 and 5 contains materials that appear in DYMAT 9th International Conference on the Mechanical and Physical Behaviour of Materials under Dynamic

Loading (2009) by Po-Hsun Chiu and V. F. Nesterenko, in AIP Conference Proceedings 1426 (1) (2012) by Po-Hsun Chiu, C.W. Lee, and V. F. Nesterenko, in Journal of Physics Conference Series 500 (11) (2014) by Po-Hsun Chiu, K. L. Olney, C. Braithwaite, A. Jardine, A. Collins, D. J. Benson, and V. F. Nesterenko, in Applied Physics Letters 102 (24) (2013) by Po-Hsun Chiu, K. L. Olney, A. J. Higgins, M. Serge, D. J. Benson, and V. F. Nesterenko, and in Philosophical Magazine 94 (26) (2014) by K. L. Olney, Po-Hsun Chiu, A. Higgins, M. Serge, T. P. Weihs, G. M. Fritz, A. K. Stover, D. J. Benson, and V. F. Nesterenko. The dissertation author was the investigator and author of above papers.

I would like to thank my friends and family, especially my parents, for their support and encouragement. I am deeply grateful for the endless motivation and inspiration from my wife, Hsiu-Pin Chen. Without her, I would not be able to accomplish this work. Last but not least, I would like to thank my daughter, Nina, for bringing me not only troubles, but also greater happiness to keep me going during difficult times.

VITA

2014	Doctor of Philosophy, University of California, San Diego, La Jolla, CA
2008 - 2014	Research Assistant, University of California, San Diego, La Jolla, CA
2008 - 2012	Teaching Assistant, University of California, San Diego, La Jolla, CA
2004	Master of Science, University of Southern California, Los Angeles, CA
2000	Bachelor of Science, National Cheng Kung University, Tainan, Taiwan

PUBLICATIONS

Po-Hsun Chiu and V.F. Nesterenko, "Dynamic behavior and fracture of granular composite Al-W", DYMAT 2009, EPD Sciences, pp. 947-953 (2009). (DOI: 10.1051/dymat/2009133).

Po-Hsun Chiu, S. Wang, E. Vitali, E.B. Herbold, D.J. Benson, and V.F. Nesterenko, "Particle size effect in granular composite aluminum/tungsten", in *Shock Compression of Condensed Matter - 2009*, edited by M.L. Elert, W.T. Buttler, M.D. Furnish, W.W. Anderson, and W.G. Proud (American Institute of Physics, Melville, NY, 2009), pp. 1345-1348.

K. L. Olney, Po-Hsun Chiu, C. W. Lee, V. F. Nesterenko, and D. J. Benson, "Role of material properties and mesostructure on dynamic deformation and shear instability in Al-W granular composites," J Appl Phys **110** (11), 114908 (2011).

C.H. Braithwaite, A.L. Collins, B. Aydelotte, F. McKenzie, Po-Hsun Chiu, N. Thadhani, and V.F. Nesterenko, "Advances in the study of novel energetic materials," Proc. 15th Seminar New Trends in Research of Energetic Materials, University of Pardubice, Czech Republic, 93-99 (2012).

Po-Hsun Chiu, C.W. Lee, and V. F. Nesterenko, "Processing and dynamic testing of Al/W granular composites," AIP Conference Proceedings 1426 (1), 737-740 (2012).

V. F. Nesterenko, Po-Hsun Chiu, C.H. Braithwaite, A. Collins, D. M. Williamson, K. L. Olney, D. Benson, and F. McKenzie, "Dynamic behavior of particulate/porous energetic materials," AIP Conference Proceedings 1426 (1), 533-538 (2012).

K. L. Olney, Po-Hsun Chiu, V. F. Nesterenko, D. J. Benson, C. Braithwaite, A. Collins, D. Williamson, and F. McKenzie, "The Fragmentation of Al-W Granular Composites Under Explosive Loading," MRS Proceedings 1521 (2012, Boston, Massachusetts.).

Po-Hsun Chiu, K. L. Olney, A. J. Higgins, M. Serge, D. J. Benson, and V. F. Nesterenko, "The mechanism of instability and localized reaction in the explosively driven collapse of thick walled Ni-Al laminate cylinders," Appl Phys Lett 102 (24) (2013).

K. Olney, Po-Hsun Chiu, C. Braithwaite, A. Jardine, A. Collins, D. Benson, and V. Nesterenko, "Fragmentation of explosively driven Al-W granular composite rings," Bulletin of the American Physical Society (2013).

Po-Hsun Chiu, K. L. Olney, C. Braithwaite, A. Jardine, A. Collins, D. J. Benson, and V. F. Nesterenko, "Mechanisms of fragmentation and microstructure of debris generated during explosive testing of Al-W granular composite rings," Journal of Physics Conference Series 500 (11), 112017 (2014).

K. L. Olney, Po-Hsun Chiu, A. J. Higgins, M. Serge, T. P. Weihs, G. Fritz, A. Stover, D. J. Benson, and V. F. Nesterenko, "Mechanisms of large strain, high strain rate plastic flow in the explosively driven collapse of Ni-Al laminate cylinders," Journal of Physics Conference Series 500 (13), 132002 (2014).

M. Serge, Po-Hsun Chiu, A. J. Higgins, and V. F. Nesterenko, "Reactivity of Ti-B, Cr-S, and Mn-S powder systems during explosively-driven collapse," Journal of Physics Conference Series 500 (18), 182039 (2014).

K. L. Olney, Po-Hsun Chiu, A. J. Higgins, M. Serge, T. P. Weihs, G. M. Fritz, A. K. Stover, D. J. Benson, and V. F. Nesterenko, "The mechanisms of plastic strain accommodation during the high strain rate collapse of corrugated Ni-Al laminate cylinders," Philosophical Magazine, 94 (26) (2014).

K.L. Olney, P.-H. Chiu, D.J. Benson, A. Higgins, M. Serge, V.F Nesterenko, "Localized microjetting in the collapse of surface macrocavities", submitted to Phys. Rev. E.

K.L. Olney, P.-H. Chiu, M.S. Ribero Vairo, A. Higgins, M. Serge, D.J. Benson, V.F. Nesterenko, "Influence of mesoscale properties on the mechanisms of plastic strain accommodation in plane strain dynamic deformation of concentric Ni-Al laminates", submitted to Journal of Applied Physics.

ABSTRACT OF THE DISSERTATION

Processing, Dynamic Deformation and Fragmentation of Heterogeneous Materials

(Aluminum-Tungsten Composites and Aluminum-Nickel Laminates)

by

Po-Hsun Chiu

Doctor of Philosophy in Materials Sciences and Engineering

University of California, San Diego, 2014

Professor Vitali F. Nesterenko, Chair

Two types of heterogeneous reactive materials, Aluminum-Tungsten composites and Aluminum-Nickel laminates were investigated. The current interest in these materials is their ability to combine the high strength and energy output under critical condition of the mechanical deformation which may include their fragmentation. Mesoscale properties of reactive materials are very important for the generation of local hot spots to ignite reactions and generate critical size of debris suitable for fast oxidation kinetics. Samples with different mesostructures (e.g., coarse vs. fine W particles, bonded vs. non-bonded Al particles, W particles vs. W wires and

concentric vs. corrugated Al-Ni laminates) were prepared by Cold Isostatic Pressing, Hot Isostatic Pressing and Swaging. Several dynamic tests were utilized including Split Hopkinson Pressure Bar, Drop Weight Test, Explosively Driven Fragmentation Test, and Thick-Walled Cylinder Method. A high speed camera was used to record images of the *in situ* behavior of materials under dynamic loading. Pre- and post-experiment analyses and characterization were done using Optical Microscopy, Scanning Electron Microscopy, X-ray Powder Diffraction, and Laser Diffraction. The numerical simulations were conducted to monitor the *in situ* dynamic behavior of materials and elucidate the mesoscale mechanisms of the plastic strain accommodation under high-strain, high-strain-rate conditions in investigated heterogeneous m aterials.

Several interesting results should be specifically mentioned. They include observation that the fracture and dynamic properties of the Al-W composites are sensitive to porosity of samples, particles sizes of rigid inclusions (W particles or wires), and bonding strength between Al particles in the matrix. Soft Al particles were heavily deformed between the rigid W particles/wires during dynamic tests. Three plastic strain accommodation mechanisms are observed in Al-Ni laminates. They depend on the initial mesostructure and act to block the development of periodic patterns of multiple shear bands that have been observed previously in homogeneous solids and granular materials.

CHAPTER 1 INTRODUCTION

Energetic materials (EMs) are generally defined as materials which are capable of releasing the chemical energy stored in the molecular building blocks in a controlled practice. Reactive materials (RMs) are energetic materials that generally combine two or more non-explosive solids forming a thermo-chemical mixture together. They offer a wide range of application, for example, biological agent defeat, material destruction, countermeasure and so on. Unlike traditional energetic materials, which have minimal strength, structural reactive materials are also required to have significant mechanical strength and sometimes a high density. This new class of energetic materials is tailored to survive the launch and release enthalpic energy under highly dynamic loads, yet they should be insensitive enough to ship and carry around. This requirement brings the fundamental challenge on how to combine the high strength materials with the ability to undergo the controlled bulk disintegration to produce small-sized reactive fragments [1].

For optimized performance of reactive materials, the mechanical properties and fragmentation of granular composites are very important [1]**.** A close link between the dynamic mechanical properties and ignition responses to impacts was established in [2] for ammonium perchlorate (AP)-based propellants. It was shown in Hopkinson bar experiments that the dynamic flow strength of AP plus HTPB compositions depends on the particle size of AP, increasing with the decreasing particle size and following the linear dependence of the flow strength on the reciprocal of the square

root of the grain size of AP. The similar effect of the particle size on strength of RDX/HTPB compositions was reported in [3, 4]. It was mentioned in [2, 3] that the mechanism of this phenomenon may be related to the way cracks propagate through these composite materials – larger interfacial area between smaller particles and matrix provide a longer path for fracture. This mechanism is similar to the one proposed in paper [5] related to the quasistatic behavior of the polymer based explosive PBX 9501.

The sensitivity of the strength and fragmentation pattern to initial particle sizes of components and microstructural changes in composites with polymer matrix (PTFE) were investigated in papers [6-10]. It was shown that at relatively large strains the skeleton of small metal particles (similar to the force chain network in granular materials at small elastic strains) can significantly affect the strength of this granular composite with weak polymer matrix. In numerical calculations it was shown that these "force chains" were able to rearrange themselves in the matrix (cold isostatically pressed PTFE) creating support for the compression loads even on the stage of the partial matrix disintegration. The particle size determines not only the dynamic strength of composites, but also affects their fractures under the shock wave loading and shear localization, like in granular ceramic materials Al_2O_3 and SiC [11-14].

The presence of stress chains and the stress bridging among the high explosive particles embedded in the polymer (PBX 109) under compression was observed in [15]. Experimental observation and numerical modeling of stress bridging in two dimensional arrays of cylindrical particles under dynamic loading was presented in [16, 17]. These stress bridges resulted in cleaving of the explosive crystals during the

apparent elastic response of the bulk material, thus the ignition sites have been ascribed to the stress chain formation in granular energetic materials.

The reaction of the energetic materials can also be ignited in the hot spots formed in the shear localization zones at high strain plastic flow with relatively weak shock pressures [18-21]. The shear bands in reactive materials act as planar hot spots and they may also provide sites where the *in situ* sintering of granular ceramics can occur [14]. In metal-based reactive materials, the intermetallic reaction may be triggered in zones of highly developed localized plastic deformation where the local temperature can be approximately an order of magnitude higher than the temperatures generated during the onset of the localized plastic flow. To improve the reactivity of these materials under conditions of dynamic, high-strain plastic deformation, a mesostructure should be designed to promote the localized plastic flow because the shear localization and the formation of hot spots are necessary to initiate the reaction.

In the context of this dissertation, two types of reactive materials, Al-W composites and Al-Ni laminates will be investigated. Numerous samples with various mesoscale parameters including the particle sizes of components, the morphology of components (e.g., wires versus powder) and the bonding between particles were prepared. They were then tested by quasistatic tests, using Split Hopkinson Pressure Bar, Drop Weight Test, Explosively Driven Fragments Test, and Thick-Walled Cylinder Method. A high speed camera was used to record the *in situ* dynamic behavior of materials. With the pre- and post-experiment analyses and the assistance of numerical simulations to monitor the *in situ* dynamic behavior of materials, we hope this research can shed light on the mesoscale mechanisms of the plastic strain

accommodation and help to design materials mesostructure for their better performance.

This chapter contains part of the materials published in the paper DYMAT 9th International Conference on the Mechanical and Physical Behaviour of Materials under Dynamic Loading (2009) by Po-Hsun Chiu and V. F. Nesterenko and in Applied Physics Letters 102 (24) (2013) by Po-Hsun Chiu, K. L. Olney, A. J. Higgins, M. Serge, D. J. Benson, and V. F. Nesterenko. The dissertation author was the investigator and author of above papers.

References:

1. R. G. Ames, *Energy Release Characteristics of Impact-Initiated Energetic Materials.* Materials Research Society Symposium Proceedings, 2006. **896**: p. 10.

2. J. E. Balzer, C. R. Siviour, S. M. Walley, W. G. Proud, and J. E. Field, *Behaviour of ammonium perchlorate-based propellants and a polymer-bonded explosive under impact loading.* Proceedings of the Royal Society of London Series a-Mathematical Physical and Engineering Sciences, 2004. **460**(2043): p. 781-806.

3. C. R. Siviour, M. J. Gifford, S. M. Walley, W. G. Proud, and J. E. Field, *Particle size effects on the mechanical properties of a polymer bonded explosive.* Journal of Materials Science, 2004. **39**(4): p. 1255-1258.

4. C. R. Siviour, P. R. Laity, W. G. Proud, J. E. Field, D. Porter, P. D. Church, P. Gould, and W. Huntingdon-Thresher, *High strain rate properties of a polymer-bonded sugar: their dependence on applied and internal constraints.* Proceedings of the Royal Society a-Mathematical Physical and Engineering Sciences, 2008. **464**(2093): p. 1229-1255.

5. P. J. Rae, S. J. P. Palmer, H. T. Goldrein, J. E. Field, and A. L. Lewis, *Quasi-static studies of the deformation and failure of PBX 9501.* Proceedings of the Royal Society of London Series a-Mathematical Physical and Engineering Sciences, 2002. **458**(2025): p. 2227-2242.

6. J. Cai, S. M. Walley, R. J. A. Hunt, W. G. Proud, V. F. Nesterenko, and M. A. Meyers, *High-strain, high-strain-rate flow and failure in PTFE/Al/W granular composites.* Materials Science and Engineering A-Structural Materials Properties Microstructure and Processing, 2008. **472**(1-2): p. 308-315.

7. J. Addiss, J. Cai, S. Walley, W. Proud, and V. Nesterenko, *High strain and strain-rate behaviour of PTFE/Aluminium/Tungsten mixtures.* AIP Conference Proceedings, 2007. **955**(1): p. 773-776.

8. J. Cai, F. Jiang, K. S. Vecchio, M. A. Meyers, and V. F. Nesterenko, *Mechanical and microstructural properties of PTFE/Al/W system.* AIP Conference Proceedings, 2007. **955**(1): p. 723-726.

9. J. Cai, V. F. Nesterenko, K. S. Vecchio, F. Jiang, E. B. Herbold, D. J. Benson, J. W. Addiss, S. M. Walley, and W. G. Proud, *The influence of metallic particle size on the mechanical properties of polytetraflouroethylene-Al-W powder composites.* Applied Physics Letters, 2008. **92**(3): p. 3.

10. E. B. Herbold, V. F. Nesterenko, D. J. Benson, J. Cai, K. S. Vecchio, F. Jiang, J. W. Addiss, S. M. Walley, and W. G. Proud, *Particle size effect on strength, failure, and shock behavior in polytetrafluoroethylene-Al-W granular composite materials.* Journal of Applied Physics, 2008. **104**(10): p. 11.

11. V. F. Nesterenko, *Dynamics of Heterogeneous Materials*. First ed. Shock Wave and High Pressure Phenomena. 2001, New York: Springer. 536.

12. D. J. Benson, V. F. Nesterenko, F. Jonsdottir, and M. A. Meyers, *Quasistatic and dynamic regimes of granular material deformation under impulse loading.* Journal of the Mechanics and Physics of Solids, 1997. **45**(11-12): p. 1955-1999.

13. V. F. Nesterenko, M. A. Meyers, and H. C. Chen, *Shear localization in high-strain-rate deformation of granular alumina.* Acta Materialia, 1996. **44**(5): p. 2017-2026.

14. C. J. Shih, M. A. Meyers, and V. F. Nesterenko, *High-strain-rate deformation of granular silicon carbide.* Acta Materialia, 1998. **46**(11): p. 4037-4065.

15. J. J. C. Foster, J. G. Glenn, and M. Gunger, *Meso-scale origins of the low-pressure equation of state and high rate mechanical properties of plastic bonded explosives.* AIP Conference Proceedings, 2000. **505**(1): p. 703-706.

16. K. M. Roessig, J. C. Foster, and S. G. Bardenhagen, *Dynamic stress chain formation in a two-dimensional particle bed.* Experimental Mechanics, 2002. **42**(3): p. 329-337.

17. S. G. Bardenhagen and J. U. Brackbill, *Dynamic stress bridging in granular material.* Journal of Applied Physics, 1998. **83**(11): p. 5732-5740.

18. J. E. Field, *Hot-Spot Ignition Mechanisms for Explosives.* Accounts of Chemical Research, 1992. **25**(11): p. 489-496.

19. V. F. Nesterenko, M. A. Meyers, H. C. Chen, and J. C. Lasalvia, *Controlled High-Rate Localized Sheer in Porous Reactive Media.* Applied Physics Letters, 1994. **65**(24): p. 3069-3071.

20. V. F. Nesterenko, M. A. Meyers, H. C. Chen, and J. C. Lasalvia, *The Structure of Controlled Shear Bands in Dynamically Deformed Reactive Mixtures.* Metallurgical and Materials Transactions A-Physical Metallurgy and Materials Science, 1995. **26**(10): p. 2511-2519.

21. H. C. Chen, V. F. Nesterenko, and M. A. Meyers, *Shear localization and chemical reaction in Ti-Si and Nb-Si powder mixtures: Thermochemical analysis.* Journal of Applied Physics, 1998. **84**(6): p. 3098-3106.

CHAPTER 2 BACKGROUND

A reactive material can be ignited by different types of impulses (e.g., chemical, electrical, mechanical and thermal). Each type of ignition is unique and will significantly influence the reaction kinetics. This dissertation will focus on the mechanical shock loading generated from the dynamic tests. Mesoscale features like particle sizes are very important for optimized performance of reactive materials [1-4]. Another mesoscale feature, reaction "hot spots" may be generated by the localized plastic flow during the dynamic loading [5-7]. Two reactive materials systems, Al-W granular/porous composites and Al-Ni laminates, are selected. The type of reaction we would like to achieve is the Al combustion for Al-W granular/porous composites and the Al-Ni intermetallic reaction for Al-Ni laminates. Details of the Al combustion and Al-Ni intermetallic reaction will be discussed in Section 2.2 and 2.3, respectively.

2.1 Aluminum Matrix Composites as Reactive Materials

Metal Matrix Composites (MMCs) are popular topics of research for decades because their mesostructure can be tailored to meet specific application. Light-weight aluminum (Al, density = 2.70 g/cc) is a particular favorite choice for matrix. Their improved strength, modulus and wear resistance over conventional Al alloys make them attractive especially in aerospace, automobile and defense industries despite their higher manufacturing costs. Al is also known for its drastic enthalpic reaction with

oxygen. For the purpose of releasing a high amount of energy, this reaction can be used as a basis to create a structural reactive material.

Diverse reinforcement materials have been used in Al alloy matrix composites, such as SiC whisker (SiC_w) [8, 9] and particulate (SiC_p) [10, 11], Al_2O_3 particulate [12-14] and fiber [15, 16] and carbon fiber [17-19] depending on applications. These reinforcement materials have high strength-to-volume ratio so they can decrease the density while increase the strength of composites. However, in some applications, higher density of materials is favored, e.g., to provide the higher kinetic energy of penetrators. Tungsten (W, density = 19.25 g/cc), with its high density and hardness, can significantly increase the density and strength of the composites. Nickel (Ni, density = 8.91 g/cc) is not as heavy as W, but the high exothermicity of intermetallic reaction between Al and Ni is well-documented and has various applications [20-44].

2.1.1 Synthesize of Aluminum Matrix Composites

There are numerous processing techniques to synthesize Al matrix composites. Depending on the phase of components, the process can be classified into three groups: (a) solid state processes, (b) liquid phase processes, and (c) two phases (solid-liquid) processes. To minimize the bonding between the Al matrix and reinforced phase during fabrication, the solid state processes will be utilized in this research and reviewed in this section.

In the solid state processes metal matrix composites are fabricated as results of bonding the matrix metal and the reinforced phases with mutual diffusion occurring between them in solid state under pressure at elevated temperature, but below

temperature of ignition. Due to their low processing temperature (as compared to liquid phase processes and two phase processes), the undesirable reaction on the boundary between the matrix and reinforced phases can be avoided or depressed. There are two principal groups of solid state processes for metal matrix composites: diffusion bonding and powder metallurgy.

Diffusion bonding is a relatively simple solid-state joining process which is used to fabricate simple shape parts such as plates and tubes with a multilayer structure as shown in Figure 2.1. Generally a matrix in the form of sheets or foils and a reinforced or dispersed phase in the form of long fibers are stacked in a particular order and direction and then pressed at elevated temperature. It is controlled by three important process parameters: bonding temperature, bonding pressure and holding time [45]. The bonding temperature should be between 50 and 70% of the melting point (in absolute temperature) of either the lowest melting temperature or major phase. The use of elevated temperature will aid the inter-diffusion of atoms across the interface and assist deformation. The bonding pressure should be high enough to ensure a tight contact between the joining surfaces. Moreover, it should be sufficient to aid in the deformation of surface roughness and to fill all the voids between interfaces. Also, the holding time should be optimized to achieve the desired joint quality. It should be sufficient for an intimate contact to be formed and for the diffusion process to take place. However, excessive holding time may lead to degradation of physical and chemical properties. Diffusion bonding process parameters are interrelated and thus have an effect on each other. They can be controlled accurately with relative ease and at low cost.

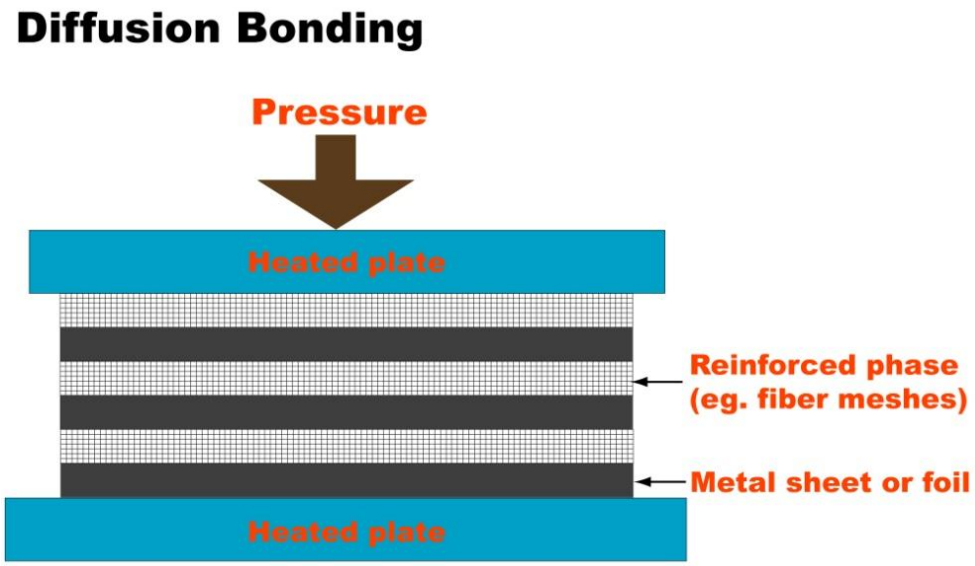

Figure 2.1 The illustration of the diffusion bonding process fabricating metal matrix composites.

Powder metallurgical products can be manufactured along different production routes, but in general the following steps can be mentioned: powder production, blending and mixing of powders with the addition of lubricants and binders, cold compaction eventually followed by sintering or hot consolidation and finally some post consolidation treatments such as machining, heat treatments, and surface treatments can be carried out to meet the dimensions and properties requirements [46].

The Al powder can be produced by a variety of manufacturing routes. The most common fabrication method for industrial scale production is atomization as shown in Figure 2.2. The formation of powder is from a molten metal jet which is broken into droplets due to interaction with high pressure gas or water. Both elemental and pre-alloyed powder can be formed. After production, powders of controlled purity and particle sizes are mixed with alloying metal powders in precisely controlled quantities. Generally, a powdered lubricant is added to minimize the wear and

facilitate the ejection from the die after compaction. This lubricant is carefully chosen to ensure that there is no residual ash to interfere with powders at later stages.

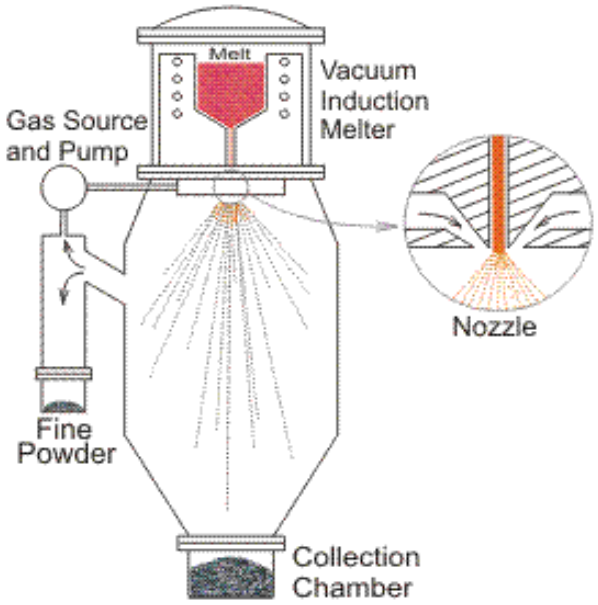

Figure 2.2 Formation of metal powder by gas atomization [47].

Cold compaction is the first step in the shaping of loose powders into the product form and providing the sufficient strength for further handling. It is mostly done by unidirectional compaction in a die or to a lesser extent by cold isostatic pressing (CIPing). Al premixes exhibit the excellent compressibility and yields the high density parts at low compaction and ejection pressures. The green compacts are then further consolidated through sintering or hot consolidation. During sintering, the green compacts are heated to a high temperature below the melting point, when the materials of separate particles diffuse to the neighboring powder particles. However, it is hard to achieve full density with a simple sintering process because some residual pores become stabilized and are difficult to remove, especially when the pores are filled with gas. On the other hand, hot consolidation involves a simultaneous action of

heat and pressure and a powder metallurgy product without residual pores can be obtained. Hot consolidation can be performed on sintered products or directly on cold compacted products. The downsides of the hot consolidation are the high cost and possible deterioration of the material properties due to the structure coarsening during the prolonged heating.

2.1.2 Al-W Composites

Many research efforts of Al/W system has been on Si-based devices since Al is the most commonly used interconnecting material and W has been used in barrier layers next to Al to prevent the diffusion [48-53]. No intermetallic reaction between sputtered-deposited W and evaporated Al was found below 500℃ [48]. The formation of the first intermetallic phase WAl_{12}, which is the most Al-rich phase on the phase diagram (Figure 2.3), is at 525℃ in a somewhat layer-by-layer fashion [51].

To utilize the high combustion energy of Al (7422 cal/g) as the reactive materials, not only the Al needed to be pulverized into less than 20 μm particle sizes to achieve sufficient short burning time (~1 millisecond, see Figure 2.5) [54], but fresh Al surface also has to be exposed during the pulverization. More details regarding the Al combustion will be discussed in Section 2.2. In this research, W is being used to provide the strength and increase the density of the composites approaching the value for steel (7.8 g/cm^3). To reach this density, the weight ratio of 23.8% Al and 76.2% W, which corresponds to the volume ratio of 69% Al and 31% W, is maintained for all Al-W granular/porous composites. This composition is shown in a red dot-line on the phase diagram (Figure 2.3).

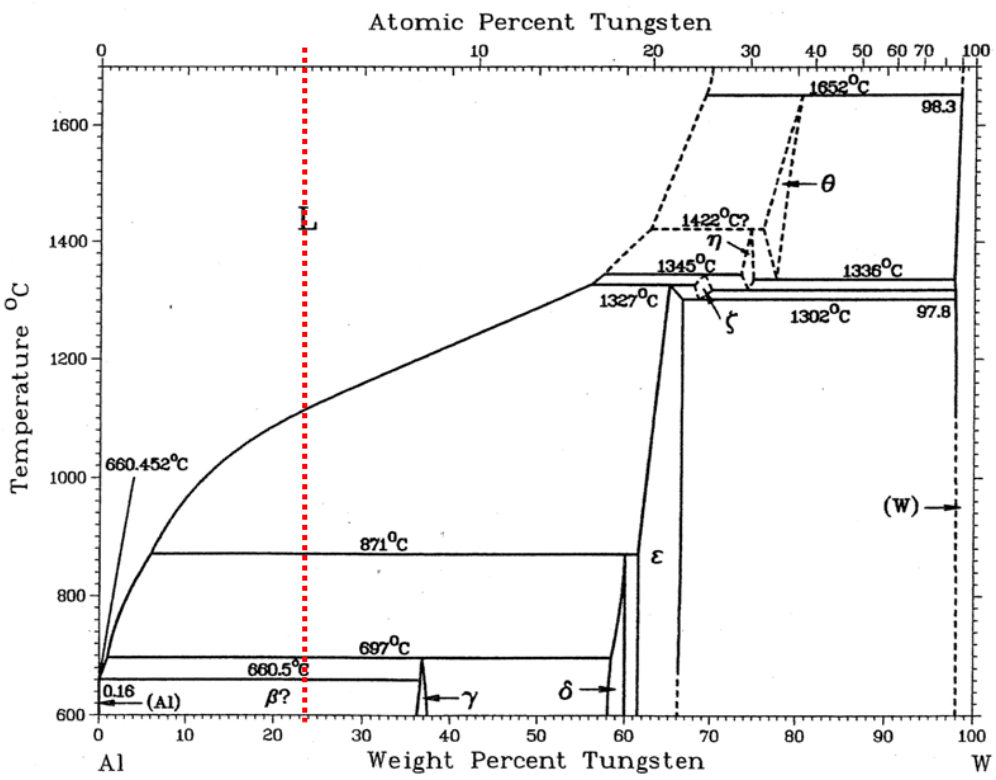

Figure 2.3 Phase diagram of Al-W system [55].

Another advantage to incorporate W is the drastic difference of the density between Al and W, which results the significantly different shock impedance. When a shock wave pass through the heterogeneous Al-W composites, the velocity gradient between Al and W may result the bulk-distributed fractures and generate the fragments on the size scale similar to the spacing between rigid W inclusions.

2.1.3 Al-Ni Laminates

There are five intermetallic compounds (Al_3Ni, Al_3Ni_2, Al_3Ni_5, AlNi and $AlNi_3$) in the Al-Ni binary system (see Figure 2.4). Both $AlNi_3$ and AlNi have received the major attention for their good high-temperature properties and corrosion

resistance. On the other hand, the Al-rich part of the system attracts less practical interest. $AlNi_3$ is known for its unique mechanical properties where the strength increases at high temperature [56]. AlNi has a higher melting point (1638℃) than $AlNi_3$ (1385℃) and is a good candidate for the shape memory alloys [57].

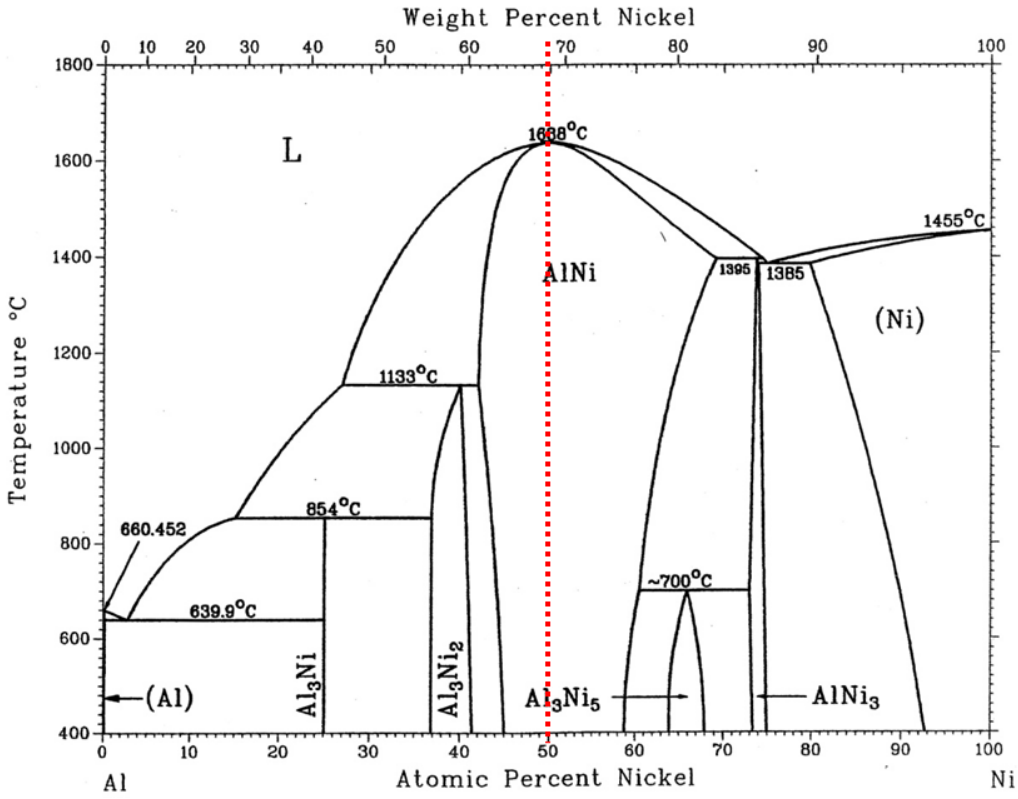

Figure 2.4 Phase diagram of Al-Ni system [55].

In this research, investigated Al-Ni laminates had the ratio of thicknesses of Al and Ni foil equal to 1.52:1 with a purpose to achieve a 1:1 stoichiometric ratio. This composition is shown in a red dot-line on the phase diagram (Figure 2.4). The intermetallic reactions between Al and Ni release large amount of heat and even can self-sustain the propagation of the reaction through the material bulk, utilizing the exothermic heat to ignite the adjacent materials. More details about the intermetallic

reactions will be presented in Section 2.3. It would be interesting to see if the dynamic loading can create mesoscale “hot spots” to initiate and sustain the self-propagating intermetallic reactions.

2.2 Combustion of Al Particles

Al particles have been shown to provide performance enhancements when used in propellant systems due to the large amount of heat released during Al combustion and the ensuing formation of alumina. The reaction is highly exothermic as shown in following equations:

$$4\,Al + 3\,O_2 \rightarrow 2Al_2O_3 \tag{2.1}$$

$$\Delta H°_{RXN} = -7422\ cal/g \tag{2.2}$$

There are several factors influencing the performance of the Al combustion, such as the initial temperature and pressure, the effect of the oxidizer, and. the burning rate of Al particles.

In an early study by Glassman [58], metal combustion was considered to be similar to diffusion-limited droplet combustion and thus the D^2 law should apply. This predicts that the time for a single Al particle to combust completely determined by the initial squared diameter. Moreover, for the same oxidizer, the combustion time is relatively independent of ambient pressure and temperature as shown in experiments [59]. These works have provided a general framework for understanding Al combustion. However, Al combustion cannot be analyzed with a simple hydrocarbon

droplet combustion model. This is due to the complications within the combustion, which takes place in the three-stage process [60].

At first stage, the gas phase combustion products condense to liquid aluminum oxide and deposit on the Al particle surface to form an oxide cap. This condensation dominates the combustion process and contributes considerably to the amount of heat released during combustion. At second stage, due to the difference of the thermal expansion coefficients between Al and alumina (α_{Al}= $29x10^{-6}$ and $\alpha_{Al_2O_3}$=$8.7x10^{-6}$), even at low temperature (<100 ^{o}C), the oxide cap begins to crack [61]. This causes jetting and fragmentation of the particle and therefore distorts the distribution of gasification velocity, temperature and other quantities around the particle. At final stage, the forming and dissociation of the condensed product repeat until most of the Al within the original particle has reacted. This repeating process maintains the flame temperature fairly constant at the gasification temperature of the aluminum oxide and thus becomes hot gas.

Later researches have suggested the D^n law for burning time, where nominal values of n vary from 1.2 to 1.8 [61-65]. There are several explanations for this deviation of exponent from the value 2, including convection effect, the formation and accumulation of the aluminum oxide, the agglomeration and fragmentation of Al particles, and at small particle diameter, transition towards kinetic-limited mechanism. A widely accepted correlation for Al between various particle sizes, temperatures, pressures, and oxidizers was presented by Beckstead [60]. This correlation works very well for particle larger than 20μm and the effect of oxidizer is pronounced with

oxygen being twice as effective as water and about five times more effective than carbon dioxide.

Of the critical importance for the optimum performance of the combustion is the Al particle size. Obviously, the large Al particles require longer heating time and higher exothermic energy to reach the ambient temperature. Hence, smaller sizes of Al particles are preferred. The collection of the experimental measurements of the Al particles burning time versus the corresponding particles diameters is presented and the relation is plotted in [54] as shown in Figure 2.5.

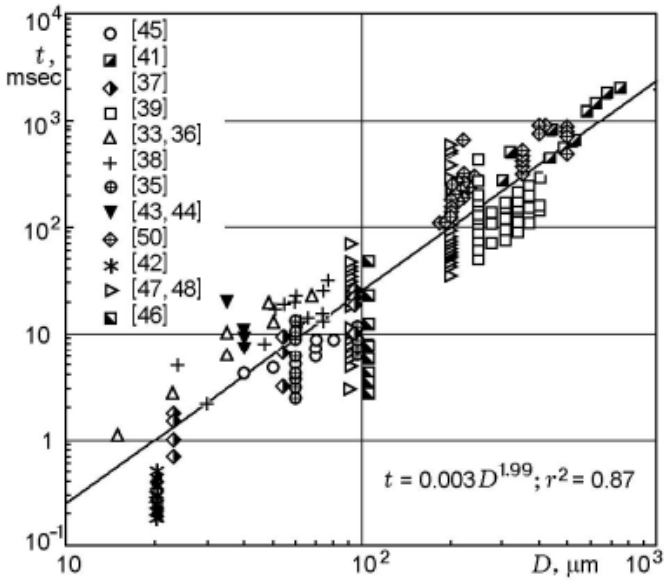

Figure 2.5 Al particles burning time versus particle diameters measured under various test techniques and conditions [54].

Generally, smaller Al particles sizes do demonstrate the shorter burning time under different test conditions. There are other benefits by using small particles of Al. For example, the contact area between aluminum and oxygen can be maximized. Therefore, the amount of energy being released due to the reaction can be maximized as well.

As the particle sizes become smaller and at lower pressure, the diffusion-limited assumption is no longer suitable. This is due to the enhancement of diffusion under both conditions. As the transition towards the kinetics-limited mechanism, significant difference in the burning rate with respect to the pressure, particle sizes, and oxidizer content are observed [66]. In one research [67], the burning time is proportional to D (n=1) and to 1/P, where D is the particle diameter and P is the pressure. Generally, the decreasing of n exponent in the D^n law and the increasing dependence of the temperature and pressure can be expected under the region of the kinetics-limited mechanism.

In recent years, nano-size Al particles generated great interests due to their large surface area and fast ignition time. Pure Al can be pyrophoric and thus each Al particle is coated with 4-8 nm thick of aluminum oxide passivation layer during the production process. As the particle size decreases, the Al_2O_3 shell becomes a considerable portion and reduces the active Al content. The role of the Al_2O_3 shell in the combustion may play a significant role in nano-scale Al particles and influence their performance. Also, the reaction mechanism of Al nanopowders is still unclear. In some researches, nano-sized aluminum particles do not show significant improvement in blast performance compared to micro-sized aluminum particles when mixed with other explosive powders [68, 69]. Some other researches demonstrated significant lowere ignition time and temperature with different reaction behavior compared to micro-scale Al particles [70, 71]. This indicates the ignition sensitivity may increase with nano-scale Al particles, which raises the safety concerns during shipping and handling of the composites. Our goal is to create energetic materials which are inert

under normal conditions and strong enough to survive the launch. Thus few micron-sized Al particles were used to process composites samples. On the later stages of deformation following impact Al matrix can be pulverized into fragments sizes less than 20 μm diameter.

2.3 Al-Ni Intermetallic Reactions

The Al-Ni system was selected due to the high exothermicity of the intermetallic reactions, e.g., 150.6 $kJ \cdot mol^{-1}$ for Al_3Ni, 293.2 $kJ \cdot mol^{-1}$ for Al_3Ni_2, and 129.2 $kJ \cdot mol^{-1}$ for AlNi [72]. As mentioned previously in Section 2.1.3, $AlNi_3$ and AlNi have generated great interests in high temperature applications. Many papers have been published employing Combustion Synthesis (CS) or Reaction Synthesis (RS) to fabricate intermetallics [73-78]. CS or RS can be subdivided into two reaction modes: self-propagating high-temperature synthesis (SHS) and thermal explosion. SHS can only be achieved if the exothermic heat of the reaction products formation is relatively large, like in the Al-Ni system, and at the same time a thermal conductivity is relatively low. On the other hand, in thermal explosion, the reactants need to be heated simultaneously in the bulk until they are converted to products.

In addition to the interests in bulk aluminide materials, reactive Al/Ni laminates also have wide variety of application when a controlled local heat source is required such as in soldering, ignition and propulsion [35, 79, 80]. Reactive Al/Ni laminates are generally fabricated by physical vapor deposition (PVD) [23, 27, 30, 33] or cold rolling [32, 36, 81]. Both methods can produce good quality laminates but they can be expensive, difficult and time consuming. Weihs and Reiss proposed a new

method to fabricate the reactive multilayer foils by swaging [82]. The advantages of this swaging method are its simplicity, low cost and time efficiency compared to PVD and cold rolling method.

The reactions in the Al-Ni system have been studied extensively [83, 84] and they can be initiated by local heating [23, 27, 30, 32, 33, 36, 81] or shock-and shear-induced [20, 21, 24, 25, 40, 85, 86]. Depending on the fabrication method of the laminates, the overall stoichiometry and how the reaction being initiated, the first phases to form in the Ni/Al reaction has been reported to be Al_3Ni [23, 27, 30, 32, 36, 81], AlNi [29, 40, 86] or Al_9Ni_2 [27, 33, 87]. A recent publication by Sauvage et al. [37] discovered that the severe plastic deformation by repeated folding and cold rolling can promote intermixing of Al and Ni. This induced the formation of metastable or non-equilibrium solid solution with various compositions before the Al_3Ni phase formed upon annealing.

In the context of this dissertation, Al-Ni laminates with concentric (by Cold Isostatic Pressing (CIPing)) and corrugated (by swaging) mesostructures will be prepared and tested by the Thick-Walled Cylinder (TWC) method. This allows us to examine how the laminates accommodate the high-strain, high-strain-rate, plastic deformation and if any reaction between Al and Ni can be induced by the high strain, high strain rate dynamic loading.

References:

1. R. G. Ames, *Energy Release Characteristics of Impact-Initiated Energetic Materials.* Materials Research Society Symposium Proceedings, 2006. **896**: p. 10.

2. J. J. C. Foster, J. G. Glenn, and M. Gunger, *Meso-scale origins of the low-pressure equation of state and high rate mechanical properties of plastic bonded explosives.* AIP Conference Proceedings, 2000. **505**(1): p. 703-706.

3. S. G. Bardenhagen and J. U. Brackbill, *Dynamic stress bridging in granular material.* Journal of Applied Physics, 1998. **83**(11): p. 5732-5740.

4. K. M. Roessig, J. C. Foster, and S. G. Bardenhagen, *Dynamic stress chain formation in a two-dimensional particle bed.* Experimental Mechanics, 2002. **42**(3): p. 329-337.

5. V. F. Nesterenko, M. A. Meyers, H. C. Chen, and J. C. Lasalvia, *Controlled High-Rate Localized Sheer in Porous Reactive Media.* Applied Physics Letters, 1994. **65**(24): p. 3069-3071.

6. V. F. Nesterenko, M. A. Meyers, H. C. Chen, and J. C. Lasalvia, *The Structure of Controlled Shear Bands in Dynamically Deformed Reactive Mixtures.* Metallurgical and Materials Transactions A-Physical Metallurgy and Materials Science, 1995. **26**(10): p. 2511-2519.

7. H. C. Chen, V. F. Nesterenko, and M. A. Meyers, *Shear localization and chemical reaction in Ti-Si and Nb-Si powder mixtures: Thermochemical analysis.* Journal of Applied Physics, 1998. **84**(6): p. 3098-3106.

8. K. Cho, S. Lee, Y. W. Chang, and J. Duffy, *Dynamic Fracture-Behavior of Sic Whisker-Reinforced Aluminum-Alloys.* Metallurgical Transactions a-Physical Metallurgy and Materials Science, 1991. **22**(2): p. 367-375.

9. M. Guden and I. W. Hall, *High strain rate properties of an SiC_W/2124-T6 aluminum composite at elevated temperatures.* Scripta Materialia, 1998. **39**(3): p. 261-267.

10. R. Vaziri, D. Delfosse, G. Pageau, and A. Poursartip, *High-Speed Impact Response of Particulate Metal Matrix Composite-Materials - an Experimental and Theoretical Investigation.* International Journal of Impact Engineering, 1993. **13**(2): p. 329-352.

11. I. W. Hall and M. Guden, *High strain rate behavior of a SiC particulate reinforced Al_2O_3 ceramic matrix composite.* Scripta Materialia, 1998. **38**(4): p. 667-674.

12. C. C. Perng, J. R. Hwang, and J. L. Doong, *High-Strain Rate Tensile Properties of an (Al_2O_3 Particles)-(Al Alloy 6061-T6) Metal-Matrix Composite.*

Materials Science and Engineering a-Structural Materials Properties Microstructure and Processing, 1993. **171**(1-2): p. 213-221.

13. S. Yadav, D. R. Chichili, and K. T. Ramesh, *The Mechanical Response of a 6061-T6 Al/Al_2O_3 Metal-Matrix Composite at High-Rates of Deformation.* Acta Metallurgica Et Materialia, 1995. **43**(12): p. 4453-4464.

14. D. R. Chichili and K. T. Ramesh, *Dynamic Failure Mechanisms in a 6061-T6 Al/Al_2O_3 Metal-Matrix Composite.* International Journal of Solids and Structures, 1995. **32**(17-18): p. 2609-&.

15. M. Guden and I. W. Hall, *High strain-rate compression testing of a short-fiber reinforced aluminum composite.* Materials Science and Engineering a-Structural Materials Properties Microstructure and Processing, 1997. **232**(1-2): p. 1-10.

16. M. Guden and I. W. Hall, *Quasi-static and dynamic compression behaviour of an FP $^{(TM)}$ alumina-reinforced aluminium metal matrix composite.* Journal of Materials Science, 1998. **33**(13): p. 3285-3291.

17. W. S. Lee and W. C. Sue, *Dynamic impact and fracture behaviour of carbon fiber reinforced 7075 aluminum metal matrix composite.* Journal of Composite Materials, 2000. **34**(21): p. 1821-1841.

18. J. Cai, Y. J. Chen, V. F. Nesterenko, and M. A. Meyers, *Effect of strain rate on the compressive mechanical of aluminum alloy matrix composite filled with discontinuous carbon fibers properties.* Materials Science and Engineering a-Structural Materials Properties Microstructure and Processing, 2008. **485**(1-2): p. 681-689.

19. Y. X. Zhou, Y. Wang, S. Jeelani, and Y. M. Xia, *Experimental study on tensile behavior of carbon fiber and carbon fiber reinforced aluminum at different strain rate.* Applied Composite Materials, 2007. **14**(1): p. 17-31.

20. Y. Horie, R. A. Graham, and I. K. Simonsen, *Synthesis of Nickel Aluminides under High-Pressure Shock Loading.* Materials Letters, 1985. **3**(9-10): p. 354-359.

21. I. K. Simonsen, Y. Horie, R. A. Graham, and M. Carr, *Formation of amorphous Nickel Aluminides under shock-wave loading.* Materials Letters, 1987. **5**(3): p. 75-78.

22. O. Arkens, L. Delaey, J. De Tavernier, B. Huybrechts, L. Buekenhout, and J. Libouton, *Dynamic compaction and hot-isostatic-pressing of nickelaluminides.* MRS Proceedings, 1988. **133**.

23. E. Ma, C. V. Thompson, and L. A. Clevenger, *Nucleation and Growth during Reactions in Multilayer Al/Ni Films - the Early Stage of Al3 Ni Formation.* Journal of Applied Physics, 1991. **69**(4): p. 2211-2218.

24. I. Song and N. N. Thadhani, *Shock-Induced Chemical-Reactions and Synthesis of Nickel Aluminides.* Metallurgical Transactions a-Physical Metallurgy and Materials Science, 1992. **23**(1): p. 41-48.

25. N. N. Thadhani, *Shock-Induced Chemical-Reactions and Synthesis of Materials.* Progress in Materials Science, 1993. **37**(2): p. 117-226.

26. F. Cardellini, G. Mazzone, A. Montone, and M. V. Antisari, *Solid-State Reactions between Ni and Al Powders Induced by Plastic-Deformation.* Acta Metallurgica Et Materialia, 1994. **42**(7): p. 2445-2451.

27. A. S. Edelstein, R. K. Everett, G. Y. Richardson, S. B. Qadri, E. I. Altman, J. C. Foley, and J. H. Perepezko, *Intermetallic Phase-Formation during Annealing of Al/Ni Multilayers.* Journal of Applied Physics, 1994. **76**(12): p. 7850-7859.

28. L. Battezzati, C. Antonione, and F. Fracchia, *Ni-Al Intermetallics Produced by Cold-Rolling Elemental Sheets.* Intermetallics, 1995. **3**(1): p. 67-71.

29. C. Michaelsen, G. Lucadamo, and K. Barmak, *The early stages of solid-state reactions in Ni/Al multilayer films.* Journal of Applied Physics, 1996. **80**(12): p. 6689-6698.

30. K. Barmak, C. Michaelsen, and G. Lucadamo, *Reactive phase formation in sputter-deposited Ni/Al multilayer thin films.* Journal of Materials Research, 1997. **12**(1): p. 133-146.

31. P. Zhu, J. C. M. Li, and C. T. Liu, *Combustion reaction in multilayered nickel and aluminum foils.* Materials Science and Engineering a-Structural Materials Properties Microstructure and Processing, 1997. **240**: p. 532-539.

32. L. Battezzati, P. Pappalepore, F. Durbiano, and I. Gallino, *Solid state reactions in Al Ni alternate foils induced by cold rolling and annealing.* Acta Materialia, 1999. **47**(6): p. 1901-1914.

33. K. J. Blobaum, D. Van Heerden, A. J. Gavens, and T. P. Weihs, *Al/Ni formation reactions: characterization of the metastable Al_9Ni_2 phase and analysis of its formation.* Acta Materialia, 2003. **51**(13): p. 3871-3884.

34. P. Zhu, J. C. M. Li, and C. T. Liu, *Adiabatic temperature of combustion synthesis of Al-Ni systems.* Materials Science and Engineering a-Structural

Materials Properties Microstructure and Processing, 2003. **357**(1-2): p. 248-257.

35. J. Wang, E. Besnoin, A. Duckham, S. J. Spey, M. E. Reiss, O. M. Knio, and T. P. Weihs, *Joining of stainless-steel specimens with nanostructured Al/Ni foils.* Journal of Applied Physics, 2004. **95**(1): p. 248-256.

36. X. Qiu and J. Wang, *Experimental evidence of two-stage formation of Al3Ni in reactive Ni/Al multilayer foils.* Scripta Materialia, 2007. **56**(12): p. 1055-1058.

37. X. Sauvage, G. P. Dinda, and G. Wilde, *Non-equilibrium intermixing and phase transformation in severely deformed Al/Ni multilayers.* Scripta Materialia, 2007. **56**(3): p. 181-184.

38. R. Knepper, M. R. Snyder, G. Fritz, K. Fisher, O. M. Knio, and T. P. Weihs, *Effect of varying bilayer spacing distribution on reaction heat and velocity in reactive Al/Ni multilayers.* Journal of Applied Physics, 2009. **105**(8).

39. E. Vitali, C. T. Wei, D. J. Benson, and M. A. Meyers, *Effects of geometry and intermetallic bonding on the mechanical response, spalling and fragmentation of Ni-Al laminates.* Acta Materialia, 2011. **59**(15): p. 5869-5880.

40. C. T. Wei, B. R. Maddox, A. K. Stover, T. P. Weihs, V. F. Nesterenko, and M. A. Meyers, *Reaction in Ni-Al laminates by laser-shock compression and spalling.* Acta Materialia, 2011. **59**(13): p. 5276-5287.

41. P. E. Specht, N. N. Thadhani, and T. P. Weihs, *Configurational effects on shock wave propagation in Ni-Al multilayer composites.* Journal of Applied Physics, 2012. **111**(7).

42. F. Zhang, R. Ripley, and W. Wilson, *Air blast characteristics of laminated al and NI-AL casings.* AIP Conference Proceedings, 2012. **1426**(1): p. 275-278.

43. G. M. Fritz, S. J. Spey, M. D. Grapes, and T. P. Weihs, *Thresholds for igniting exothermic reactions in Al/Ni multilayers using pulses of electrical, mechanical, and thermal energy.* Journal of Applied Physics, 2013. **113**(1).

44. A. K. Stover, N. M. Krywopusk, J. D. Gibbins, and T. P. Weihs, *Mechanical fabrication of reactive metal laminate powders.* Journal of Materials Science, 2014. **49**(17): p. 5821-5830.

45. X. P. Zhang, L. Ye, Y. W. Mai, G. F. Quan, and W. Wei, *Investigation on diffusion bonding characteristics of SiC particulate reinforced aluminium metal matrix composites (Al/SiCp-MMC).* Composites Part a-Applied Science and Manufacturing, 1999. **30**(12): p. 1415-1421.

46. I. A. Ibrahim, F. A. Mohamed, and E. J. Lavernia, *Particulate Reinforced Metal Matrix Composites - a Review.* Journal of Materials Science, 1991. **26**(5): p. 1137-1156.

47. L. Gerking, *Powder from Metallic and Ceramic Melts by Laminar Gas Streams at Supersonic Speeds.* Powder Met. Int., 1992. **25 (No. 2)**: p. 59-65.

48. G. Van Gurp, J. Daams, A. Van Oostrom, L. Augustus, and Y. Tamminga, *Aluminum - silicide reactions. I. Diffusion, compound formation, and microstructure.* Journal of Applied Physics, 1979. **50**(11): p. 6915-6922.

49. E. Colgan, *A review of thin-film aluminide formation.* Materials Science Reports, 1990. **5**(1): p. 1-44.

50. I. Krafcsik, J. Gyulai, C. Palmström, and J. Mayer, *Influence of Cu as an impurity in Al/Ti and Al/W thin - film reactions.* Applied Physics Letters, 1983. **43**(11): p. 1015-1017.

51. E. Colgan and J. Mayer, *Thin-film reactions of Al with Co, Cr, Mo, Ta, Ti, and W.* Journal of Materials Research, 1989. **4**(04): p. 815-820.

52. S. Wang and J. Mayer, *Marker studies in the reactions of W/Al couples.* Journal of Applied Physics, 1990. **67**(6): p. 2939-2943.

53. M. Tsukada and S. I. Ohfuji, *Interface Reaction of Al/W and Chemical-Properties of Al-W Bimetallic Bonding.* Journal of Vacuum Science & Technology A, 1995. **13**(5): p. 2525-2531.

54. M. W. Beckstead, *Correlating aluminum burning times.* Combustion Explosion and Shock Waves, 2005. **41**(5): p. 533-546.

55. *Metals Handbook*. 8 ed. Metallography, Structures and Phase Diagrams. Vol. 8. 1973, American Society for Metals: Metals Park, OH

56. C. T. Liu and V. K. Sikka, *Nickel Aluminides for Structural Use.* Journal of Metals, 1986. **38**(5): p. 19-21.

57. R. D. Noebe, R. R. Bowman, and M. V. Nathal, *Physical and Mechanical-Properties of the B2 Compound NiAl.* International Materials Reviews, 1993. **38**(4): p. 193-232.

58. I. Glassman, *Metal Combustion Processes.* American Rocket Society Preprint, 1959: p. 938-959.

59. P. F. Pokhil, V. M. Maltsev, V. S. Logachev, and V. A. Seleznev, *Combustion of Aluminum Particles in Flames of Condensed Systems.* Combustion Explosion and Shock Waves, 1971. **7**(1): p. 43-47.

60. M. W. Beckstead, Y. Liang, and K. V. Pudduppakkam, *Numerical simulation of single aluminum particle combustion (review).* Combustion Explosion and Shock Waves, 2005. **41**(6): p. 622-638.

61. P. F. Pokhil, V. S. Logachev, and V. M. Maltsev, *Mechanism of Metal Particle Combustion.* Combustion Explosion and Shock Waves, 1973. **6**(3): p. 356-358.

62. M. K. King, *Modeling of Single Particle Aluminum Combustion in CO_2 /N_2 Atmospheres.* 17th International Symposium on Combustion, The Combustion Institute, Pittsburgh, PA, 1977: p. 1317-1328.

63. C. K. Law, *A Simplified Theoretical Model for the Vapor-Phase Combustion of Metal Particles.* Combustion Science and Technology, 1973. **7**: p. 197-212.

64. J. L. Prentice, *Combustion of Laser-Ignited Aluminum Droplets in Wet and Dry Oxidizers.* AIAA 12th Aerospace Sciences Meeting, 1974(Paper No. 74-146).

65. K. K. Kuo, *Principles of Combustion, 2nd Edition*. 2005: John Wiley and Sons, New York.

66. P. Lynch, H. Krier, and N. Glumac, *A correlation for burn time of aluminum particles in the transition regime.* Proceedings of the Combustion Institute, 2009. **32**: p. 1887-1893.

67. R. A. Yetter, Dryer, F.L., *Microgravity Combustion: Fire in Free Fall (Chapter 6)*, ed. H.D. Ross. 2001, San Diego: Academic Press.

68. M. M. Mench, K. K. Kuo, C. L. Yeh, and Y. C. Lu, *Comparison of thermal behavior of regular and ultra-fine aluminum powders (Alex) made from plasma explosion process.* Combustion Science and Technology, 1998. **135**(1-6): p. 269-292.

69. P. Brousseau and C. J. Anderson, *Nanometric aluminum in explosives.* Propellants Explosives Pyrotechnics, 2002. **27**(5): p. 300-306.

70. E. M. Hunt, K. B. Plantier, and M. L. Pantoya, *Nano-scale reactants in the self-propagating high-temperature synthesis of nickel aluminide.* Acta Materialia, 2004. **52**(11): p. 3183-3191.

71. M. L. Pantoya and J. J. Granier, *Combustion behavior of highly energetic thermites: Nano versus micron composites.* Propellants Explosives Pyrotechnics, 2005. **30**(1): p. 53-62.

72. S. S. Dong, P. Hou, H. B. Yang, and G. T. Zou, *Synthesis of intermetallic NiAl by SHS reaction using coarse-grained nickel and ultrafine-grained aluminum produced by wire electrical explosion.* Intermetallics, 2002. **10**(3): p. 217-223.

73. J. Subrahmanyam and M. Vijayakumar, *Self-Propagating High-Temperature Synthesis.* Journal of Materials Science, 1992. **27**(23): p. 6249-6273.

74. H. C. Yi and J. J. Moore, *Self-Propagating High-Temperature (Combustion) Synthesis (SHS) of Powder-Compacted Materials.* Journal of Materials Science, 1990. **25**(2B): p. 1159-1168.

75. Z. Munir, *Reaction synthesis processes: mechanisms and characteristics.* Metallurgical Transactions A, 1992. **23**(1): p. 7-13.

76. J. J. Moore and H. Feng, *Combustion synthesis of advanced materials: Part I. Reaction parameters.* Progress in Materials Science, 1995. **39**(4): p. 243-273.

77. K. C. Patil, S. T. Aruna, and S. Ekambaram, *Combustion synthesis.* Current opinion in solid state and materials science, 1997. **2**(2): p. 158-165.

78. K. Morsi, *Review: reaction synthesis processing of Ni-Al intermetallic materials.* Materials Science and Engineering a-Structural Materials Properties Microstructure and Processing, 2001. **299**(1-2): p. 1-15.

79. J. Wang, E. Besnoin, O. M. Knio, and T. P. Weihs, *Effects of physical properties of components on reactive nanolayer joining.* Journal of Applied Physics, 2005. **97**(11).

80. J. Wang, E. Besnoin, A. Duckham, S. J. Spey, M. E. Reiss, O. M. Knio, M. Powers, M. Whitener, and T. P. Weihs, *Room-temperature soldering with nanostructured foils.* Applied Physics Letters, 2003. **83**(19): p. 3987-3989.

81. H. Sieber, J. S. Park, J. Weissmuller, and J. H. Perepezko, *Structural evolution and phase formation in cold-rolled aluminum-nickel multilayers.* Acta Materialia, 2001. **49**(7): p. 1139-1151.

82. T. P. Weihs and M. Reiss, *Method of making reactive multilayer foil and resulting product*. 2003: U.S. Patent 6,534,194.

83. D. B. Miracle, *Overview No.104 The physical and mechanical properties of NiAl.* Acta Metallurgica Et Materialia, 1993. **41**(3): p. 649-684.

84. I. Ansara, N. Dupin, H. L. Lukas, and B. Sundman, *Thermodynamic assessment of the Al-Ni system.* Journal of Alloys and Compounds, 1997. **247**: p. 20-30.

85. D. Eakins and N. N. Thadhani, *Discrete particle simulation of shock wave propagation in a binary Ni plus Al powder mixture.* Journal of Applied Physics, 2007. **101**(4).

86. C. T. Wei, V. F. Nesterenko, T. P. Weihs, B. A. Remington, H. S. Park, and M. A. Meyers, *Response of Ni/Al laminates to laser-driven compression.* Acta Materialia, 2012. **60**(9): p. 3929-3942.

87. M. H. D. Bassani, J. H. Perepezko, A. S. Edelstein, and R. K. Everett, *Initial phase evolution during interdiffusion reactions.* Scripta Materialia, 1997. **37**(2): p. 227-232.

CHAPTER 3 EXPERIMENTAL TECHNIQUES

Experimental techniques utilized in this research will be introduced in this chapter. They include the preparation and processing of samples, the testing methods and material characterization after tests. For high density reactive materials, Al-W granular/porous composite and Al-Ni laminates were selected for the research. To fabricate samples with various mesostructures, different morphology (e.g., particle sizes, wire diameter, or layer thickness) of as-received materials and different processing procedures to fabricate samples with desirable shape and accuracy will be applied.

A variety of testing methods are employed to investigate the mechanical properties of processed materials. Depending on the strain-rate, mechanical testing techniques can be classified into four categories [1]: creep and stress relaxation, quasi-static, dynamic, and impact as shown in Figure 3.1. The techniques utilized in this research include quasi-static and dynamic testing. To understand the influence of mesostructures, the characterization of recovered specimens from mechanical tests is very critical. Microscopy, including optical and scanning electron microscopy, X-ray diffractometry (XRD), particle size analysis by laser diffraction, and micro-hardness testing will be applied.

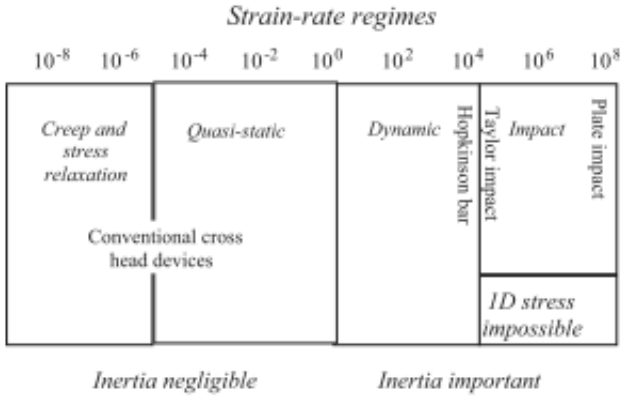

Figure 3.1 The schematic diagram of strain rate regimes (in reciprocal seconds) and the techniques that have been developed for obtaining them. [1]

3.1 Sample Preparation

3.1.1 Al-W Composites

High density aluminum-tungsten composites were prepared in our lab. All samples had identical mass ratios of Al and W components (23.8% Al and 76.2% W, by weight, corresponding to volume ratio of 69.0% Al and 31.0% W) with theoretical solid density of 7.8 g/cm^3. Randomly distributed mesostructure was chosen to create isotropic materials. They are fabricated from elemental powders of Al (-325 mesh, Alfa Aesar) and W with different particle sizes (coarse: -325 mesh and fine: <1 μm, both from Alfa Aesar). Tungsten short rods (4 mm long with 200 μm diameter, AM-System) were also used to replace W powder with the random orientation inside samples. Table 3.1 summarizes the characteristics of as-received materials used in Al-W composites.

Table 3.1 Characteristics of commercial powders and wire used in the research.

Powder	***Particle Size (µm)***	***Purity (wt %)***	***Manufacturer***
Aluminum	<44 µm (-325 mesh)	99.7	Alfa Aesar
Coarse Tungsten	<44 µm (-325 mesh)	99.5	Alfa Aesar
Fine Tungsten	<1 µm	99.5	Alfa Aesar
Rod	***Rod Diameter and Length***	***Purity (wt %)***	***Manufacturer***
Tungsten Rod	D=200 µm; L=4 mm	99.5	A-M System

With different particle size (fine vs. coarse) and morphology (powder vs. rod) of W, three types of samples with Al matrix were processed: (1) Al-Coarse W; (2) Al-Fine W; and (3) Al-W wires (randomly distributed). The mixtures of powders were blended in a SPEX 800 ball mill machine and then densified in the ABB Cold Isostatic Press (CIP). In order to understand the influence of the bonding between aluminum and aluminum, the Hot Isostatic Pressing (HIPing) was also carried out after CIPing process. Thus, the difference between non-bonded (CIPed only) and bonded (CIPed+HIPed) Al matrix can be investigated. There are six types of samples investigated in this research, taking into account the processing variables (see Figure 3.2).

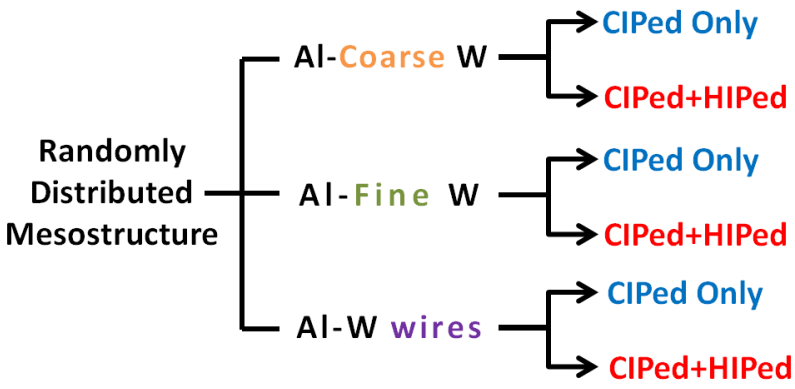

Figure 3.2 Types of investigated samples with different mesostructure

3.1.2 Al-Ni Laminates

Aluminum and nickel laminates were assembled from alternating thin foils of pure Al and Ni with a 1:1 atomic ratio of Ni/Al (theoretical solid density 5.2 g/cm^3). Two types of mesostructures were investigated: concentric and corrugated. The concentric mesostructure was created one layer at a time starting with the outermost layer. Each layer was prepared by first cutting a length of foil equal to the approximate circumference of its corresponding position in the final assembly. The foil was then cleaned with acetone, loosely rolled and inserted into the cylinder. A thin copper tube (wall thickness 0.5 mm) with an inner radius equal to the desired composite outer radius was used to encase the laminate. After each layer was inserted, a balloon was placed into the center cavity and inflated, causing the inner foil layer to unroll such that it was snug against the neighboring layer. The procedure was repeated until desirable thickness of sample was reached. The composite was then encapsulated in a rubber jacket and processed using cold isostatic pressing (CIPing) by applying pressure 345 MPa on the interior surface of the laminate to increase stacking density

and prevent the sample from buckling during preparation. After CIPing, the Al and Ni foils were densely packed, but the layers were not bonded. Porosity of samples after CIPing was about 6%.

Samples with corrugated mesostructure were fabricated by swaging of stacks of laminates instead of CIPing. The processing of the corrugated Al-Ni laminates was done in Johns Hopkins University and more details can be found in [2]. Alternating layers of Al (30 micron nominal thickness) and Ni (20 micron nominal thickness) were stacked, rolled into a cylinder and then placed into a tubular steel jacket. This jacketed assembly was then swaged using mating tapered dies resulting in cylindrical shaped rods with a corrugated mesostructure. The two rods that underwent 6 and 7 swaging cycles were used to prepare samples tested in this research, SW-6 and SW-7, respectively.

3.1.3 Ball Milling

The ball milling is an operation which fractures, deforms (cold works), or cold welds the impacted particles. Typical objectives of milling include particle size reduction, mixing or blending, particle shape change, and microstructure transformation. In this research, ball milling was employed to break down the agglomeration of Al and W powders. The powders were mixed, corresponding to the pre-determined ratio, and ball milled in an alumina vial set in the SPEX 800 for 10 minutes using alumina balls with a 1:5 mass ratio of balls to powder.

3.1.4 Cold Isostatic Pressing

To obtain high-accuracy samples, the cold isostatic pressing (CIPing) technique was adopted. CIPing is a materials processing technique in which high pressure is applied to metal powder in a sealed elastomeric container shaped for the application. The powder is converted from a loose aggregate into a partially dense compact that has sufficient green strength to permit careful handling and transfer to the following process operation. Figure 3.3 (a) and (b) demonstrate the examples of encapsulation for Al-W porous/granular composites and Al-Ni laminates, respectively. The steel mandrel was used to ensure the samples have excellent cylindrical shape after CIPing which was prerequisite to use them in subsequent mechanical testing. Different sizes and shapes (solid or hollow cylinders) of samples can be tailor-made by using the corresponding mandrel. For solid-cylinder samples, the mixture of the powder was sandwiched between two solid steel plugs inside the steel mandrel as shown in Figure 3.3 (a). To make a hollow cylinder, a slightly tapered steel rod (the slope from bottom to the larger top of the rod is 1^{o}) was inserted into a hollow steel plug located at the bottom of the mandrel. Then, the mixed powders were carefully added into the mandrel. Another hollow steel plug was placed at the top of the powders. After the powder was placed in the mandrel, the whole assembly was then placed into a rubber jacket with two rubber plugs at the both ends. Metal clamps were used to fasten and seal the gap between rubber plugs and the rubber jacket to avoid the pressure oil oozing into powders and contaminating them. After that, the whole assembly was placed in the high pressure chamber filled with oil in ABB Cold Isostatic Press as shown in Figure 3.3 (c).

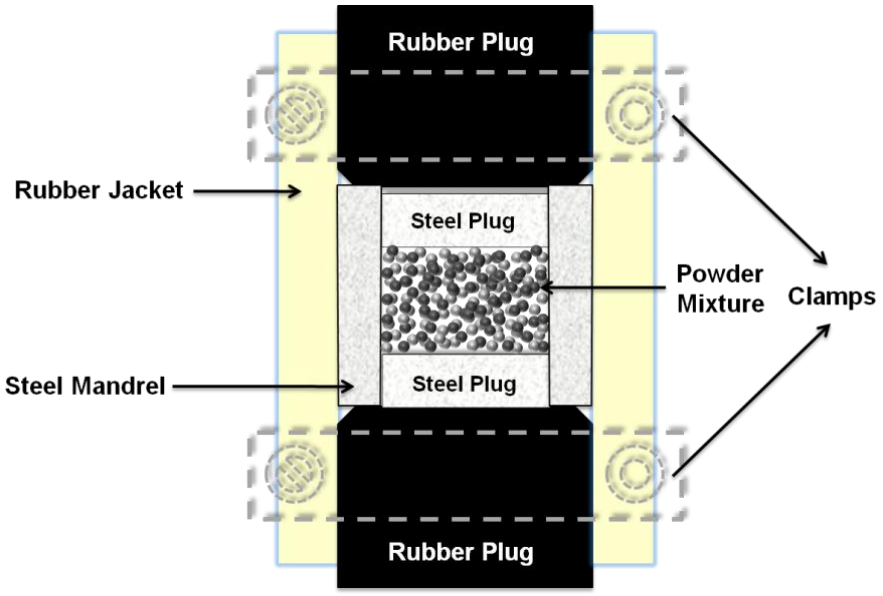
Rubber Plug
Rubber Jacket
Steel Plug
Powder Mixture
Clamps
Steel Mandrel
Steel Plug
Rubber Plug

(a)

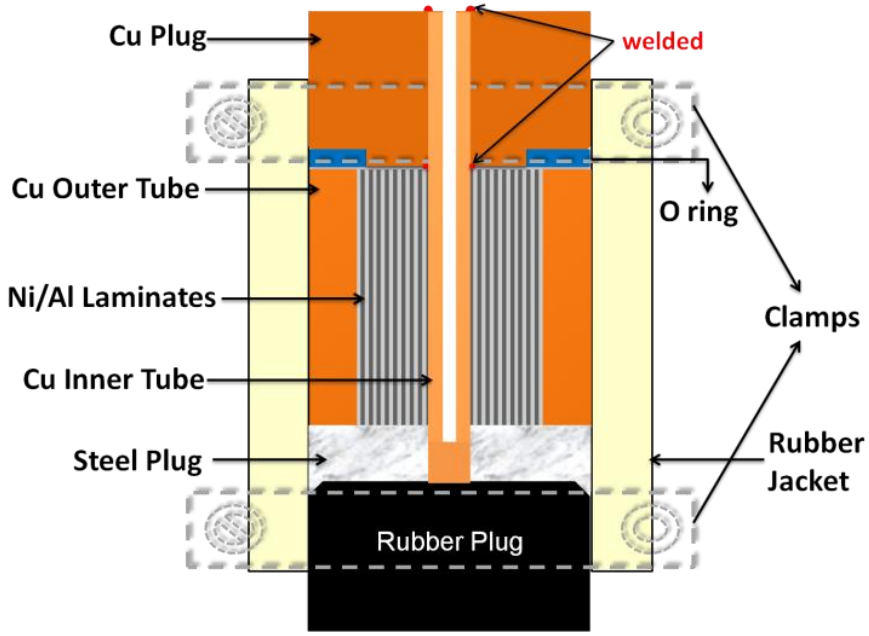
Cu Plug
welded
Cu Outer Tube
O ring
Ni/Al Laminates
Clamps
Cu Inner Tube
Steel Plug
Rubber Jacket
Rubber Plug

(b)

(c)

Figure 3.3 Illustrations of CIPing encapsulation for pressure assisted processing of heterogeneous materials;
(a) Al-W granular/porous composites and (b) Al-Ni concentric laminates. In this case central copper tube was inserted inside copper plug and welded at the bottom and at the top to prevent penetration of oil during CIPing. (c) ABB Cold Isostatic Press. Please note that in the case shown in (a) the densifying pressure to the sample was applied from the top and bottom. In the case (b) the densifying pressure was applied from inside the concentric Ni-Al assembly

This equipment is typically employed to pressurize powders into high accuracy solid samples (which did not require any additional manufacturing step) under room temperature and pressures up to 350 MPa. The lower CIPing pressures were used for samples if higher porosity was required. After the pressure ramped to 345 MPa, which typically took about 10 minutes, it would be held constant for 15 minutes before it gradually reduced to the atmospheric pressure for about 10 minutes. After the pressing cycle, the assembly was taken out, outside surface was cleaned from the oil and the assembly was disassembled. The sample was then gently pushed out. Figure 3.4

demonstrates some samples fabricate by Cold Isostatic Pressing from Al and W powder or Al powders and W wires.

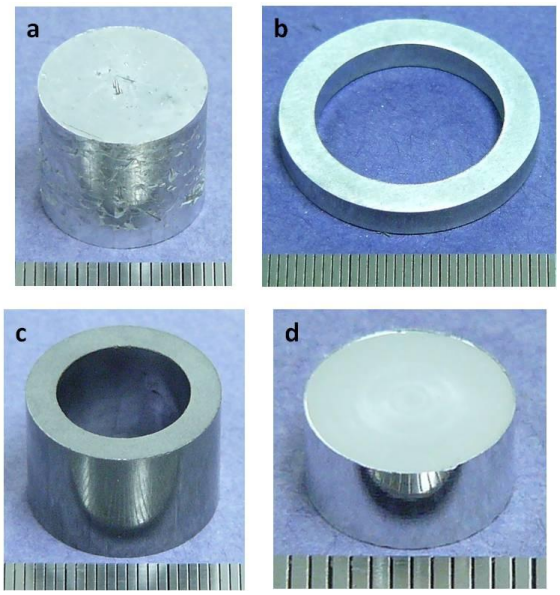

Figure 3.4 Some examples of CIPed samples and the spacing between two black lines in the bottom rulers is 1mm:
(a) cylindrical samples with randomly distributed W wires and matrix from coarse Al powder;
(b) ring shape samples from Al powder and coarse W powder;
(c) tube shape samples from Al powder and fine W powder;
(d) cylindrical samples from coarse Al powder and coarse W powder.

3.1.5 Hot Isostatic Pressing

Hot Isostatic Pressing (HIPing) is a process involving the use of high-pressure gas isostatically applied to an object at an elevated temperature performed in a specially constructed pressure vessel. This process can compress and sinter the part simultaneously. It is used when it is necessary to remove the porosity and obtain high strength of the samples. It can be used to consolidate powder, heal a casting compact, or bond two dissimilar materials. The HIP process eliminates internal voids and microporosity through a combination of plastic deformation, creep and diffusion

bonding and can achieve 100% theoretical density. The samples after HIPing may deform very little macroscopically; however, microscopically there is localized plastic flow mostly concentrated at the particles contacts enhancing bonding. A more detailed description of the mechanisms of porosity removal during HIPing can be found in [3-5].

The bonding between Al particles in the matrix may play an important role under dynamic loading. Therefore, HIPing is employed to bond the Al particles after the mixture of powder is compacted first in CIPing into the cylindrical shape. Prior to HIPing, the encapsulation of the sample is required to act as a barrier between the high-pressure gas and the sample to provide the force required to create the plastic deformation of the sample. An example of the encapsulation is shown in Figure 3.5 (a). To create bonding between Al particles and prevent reaction between Al and W at the same time, there is a rather narrow for optimum processing time and temperature. Some experiments were carried out in the vacuum oven to investigate when and at what temperature the reaction between Al and W occurred. The ABB Hot Isostatic Press shown in Figure 3.5 (b) is used to HIP Al-W granular/porous samples. Process parameters, such as time, pressure and temperature, are automatically controlled by the computer following prescribed path.

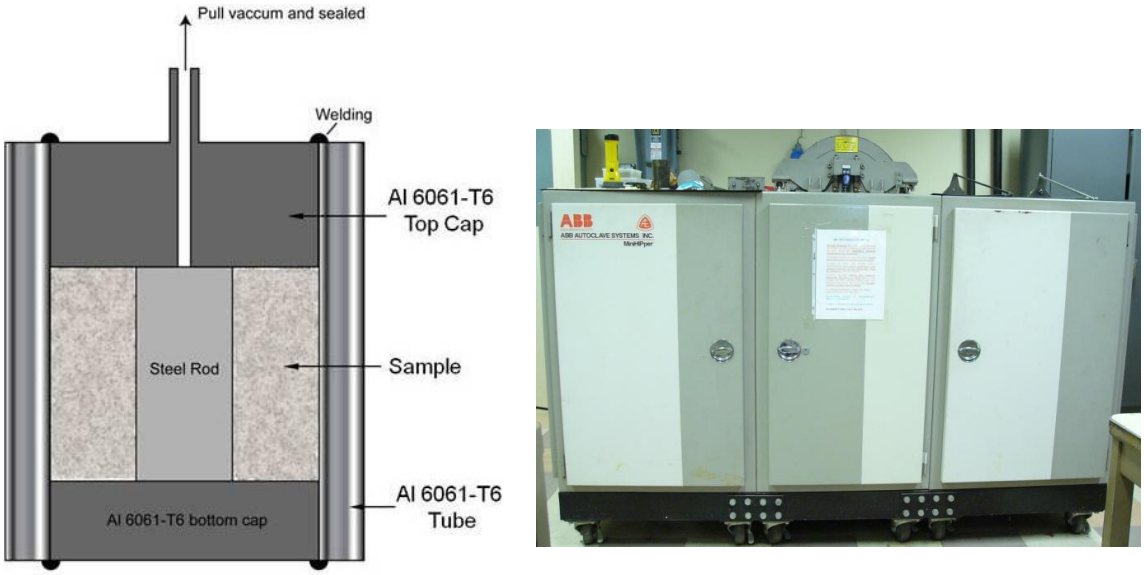

(a) (b)

Figure 3.5 (a) A schematic of the HIPing encapsulation to process hollow cylinder samples; (b) The cabinet style ABB Hot Isostatic Press.

3.1.6 Annealing

Most commercially available and affordable Al tubes are made of 6061-T6, which is also easy to machine. Annealing was utilized to reduce the hardness of tubes so they are easier to flow and deform at following CIPing and HIPing steps. Copper tubes used for Al-Ni laminates were also annealed for the same reason. Annealing is performed in the VAC vacuum oven in our lab (shown in Figure 3.6). Al is annealed at 415°C for 3 hours and Cu is annealed at 500^0C for an hour.

Figure 3.6 The VAC OC-1 vacuum oven for annealing process.

3.2 Mechanical Testing

3.2.1 Quasi-static Compression Testing

The SATECTM Universal Materials Testing Machine (Instron; Canton, MA) with a 5,000 lb loading capacity was employed to measure the strength of Al-W granular/porous materials under quasistatic loading (strain rate ~10^{-3} s^{-1}) until the sample was fractured. A clip-on extensometer was used to measure the displacement of the sample. The load-displacement data were recorded and converted to true stress-strain data from engineering stress-strain by the following equations:

$$\varepsilon_{tr} = ln(1+\varepsilon_e), \tag{3.1}$$

$$\sigma_{tr} = \sigma_e(1+\varepsilon_e), \tag{3.2}$$

where ε_e and σ_e are the engineering strain and stress, respectively.

3.2.2 Split Hopkinson Pressure Bar Compression Testing

Hopkinson Bar technique has been used to measure the dynamic properties of materials in the strain rate range of 10^3-10^4 s^{-1}. The split Hopkinson pressure bar (SHPB) was originally developed by Hopkinson [6] and later modified by Kolsky [7]. It has been intensively employed and modified to determine the dynamic response of a variety of engineering materials, such as metals [8-10], concrete [11], ceramics [12], composites [13-15], and polymers [9].

Figure 3.7 demonstrates the setup of the split Hopkinson Pressure Bar [8]. During the SHPB tests, a sample is deformed between two bars (incident bar and transmitted bar) [1]. Maraging steel was chosen as the material for all three bars (striker, incident and transmitted bars) because it can remain elastic while the samples may be driven to the large strain. Strain gauges are mounted on both incident and transmitted bars to measure the stress wave propagation. The pressurized gas in the launch chamber was released to drive the striker bar which hit the incident bar, the resulting elastic wave travels through the incident bar and reaches the sample. Due to the difference of shock impedances between the sample and the incident bar, a part of the incident wave is reflected back and can also be recorded by the strain gauge on the incident bar. The remainder of the stress pulse passes through the sample and enters the transmitted bar. A momentum trap made of lead was used to catch the transmitted bar at the end. An example of input (incident), transmitted and reflected pulses is shown in Figure 3.8. Hopkinson bar testing also provides information for a constitutive equation that represents the materials' dynamic behavior under specific circumstances at a given temperature and strain rates [16]. A high speed camera

(Phantom V12) was used to record images of samples during the tests and estimate nominal strains based on the change of the length of the sample.

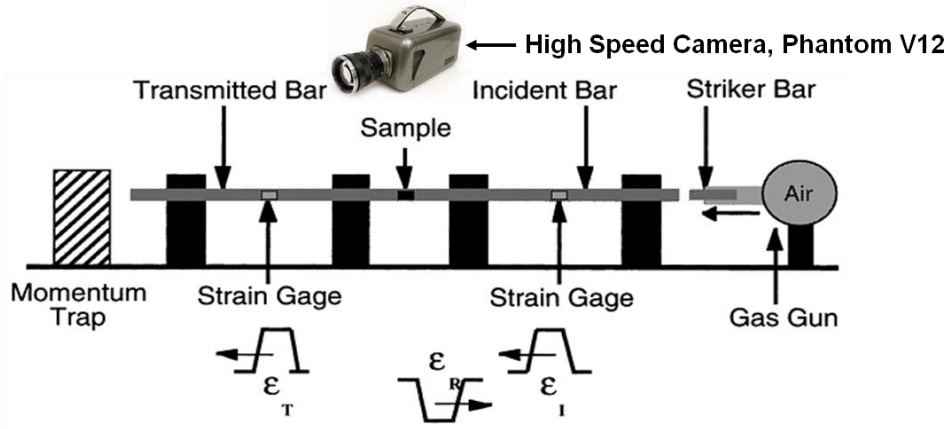

Figure 3.7 Illustration of striker bar, incident bar, transmitted bar, and sample in a split Hopkinson bar experiment with the high speed camera [8].

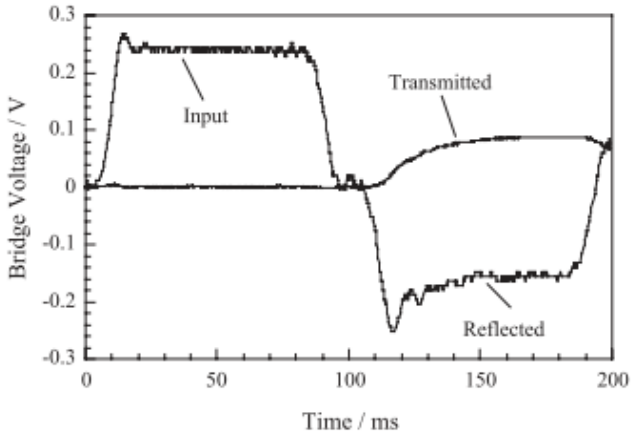

Figure 3.8 Typical input, reflected, and transmitted signals from a split Hopkinson bar experiment [1].

The elastic wave analysis of the SHPB assumes the bars are the 1-D linearly elastic objects so the elastic strains of the bars (measured by strain gauges) can relate to the force applied and the deformation of the sample. Detailed analysis can be found

in [8] and the dynamic stress of the sample σ(t), and its strain rate $\dot{\boldsymbol{\varepsilon}}$ can be expressed in the following equations :

$$\dot{\varepsilon} = \frac{2C\varepsilon_r}{l_s}, \tag{3.3}$$

$$\sigma(t) = \frac{AE\varepsilon_t}{A_s}, \tag{3.4}$$

where C is the longitudinal wave speed of the bar material (maraging steel); ε_r is the strain pulse reflected from the sample, which is measured from the strain gauge on the incident bar; l_s is the instantaneous length of the sample; A is the cross-sectional area of the bar and E is the Young's modulus of the incident and transmitted bars; ε_t is the strain pulse measured from the strain gauge on the transmitted bar; As is the cross-sectional area of the sample. Using equation 3.3 and 3.4, the stress-strain curve can be computed from two strain gauge signals.

3.2.3 Drop-weight Testing

The drop-weight apparatus has been widely used for a variety of test related to the dynamic response of materials. ASTM International has been published several standards governing the performance of such tests, e.g., ASTM D5420-98a and ASTM F736-95 for sheet materials. The drop-weight testing can also be used to investigate the impact sensitivity of reactive materials to evaluate their safety qualification [17, 18]. To analyze the output of a drop-weight test, the weight is assumed to behave as a rigid body and therefore Newton's laws of motion can be applied. A calibration

number k (unit N/V) is needed to convert voltage-time data into force-time data and can be expressed as follows:

$$k \cdot \int V dt = \int F dt \,, \tag{3.5}$$

According to Newton's Second Law ($F=ma$), the following equation is obtained by integrating it with respect to time:

$$m\Delta v = \int F dt \,, \tag{3.6}$$

where m is the mass of the drop-weight, $\int V dt$ is the integral of output voltage from the strain gauge and Δv is the change of the velocity of the weight.

The biggest challenge of drop-weight testing is the output signal often has oscillations comparable in magnitude to the signal generated by the sample deformation, especially when the low-strength materials are tested. This is due to the excitation of vibrations by impact in different parts of the device [1]. To reduce the oscillatory noise, a "soft" drop–weight testing is proposed [19]. A Nitrile O-ring (BS201N170) is placed on the top of the impact surface as shown in Figure 3.9 [20]. Examples of the oscillograms from the testing of the PTFE-Al-W granular/porous composites in conventional and "soft drop-weight testing are shown in Figure 3.10 (a) and (b), respectively. The oscillatory noise in "soft" drop weight testing is significantly reduced compared to the conventional drop-weight testing.

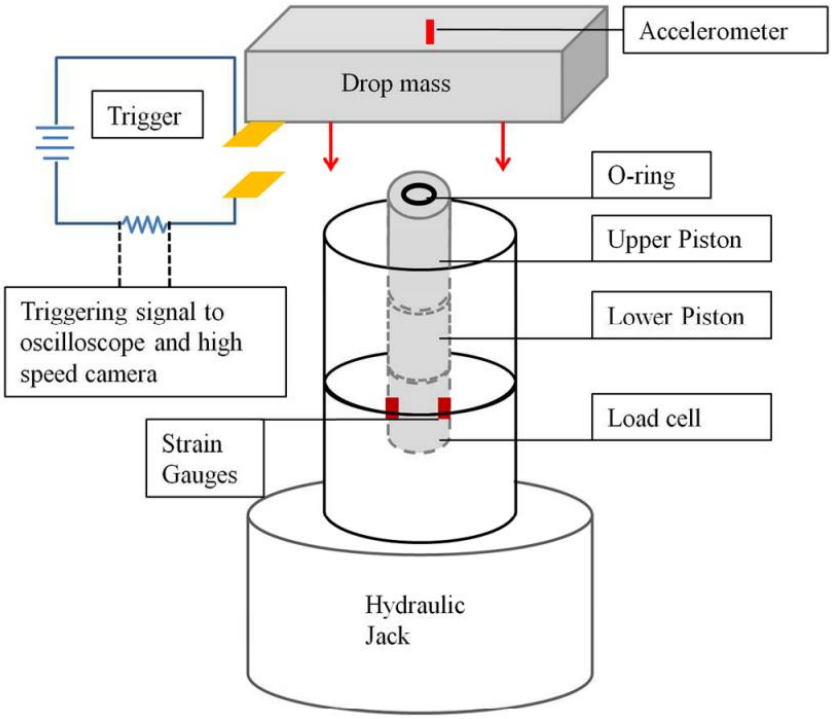

Figure 3.9 A Schematic diagram demonstrate the setup of the "soft" drop-weight testing [20].

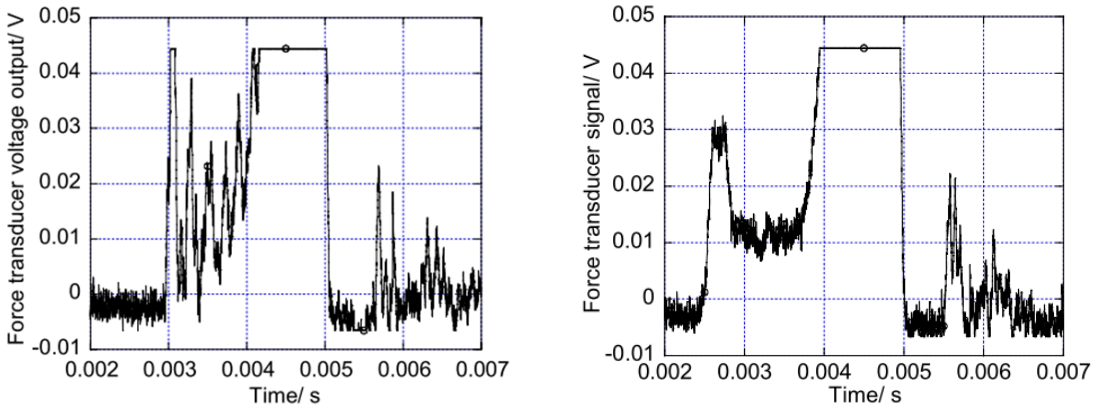

(a) (b)

Figure 3.10 (a) Output signal of a PTFE-Al-W granular/porous composite tested in the conventional drop-weight test, the oscillatory noise is comparable to the signal of interest; (b) Output signal of a similar material tested in the "soft" drop-weight testing, the oscillatory noise significantly reduced compared to (a) [19].

Instron DYNATUP 9250HV impact test instrument (shown in Figure 3.11) was used to test Al-W granular/porous composites. It was originally designed to

measure the energy absorption and related impact properties of materials. It is equipped with the velocimeter and variables such as the height, velocity and impact energy of the drop mass can be controlled. The instrument was modified in-house to allow compression tests and the schematic setup after modification is shown in Figure 3.9. A hydraulic jack (Central Hydraulic 30-ton) is added to the bottom to support the bottom anvil of apparatus necessary for compression tests. A brass block and a steel block with total mass of 14.4 kg were used. The brass block is a shock absorber to protect the equipment and sits on top of the steel block. When the drop mass falls, the steel block will directly impact a steel cylinder (the upper piston). The specimen is sandwiched between the upper and lower pistons. The load cell is a steel cylinder underneath the lower piston with two strain gauges attached on opposite sides to prevent signal originated by bending. A conditioner/amplifier (Ectron Model 778) is used and the signal is detected by an oscilloscope (Tektronix TDS2014). The data acquired from tests can be later converted into the time dependent force acting on the samples. A high speed camera (Phantom V12) was used to capture images of samples during the impact tests. The oscilloscope and the high speed camera were trigged simultaneously by the triggering device. Therefore, the high speed images and the output signals from the oscilloscope can be synchronized and each image can be related to specific point of the signal.

Figure 3.11 Instron DYNATUP 9250HV impact test instrument.

3.2.4 Explosively Driven Fragmentation Tests

The explosively driven fragmentation tests were conducted in the Cavendish Laboratory, Cambridge University, UK. The experimental setup is shown in Figure 3.12. The samples were placed around a Cu tube. The explosive charge (Primersheet 1000 discs) was placed inside the Cu tube and initiated by either a hollow end Nobel No. 6 detonator or a RP501 detonator made by Teledyne. Photon Doppler Velocimetry (PDV or Het-V) with nominal 140A laser output was used to capture the time-resolved expansion velocity. A high speed camera (Ultra 8) and two standard Bowens studio flashes were also used to obtain images with an interframe time of 2 microseconds. Paraffin wax (for homogeneous samples) or polyethylene glycol (for granular/porous

samples) was used for the soft capture of fragments. More detailed information regarding the experimental can be found in [21].

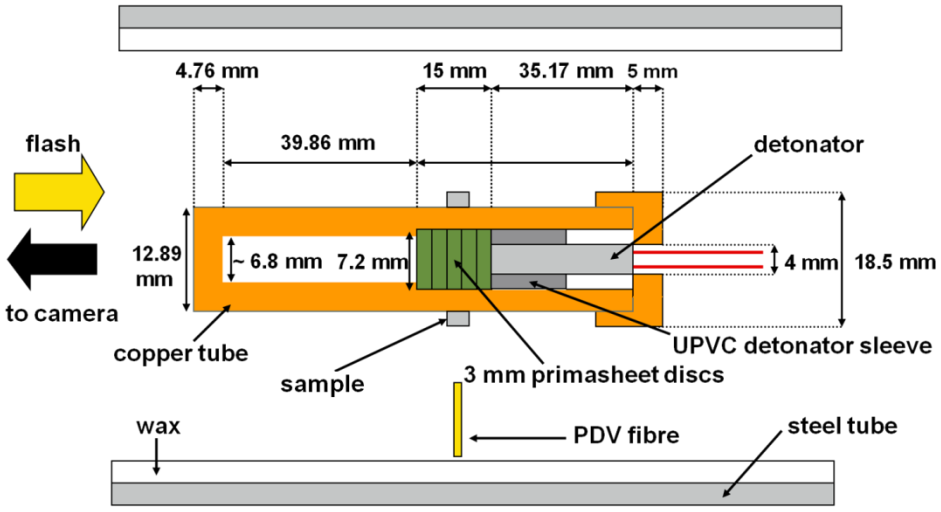

Figure 3.12 The schematic diagram shows the experimental setup of the explosively driven fragmentation tests performed in Cavendish Laboratory, Cambridge University, United Kingdom [21].

3.2.5 Thick-Walled Cylinder (TWC) Method

The Thick Walled Cylinder (TWC) method [22] was proposed to examine the development of material instabilities during the high strain rate, large strain deformations in plane strain conditions. It uses an explosive to collapse a cylindrical tube of the sample placed between two Cu tubes and the set-up is shown in Figure 3.13 [23]. The interior Cu tube (stopper tube) controls the total final maximum strain in the sample while the outer Cu tube (driver tube), which is accelerated by an explosive charge and axisymmetrically drives the radial collapse. Because the mass of the driver Cu tube is significantly larger than the mass of the TWC sample, the kinetics of the collapse are determined mainly by the thickness of the outer Cu tube,

allowing the testing of materials with different properties at similar strains and strain rates.

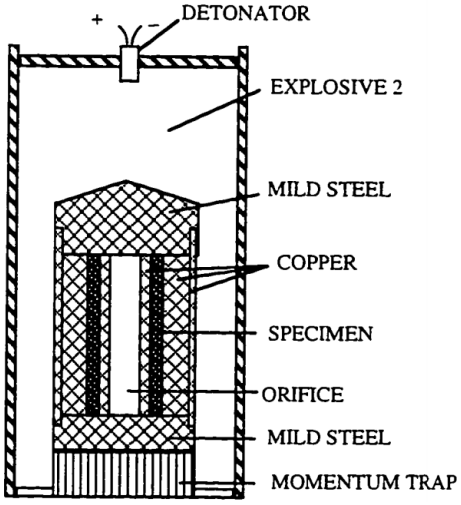

Figure 3.13 Experimental setup of thick-walled cylinder (TWC) method [23]. The specimen is sandwiched between a thick Cu outer tube and a thin Cu inner tube. The outer Cu tube (driver tube) is accelerated by an explosive charge and axisymmetrically drives the radial collapse of the specimen. The interior Cu tube (stopper tube) controls the total final maximum strain in the sample.

The TWC method is a strain-controlled test and the state of the strain within the collapsed cylinder is of pure shear (plane strain). The deformation of an element of radius r_0 is shown in Figure 3.14 [23]. As the tube is collapsed inward, the element moves toward the axis of the cylinder without the rotation and it is arrested at the final radii r_f when the Cu inner (stopper) tube is fully collapsed. The radial strain (ε_{rr}), tangential strain ($\varepsilon_{\varphi\varphi}$), and axial strain ($\varepsilon_{zz}$) can be expressed as followed:

$$\varepsilon_{rr} = -\varepsilon_{\phi\phi} = ln(\frac{r_0}{r_f}), \tag{3.7}$$

$$\varepsilon_{zz} = 0, \tag{3.8}$$

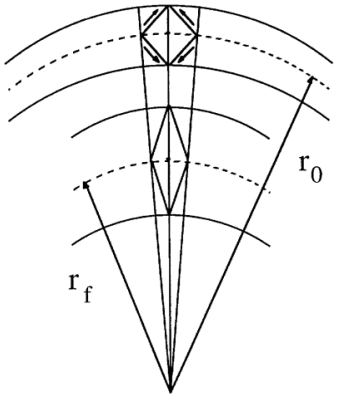

Figure 3.14 The pure shear deformation of an element under axisymmetrically-driven, radial collapse in TWC test, r_i and r_f are its initial and final radii, respectively [23].

Materials in the TWC method can be considered incompressible in the first approximation. Therefore, based on the conservation of mass, the initial and final positions of a general point, r_i and r_f, are related to the initial and final radii of cavity, R_0 and R_f, with following equation:

$$r_0^2 - R_0^2 = r_f^2 - R_f^2, \tag{3.9}$$

The effective strains at the points with radius r_f can be expressed as:

$$\varepsilon_{eff} = \frac{2}{\sqrt{3}}\varepsilon_{rr} = \frac{2}{\sqrt{3}} ln(\frac{r_0}{r_f}), \tag{3.10}$$

Equation 3.8, 3.9, and 3.10 are also applicable for the outside area, if the initial symmetry in this area is preserved, while shear bands can be generated in the inside area. This allows to study the shear band initiation and propagation under controlled conditions on the outside surface of the sample.

Various materials have been tested using TWC methods, e.g., metals and polymers [22-26], solid and granular ceramics [27-29], and reactive granular materials

[30-32]. They accommodate the high strain/strain-rate global plane strain deformation by developing multiple shear bands. These periodic and self-organized shear localization zones originating in the interior of the sample and propagating radially outward at an angle close to 45° to the radius. In some cases, these shear bands can number in the hundreds as in SS T-304L [26]. The mechanisms of plastic flow instability in the thick-walled cylindrical geometry responsible for triggering the spontaneous shear localization and subsequent pattern of shear bands are different for various classes of materials. For example, in solid homogeneous metals, the thermal softening triggers the shear instability at a very modest increase in the uniform temperature caused by plastic deformation (~30 K) [26]. In the case of granular materials, it is microfracture of grains due to the high stresses localized at the contact interfaces.

3.3 Characterization

3.3.1 High Speed Photography

High-speed photography has the great advantage of giving direct visual information about transient processes and allows to make measurements of sample deformation. Phantom V12 high speed camera was used during dynamic testing and shown in Figure 3.15. It is capable of taking 10^6 frames per second at lower resolution and 6242 frames per second at full 1280 x 800 high-definition. The camera is set to take a picture every 20 microseconds to have the optimal balance between resolution and frames-per-second. The duration of the impact at initial velocity of 10m/s is about

3 milliseconds and therefore 150 pictures will be taken, which can be used to compare the relative height of the specimen during the test and estimate strains.

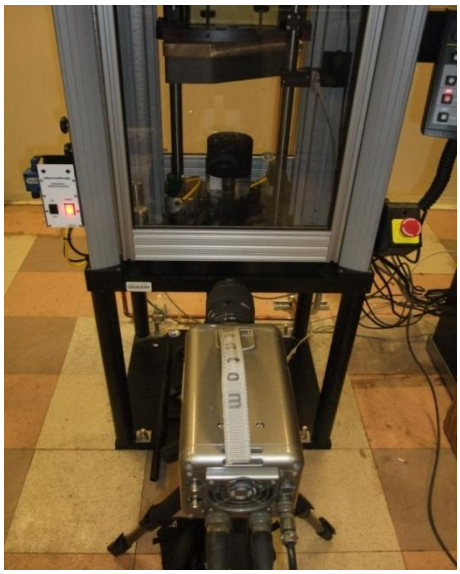

Figure 3.15 Phantom V12 high speed camera operated during the drop weight test.

3.3.2 Optical Microscopy (OM)

The morphology and microstructure of the specimens after processing and testing were examined with a Zeiss Axio Imager Optical Microscope in CalIT^2, UCSD. The specimen preparation included sectioning by diamond saw or electrical discharge maching (EDM), mounting in epoxy, grinding and polishing with a Struers RotoPol-11 Metallurgical Polisher.

3.3.3 Scanning Electron Microscopy (SEM)

The scanning electron microscope (SEM) has been widely used to investigate the materials surface. It provides two significant improvements over the optical microscope: (1) It increases the resolution limit to several nanometers and (2) it also

enhances the depth-of-field resolution dramatically. It consists of four major components: (1) the electron optical column, (2) the specimen chamber, (3) the vacuum system, and (4) the electronic control and imaging system as shown in Figure 3.16 [33].

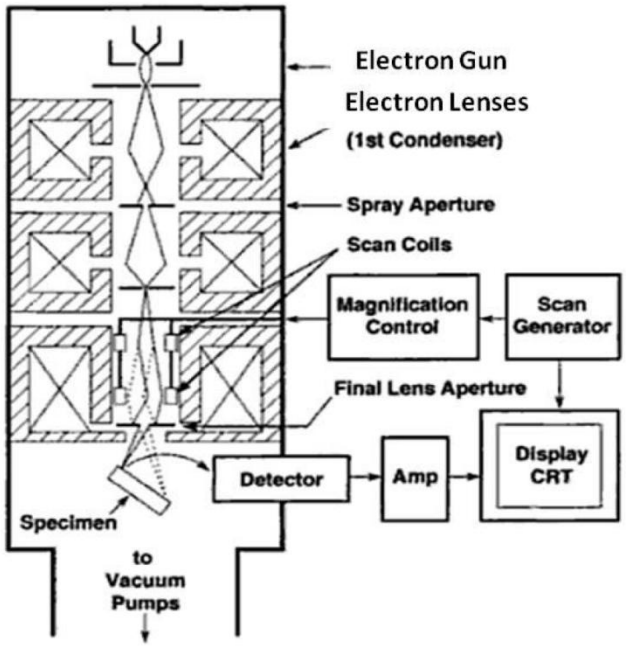

Figure 3.16 A diagram of the basic components of the scanning electron microscope [33].

The electron beam is generated by the electron gun at the top of the column and focused into a fine spot by the electron lens. The beam scans over the sample surface and the interaction between the beam electron and specimen surface creates various types of electrons, e.g., secondary electrons, backscattered electrons and auger electrons. The intensities of various electron signals are measures and the values are mapped as variation in brightness in images. The most commonly used signals in SEM are secondary electrons (SE) and backscattered electrons (BSE). Due to their low energies, SE can only escape the sample to be detected if they originate closely to the

sample surface. Therefore, the SE images have high spatial resolution and topographic contrast. On the other hand, the BSE images are primarily used for their strong atomic number (Z) contrast (brighter regions representing heavier elements).

A FEI XL30 Environmental Scanning Electron Microscope in CalIT^2, UCSD was used to capture the microstructural evolution of samples after high-strain, high-strain-rate deformation. This microscope is also equipped for Energy Dispersive X-ray spectroscopy (EDX) to detect the characteristic X-rays, which are produced by the interaction between the electron beam and the specimen. It can qualitatively and quantitatively identify the elemental composition of the area of interest in samples. The specimen preparation is similar to the optical microscope (including sectioning, mounting, grinding and polishing). If the sample is non-conductive or mounted in epoxy, about 1 μm thick of platinum (Pt) has to be deposited using Denton Discovery 18 Sputter System at CalIT^2, UCSD to prevent the accumulation of the electrostatic charge at the samples surface.

3.3.4 Microhardness Testing

The hardness measurement is a useful tool for evaluating materials properties after processing, heat treatment and testing. It can provide critical information of materials, such as strength, ductility and wear resistance, for quality control and research and development. Vickers hardness test was employed in this study with a LECO Model M400-H1 hardness tester due to its versatility and easy-to-use. It has a diamond pyramid indenter with the face angle equals to 136° as shown in Figure 3.17 [34] and can apply a giving load (P, in gf) to the specimen for 15 seconds. The Vickers

Hardness (HV) is calculated by the measuring the diagonal length (d, in micron) of an indent left by the indenter and using the following equation:

$$HV = \frac{1854.4P}{d^2}. \tag{3.11}$$

The corresponding units of HV are expressed in kilograms-force per square millimeter (kgf/mm^2) (rather than the equivalent grams-force per square micrometer ($gf/\mu m^2$)) and can be converted to megapascal (MPa).

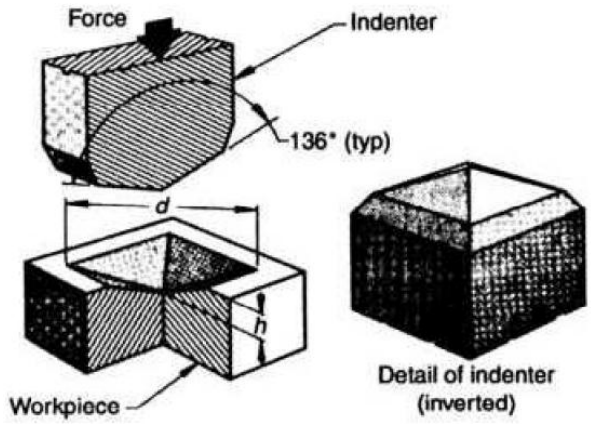

Figure 3.17 Schematic view of the indenter (pyramidal diamond with the square base) used in Vickers hardness tester and the resulting indentation on the specimen. [34]

3.3.5 X-ray Powder Diffraction

X-ray Powder Diffraction (XRPD) is used widely to identify crystalline phases in unknown samples qualitatively and quantitatively. It can also be used to characterize solid-state phase transformations/reactions and analyze the lattice parameter and crystal structure. The basic geometry of an X-ray diffractometer is shown in Figure 3.18 [35], where *C* is a powder specimen, *H* is the supporting table, *O* is the rotation axis, *S* is the X-ray source, *T* is the target of X-ray tube, *A* is the divergent slit, *B* and *F* are the receiving slits, *G* is the counter, *E* and *H* are

mechanically coupled supports to ensure focusing conditions, and *K* is the graduated scale. Rigaku MiniFlex II in Scripps Institution of Oceanography, UCSD was used to determine the reaction products of the fragments after explosively driven fragmentation tests.

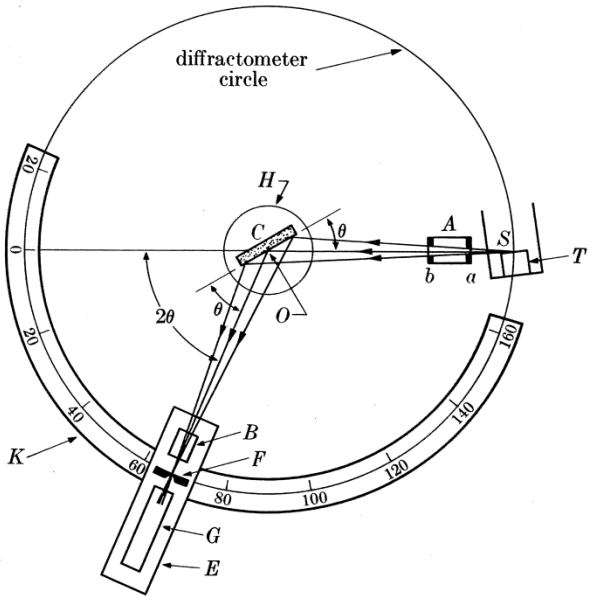

Figure 3.18 Schematic of X-ray diffractometer [35].

An incident X-ray beam is generated from the source and when it reaches the specimen (a crystalline structure), it scatters. Most scattering interferes with each other and is eliminated (destructive interference). When the scattering in a certain direction is in phase with the scattered rays from other atomic planes, they mutually reinforce each other (constructive interference) to form new enhanced wave fronts and diffraction occurs. The relation by which diffraction occurs is known as the Bragg's law and can be expressed by:

$$n\lambda = 2d\sin\theta, \tag{3.12}$$

where n is an integer, λ is the wavelength of the incident, d is the space between the atomic planes in the crystal, and θ is the angle between the incident beam and the particular scattering planes as shown in Figure 3.19. Each crystalline material will diffract X-rays in a unique pattern due to its characteristic atomic structure. The pattern is then compare to the data from the Joint Committee on Powder Diffraction International Center for Diffraction Data (JCPDS-ICDD), which has been collecting, editing, publishing, and distributing powder diffraction data for decades. Based on these data the phase in question can be identified.

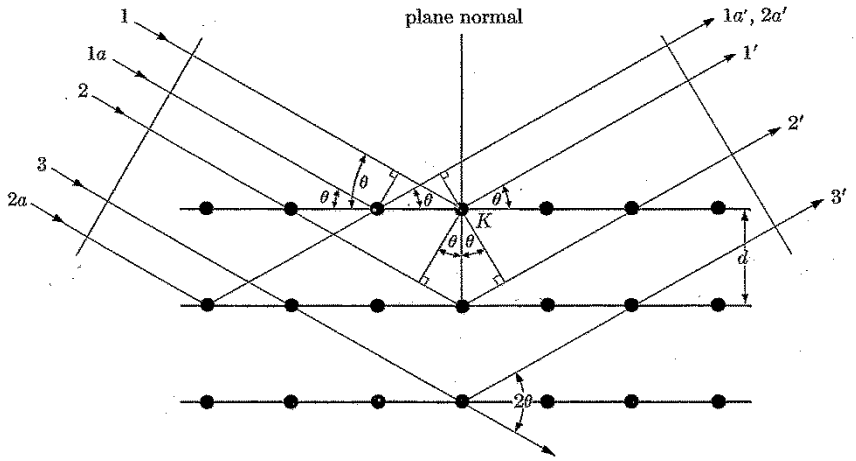

Figure 3.19 Diffraction of X-ray beams by a crystalline structure is described by the Bragg's law [35].

3.3.6 Particle Size Analysis-Laser Diffraction

Particle size is a critical parameter for wide variety of industries, such as chemical, pharmaceutical, mining, and agriculture. It is also one of the principal variables to characterize materials after processing and testing. Various techniques have been developed, e.g., sieve analysis, sedimentation techniques, air elutriation analysis, imaging analysis, and dynamic light scattering. Laser diffraction methods

have emerged as the technique of choice in many industrial sectors due to its flexibility, automated and fast measurement, non-destructiveness, and wide measurement range (0.1-3000 µm). It measures the particle size distribution by passing a dispersed particulate sample through a collimated laser. Large particles scatter the light at relatively narrow angles to the laser beam with a high scattering intensity, while smaller particles result in a low scattering intensity at wider angles as demonstrated in Figure 3.20 [36]. From the recorded angular variation of intensities of the light scattered and using an appropriate theory of the light behavior, the particle size distribution of the sample can be determined. The Mie theory of light scattering is applied mostly and details are covered by ISO 13320 (2009), the international standard for laser diffraction.

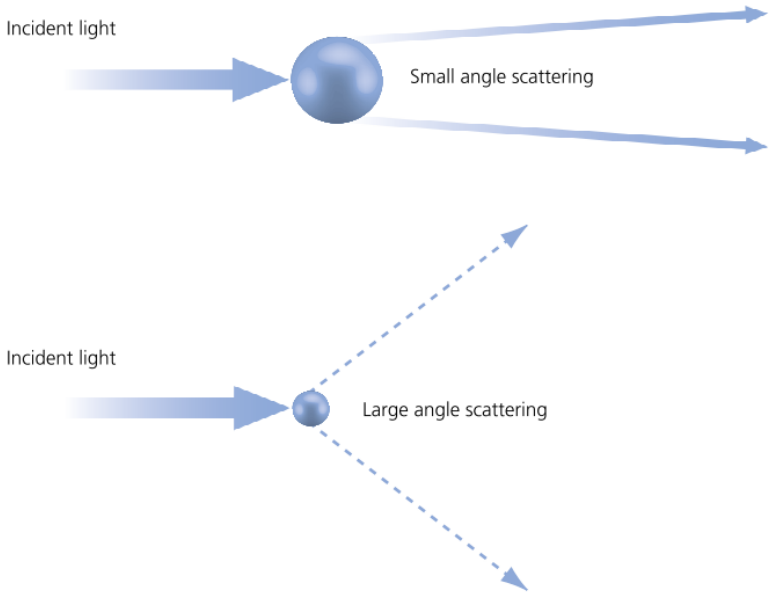

Figure 3.20 Scattering of a laser beam from large and small particles. [36]

Fragments sizes of energetic materials under high-strain, high-strain-rate testing is critical to their performance. The fragments of each sample from explosively

driven fragmentation tests were collected and sent to Particle Technology Labs to analyze the particle size distribution of the fragments. A Malvern Mastersizer MS2000 with a wet dispersion (Hydro S accessory) was used. The analyses were run at least three times for each sample to ensure the reproducibility of the results.

Reference:

1. J.E. Field, S.M. Walley, W.G. Proud, H.T. Goldrein, and C.R. Siviour, *Review of experimental techniques for high rate deformation and shock studies.* International Journal of Impact Engineering, 2004. **30**(7): p. 725-775.

2. E.P. Degarmo, J.T. Black, and R.A. Kohser, *Materials and processes in manufacturing*. 9th ed. 2003, Hoboken, NJ: John Wiley & Sons.

3. R.D. Kissinger, *The Densification of Nickel Base Superalloy Powders by Hot Isostatic Pressing.* Diss. Abstr. Int., 1989. **49**(9): p. 1-39.

4. W.B. Eisen, *Modeling of Hot Isostatic Pressing.* Rev. Partic. Mater., 1996. **4**.
5. E. Arzt, M.F. Ashby, and K.E. Easterling, *Practical Applications of Hot-Isostatic Pressing Diagrams - 4 Case Studies.* Metallurgical Transactions a-Physical Metallurgy and Materials Science, 1983. **14**(2): p. 211-221.

6. B. Hopkinson, *A Method of Measuring the Pressure Produced in the Detonation of High Explosives or by the Impact of Bullets.* Phil. Trans. Roy. Soc. London, 1914. **A**(213): p. 437-456.

7. H. Kolsky, *An Investigation of the Mechanical Properties of Materials at very High Rates of Loading.* Proceedings of the Physical Society Section B, 1949. **62**: p. 676-700.

8. G.T. Gray, *Classic Split-Hopkinson Pressure Bar Testing*. Mechnical Testing and Evaluation, ASM Handbook, ed. H. Kuhn and D. Medlin. Vol. 8. 2000, Materials Park: ASM International.

9. E.D.H. Davies and S.C. Hunter, *The Dynamic Compression Testing of Solids by the Method of the Split Hopkinson Pressure Bar.* Journal of the Mechanics and Physics of Solids, 1963. **11**(3): p. 155-179.

10. K.S. Vecchio and F.C. Jiang, *Improved pulse shaping to achieve constant strain rate and stress equilibrium in split-hopkinson pressure bar testing.*

Metallurgical and Materials Transactions a-Physical Metallurgy and Materials Science, 2007. **38A**(11): p. 2655-2665.

11. C.A. Ross, D.M. Jerome, J.W. Tedesco, and M.L. Hughes, *Moisture and strain rate effects on concrete strength.* Aci Materials Journal, 1996. **93**(3): p. 293-300.

12. W.N. Chen and G. Ravichandran, *Dynamic compressive failure of a glass ceramic under lateral confinement.* Journal of the Mechanics and Physics of Solids, 1997. **45**(8): p. 1303-1328.

13. M. Guden and I.W. Hall, *High strain-rate compression testing of a short-fiber reinforced aluminum composite.* Materials Science and Engineering a-Structural Materials Properties Microstructure and Processing, 1997. **232**(1-2): p. 1-10.

14. W.S. Lee and W.C. Sue, *Dynamic impact and fracture behaviour of carbon fiber reinforced 7075 aluminum metal matrix composite.* Journal of Composite Materials, 2000. **34**(21): p. 1821-1841.

15. L. Ninan, J. Tsai, and C.T. Sun, *Use of split Hopkinson pressure bar for testing off-axis composites.* International Journal of Impact Engineering, 2001. **25**(3): p. 291-313.

16. B. Wang and S. Yi, *Dynamic plastic behavior of 63 wt% Sn 37 wt% Pb eutectic solder under high strain rates.* Journal of Materials Science Letters, 2002. **21**(9): p. 697-698.

17. H. Mortlock and J. Wilby, *The Rotter apparatus for the determination of impact sensitiveness.* Explosivstoffe, 1966. **14**: p. 49-55.

18. E.M. Hunt and M.L. Pantoya, *Impact sensitivity of intermetallic nanocomposites: A study on compositional and bulk density.* Intermetallics, 2010. **18**(8): p. 1612-1616.

19. J. Addiss, J. Cai, S. Walley, W. Proud, and V. Nesterenko, *High strain and strain-rate behaviour of PTFE/Aluminium/Tungsten mixtures.* AIP Conference Proceedings, 2007. **955**(1): p. 773-776.

20. C.W. Lee and V.F. Nesterenko, *Dynamic deformation of strongly nonlinear toroidal rubber elements.* Journal of Applied Physics, 2013. **114**(8).

21. C.H. Braithwaite, A.L. Collins, B. Aydelotte, F. McKenzie, P.-H. Chiu, N. Thadhani, and V.F. Nesterenko, *Advances in the study of novel energetic materials.* Proc. 15th Seminar New Trends in Research of Energetic Materials, University of Pardubice, Czech Republic, 2012: p. 93-99.

22. V.F. Nesterenko, *Dynamics of Heterogeneous Materials*. First ed. Shock Wave and High Pressure Phenomena. 2001, New York: Springer. 536.

23. V.F. Nesterenko, M.A. Meyers, and T.W. Wright, *Self-organization in the initiation of adiabatic shear bands.* Acta Materialia, 1998. **46**(1): p. 327-340.

24. Y.J. Chen, M.A. Meyers, and V.F. Nesterenko, *Spontaneous and forced shear localization in high-strain-rate deformation of tantalum.* Materials Science and Engineering a-Structural Materials Properties Microstructure and Processing, 1999. **268**(1-2): p. 70-82.

25. M.A. Meyers, V.F. Nesterenko, J.C. LaSalvia, and Q. Xue, *Shear localization in dynamic deformation of materials: microstructural evolution and self-organization.* Materials Science and Engineering a-Structural Materials Properties Microstructure and Processing, 2001. **317**(1-2): p. 204-225.

26. Q. Xue, V.F. Nesterenko, and M.A. Meyers, *Evaluation of the collapsing thick-walled cylinder technique for shear-band spacing.* International Journal of Impact Engineering, 2003. **28**(3): p. 257-280.

27. C.J. Shih, V.F. Nesterenko, and M.A. Meyers, *High-strain-rate deformation and comminution of silicon carbide.* Journal of Applied Physics, 1998. **83**(9): p. 4660-4671.

28. C.J. Shih, M.A. Meyers, and V.F. Nesterenko, *High-strain-rate deformation of granular silicon carbide.* Acta Materialia, 1998. **46**(11): p. 4037-4065.

29. V.F. Nesterenko, M.A. Meyers, and H.C. Chen, *Shear localization in high-strain-rate deformation of granular alumina.* Acta Materialia, 1996. **44**(5): p. 2017-2026.

30. V.F. Nesterenko, M.A. Meyers, H.C. Chen, and J.C. Lasalvia, *Controlled High-Rate Localized Sheer in Porous Reactive Media.* Applied Physics Letters, 1994. **65**(24): p. 3069-3071.

31. V.F. Nesterenko, M.A. Meyers, H.C. Chen, and J.C. Lasalvia, *The Structure of Controlled Shear Bands in Dynamically Deformed Reactive Mixtures.* Metallurgical and Materials Transactions A-Physical Metallurgy and Materials Science, 1995. **26**(10): p. 2511-2519.

32. H.C. Chen, V.F. Nesterenko, and M.A. Meyers, *Shear localization and chemical reaction in Ti-Si and Nb-Si powder mixtures: Thermochemical analysis.* Journal of Applied Physics, 1998. **84**(6): p. 3098-3106.

33. D.E.N. Goldstein J., D.C. Joy, C.E. Lyman, P. Echlin, E. Lifshin, L.C. Sawyer, and J.R. Michael, *Scanning Electron Microscopy and X-ray Microanalysis*. 3rd ed. 2003, New York: Springer-Verlag.

34. *Mechanical Testing*. 1998, ASM International. p. 1308-1342.

35. B.D. Cullity and S.R. Stock, *Elements of X-ray Diffraction*. 2001: Pearson.

36. C. Levoguer and P. Kippax, *Laser Diffraction: A Firm Foundation for Particle Characterization.* American Laboratory, 2011. **43**(8): p. 13-16.

CHAPTER 4 RESULTS AND DISCUSSION

In this chapter, the results of the different tests introduced in the previous chapter are presented and discussed. It is divided into four sections based on materials investigated: Al-W composites: W particulate–reinforced (Section 4.1) and W fiber–reinforced (Section 4.2); Al-Ni concentric laminates (Section 4.3) and Al-Ni corrugated laminates (Section 4.4).

4.1 Al-W Particulate-reinforced Composites

4.1.1 Sample Preparation

Al-W particulate-reinforced granular/porous composites were Cold Isostatically Pressed (CIPed) from the elemental powders of Al (-325 mesh, Alfa Aesar), coarse W (-325 mesh, Alfa Aesar) and fine W (particle size less than 1 micron, Alfa Aesar) with identical mass ratios (23.8 wt% Al and 76.2 wt% W, by weight, corresponding to volume ratio 69% and 31%, respectively) corresponding to their solid density 7.8 g/cm^3. The processing pressures with the achieved densities of each sample after CIPing are shown in Table 4.1. Samples with fine W particles at the same densification pressure (345MPa) demonstrated a higher porosity (about 29%) than samples with coarse W particles (about 14%). The increased level of porosity indicates that fine W particles resist densification stronger in comparison with coarse W particles. This is consistent with the microstructure and the higher strength of composite with fine W particles observed in quasistatic and dynamic tests later. To

investigate the behavior of Al-coarse W composite samples with porosity similar to Al-fine W composites, the former material was CIPed at significantly lower pressure of 48 MPa. The Higher-Porosity (HP) Al-coarse W samples have porosity about 29%.

Table 4.1 Experimental results of sample properties after processing.

Sample Type	**CIPing Pressure (MPa)**	**HIPing Pressure (MPa)**	**Density (g/cm^3)**	**Porosity (%)**
Al-fine W *CIPed only*	345	N/A	5.53±0.2	29.1
Al-fine W *CIPed+HIPed*	345	200	6.05±0.3	22.9
Al-coarse W *CIPed only*	345	N/A	6.74±0.2	13.6
Al-coarse W *CIPed+HIPed*	345	200	7.19±0.3	7.8
HP Al-coarse W *CIPed only*	48	N/A	5.57±0.1	28.6

Hot Isostatic Pressing (HIPing) temperature was studied first to prevent bonding/reaction between aluminum and tungsten. From the Al-W binary phase diagram (Figure 2.3), the processing temperature should be lower than 660°C. Several Al-coarse W CIPed only samples were put into the vacuum oven at 550^0C for three hours. The SEM images and EDX analysis revealed that there is reaction between Al and W (and fracturing of reaction products due to the change of the volume of reactants) at this condition as shown in Figure 4.1. Both W-rich (light gray, X_1-X_4 in the figure) and Al-rich (dark gray, X_5-X_8 in the figure) reaction products were found. The temperature was then lower to 500^0C with the same duration (three hours). At these conditions no intermetallic reaction between Al and W was found.

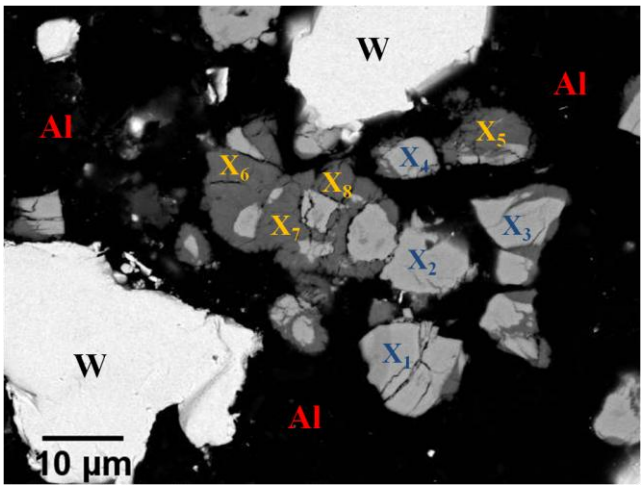

Figure 4.1 SEM (BSE) images of the Al-coarse W CIPed only sample after 3 hours in the vacuum oven at 550°C. Intermetallic reaction between Al-W was found and locations X_1-X_8 is where the EDX analysis was conduct showing W-rich (X_1-X_4) and Al-rich (X_5-X_8) reaction product with multiple cracks.

Based on these results we selected the HIPing temperature being equal to 500^0C, which was used for all HIP processing of Al-W systems in this dissertation: Al/W powders and Al tubes and W wires. Holding time, pressure, and pressure/temperatures paths were found experimentally, keeping the maximum available pressure and minimizing the time of high temperature exposure. For our application, HIPing cycle for Al-W granular/porous composite was optimized at 500^0C and 200 MPa with a hold time 25 minutes and the cooling under pressure as shown in Figure 4.2. After CIPing at 345 MPa, some samples (both Al-coarse W and Al-fine W granular/porous composites) underwent the subsequent HIPing to introduce bonding between Al particles with a goal to investigate its role in dynamic behavior and subsequent fracture of samples. During the HIPing about 6% of porosity was removed for both Al-coarse W and Al-fine W granular/porous composites. The density and porosity of samples after CIPing and HIPing can be found in Table 4.1.

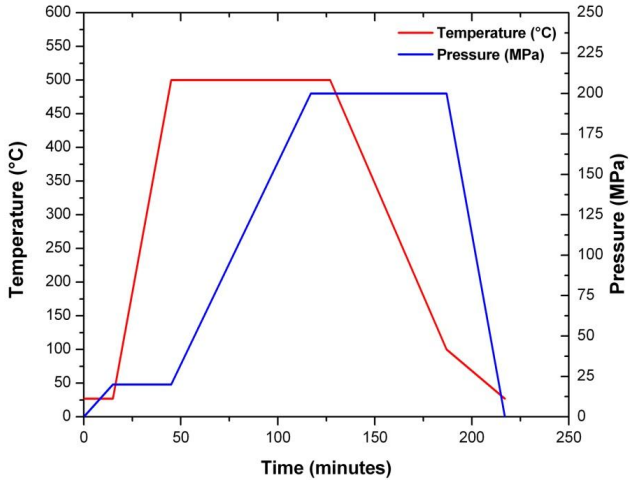

Figure 4.2 The HIP cycle for fabricating Al-W CIPed+HIPed samples.

The optical micrographs of Al-coarse W and Al-fine W after CIPing (and before HIPing) at 345 MPa are shown in Figure 4.3 (a) and (b), respectively. The white area is Al matrix and the gray area is W particles. Pores or the fallout of W particle during polishing are in black. The Al matrix in samples with coarse W particles is much compacted and denser than samples with fine W particles. This indicates that samples with fine W particles resisted densification as mentioned previously.

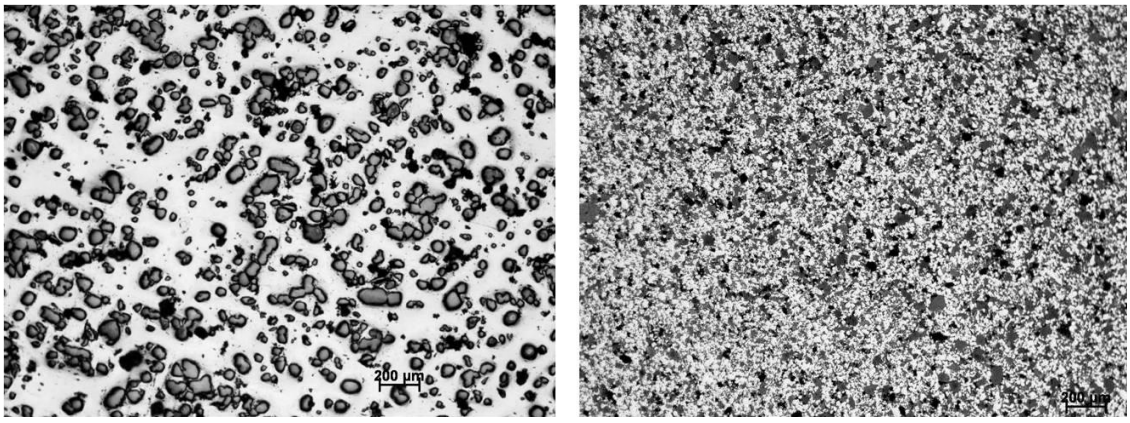

(a) (b)

Figure 4.3 The optical microstructure of (a) Al-coarse W; (b) Al-fine W CIPed only samples.

The SEM micrographs of Al-coarse W and Al-fine W after CIPed at 345 MPa are shown in Figure 4.4 (a) and (b), respectively. The dark gray particles are Al and white particles are W. These high magnification images demonstrate the interface between Al and W particles. Although both samples have the same volume fraction of Al and W, due to the much smaller particle sizes of fine W (< 1μm), and thus much larger surface area, the W become the "matrix" with trapped porosity inside it, at least in some parts of the sample, as seen in Figure 4.4(b). This trapped porosity inside agglomerated fine W particles can't be removed by CIPing and HIPing due to high strength of W particles. Coarse W particles did not demonstrate this trapped porosity because they are not agglomerated. The drastic mesostructural difference due to the high surface area-to-volume ratio of the fine W particles, compared to the coarse ones, plays an import role in mechanical testing which will be demonstrated later.

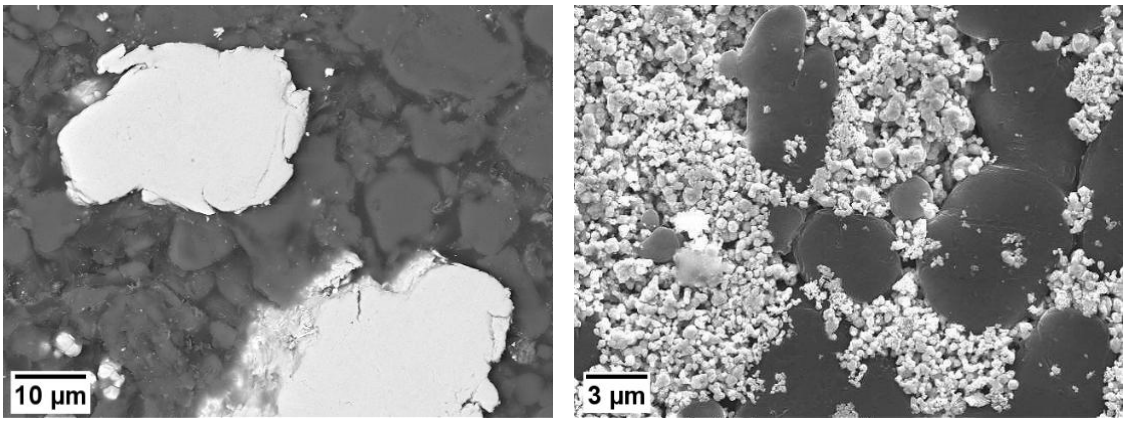

(a) (b)

Figure 4.4 (a) SEM micrographs of (a) Al-coarse W; (b) Al-fine W CIPed only samples.

Different processing conditions can also alter the mesostructure of the sample. Figure 4.5 demonstrated Al-coarse W samples after (a) CIPed at 48 MPa (W in white);

(b) CIPed at 345 MPa (W in white) and (c) CIPed at 345 MPa and then HIPed at 200 MPa and 500°C for 25 minutes (W in light gray).

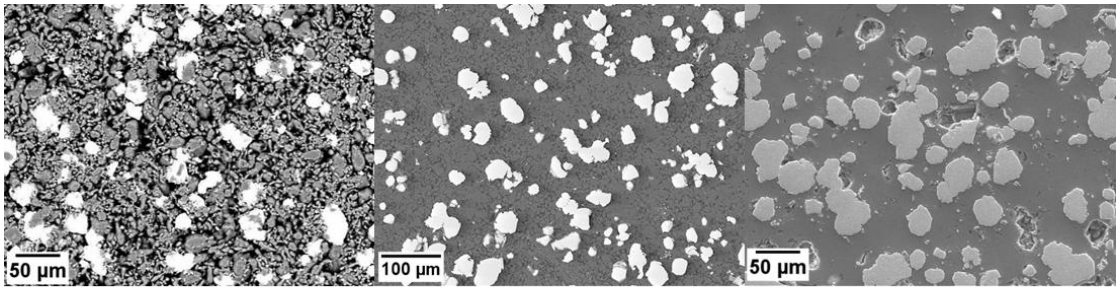

Figure 4.5 SEM micrographs of Al-coarse W particulate-reinforced granular/porous composites after different processing conditions: (a) CIPed at 48 MPa; (b) CIPed at 345 MPa and (c) CIPed at 345 MPa and HIPed at 200 MPa and 500°C for 25 minutes.

Pores (black spots) become less with increasing CIPing pressure (from (a) to (b)) and most pores have been removed after additional HIPing as shown in Figure 4.5 (c). The bonding between Al particles in Al matrix can affect the behavior of the materials under dynamic loading as well.

4.1.2 Quasistatic Tests

Quasistatic compression tests were performed by using a SATEC^{TM} Universal Materials Testing Machine (Instron) on CIPed-only samples. The load was applied at a nominal deformation strain rate of $0.001s^{-1}$. The corresponding stress–strain curves demonstrated maximum compressive strength 94 MPa for Al-fine W composite (CIPed at 345 MPa with porosity 29%). Al-coarse W composite (CIPed at 345 MPa with porosity 14%) had a maximum strength 150 MPa, and Higher-Porosity (HP) Al-coarse W composite (CIPed at 48 MPa with porosity 29%) had a very low strength 28 MPa (Figure 4.6). Under quasistatic loading, samples with lower porosity exhibited

higher strength while at the similar porosity, samples with fine tungsten particles demonstrated higher strength than samples with coarse tungsten particles. We attribute this behavior to the force chains created by fine W particles due to their agglomeration (Fig. 4.4(b)) which contained some porosity but maintained high strength.

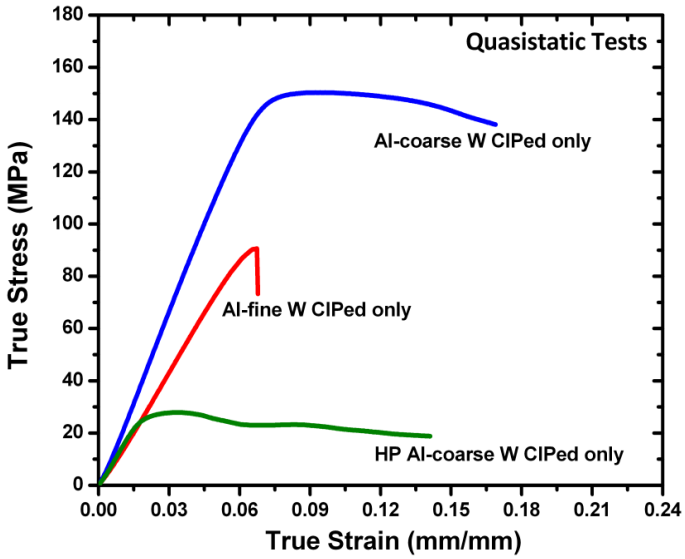

Figure 4.6 Stress-strain curves of CIPed-only, Al-W particulate-reinforced granular/porous composites after quasistatic tests.

4.1.3 Split Hopkinson Pressure Bar Compression Tests

Dynamic testing was performed using the split Hopkinson pressure bar which comprises three 19-mm-diameter bars made from C350 Maraging steel. The stresses and strains in the samples were calculated based on measured values of transmitted and reflected strains and elastic properties of Maraging steel. High speed camera Phantom v12 was used to get images of samples during dynamic tests and estimate nominal strains based on the change of length of samples. The test results and high speed images for three types of Al-W particulate-reinforced granular/porous composites are shown in Figure 4.7.

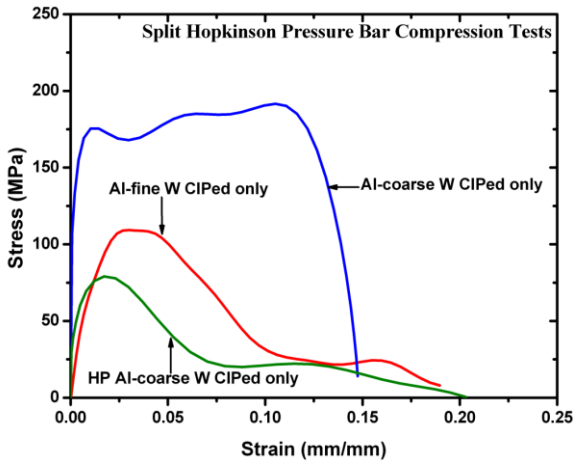

(a)

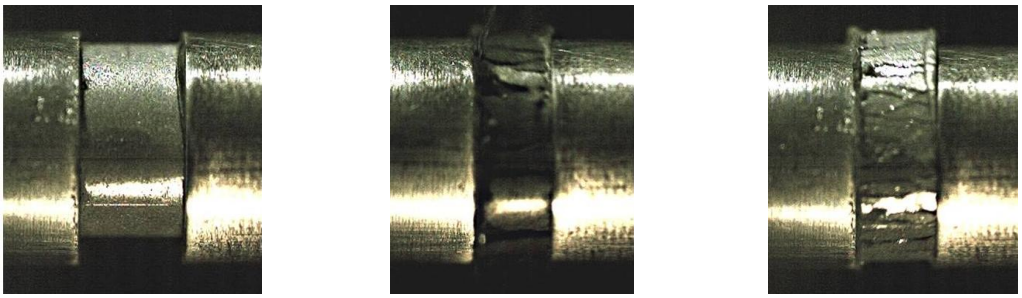

(b) (c) (d)

Figure 4.7 Results of CIPed-only, Al-W particulate-reinforced granular/porous composites after Split Hopkinson Pressure Bar Tests: (a) Stress-strain curves with strain rate about 1500 1/s; high speed images of the developing fracture at nominal strain 0.15 for (b) Al-coarse W samples (initial porosity 14%), (c) Al-fine W (average initial porosity 29%), and (d) Higher-porosity Al-coarse W sample (initial porosity 29%).

Similar to quasistatic tests, samples with lower porosity exhibited higher strength than samples with higher porosity at the same particles morphology. At the similar porosity, samples with fine W particles demonstrated higher strength than samples with coarse W particles as shown in Figure 4.7(a) similar to quasistatic tests. High speed images of the developing fracture at nominal strain 0.15 are shown in Figure 4.7(b), (c), and (d) from Al-coarse W, Al-fine W, and higher-porosity Al-coarse W samples, respectively. From Figure 4.7(b), the volume of sample based on geometrical sizes is 8% smaller than initial volume due to *in situ* densification. From

Figure 4.7(c), the volume of sample in the high speed image based on geometrical sizes is 18% larger than initial volume, probably due to micro/macrocraking. From Figure 4.7(d), the volume of sample based on geometrical sizes is 28% larger than initial volume, probably due to micro/macrocraking of in situ densified sample. The dynamic fracture of Al-W samples was due to axial cracks as shown in Figure 4.7 (c) and (d).

4.1.4 Drop-weight Testing

Another dynamic testing, drop weight tests, were also conducted using the DYNATUP 9250HV with an in-house modified anvil for the samples support. The strain rates of this test (in the order of 10^2 to 10^3 s^{-1}, depending on the impact velocity) are comparable to the Hopkinson bar tests. However, samples in drop weight tests can be deformed to higher strains, unlike in the Hopkinson bar tests. This allows the examination of the larger deformation (strains up to 0.5) and the post critical behavior of the materials. All five types of Al-W particulate-reinforced granular/porous composites mentioned in the Table 4.1 were tested. The results and corresponding high speed images are presented in Figure 4.8 to 4.11.

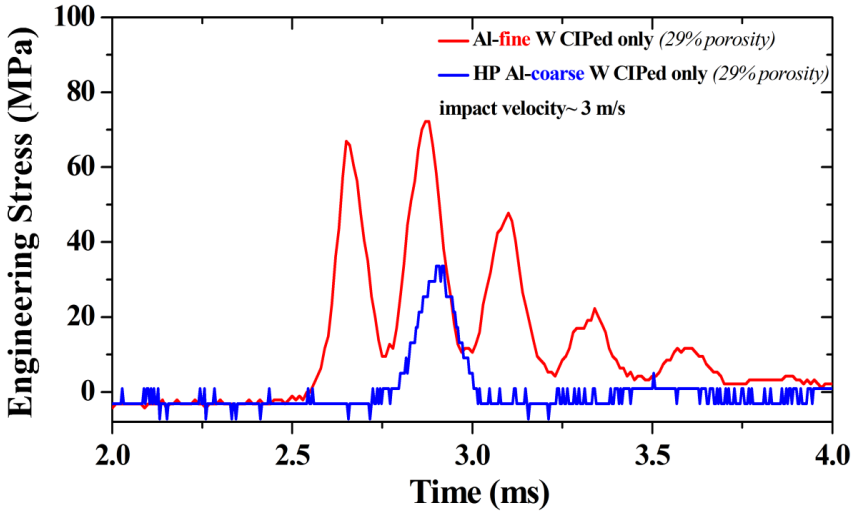

Figure 4.8 Engineering stress and time curves for CIPed only, coarse and fine W-reinforced Al porous/granular composites at the similar porosity. The drop weight velocity is about 3m/s.

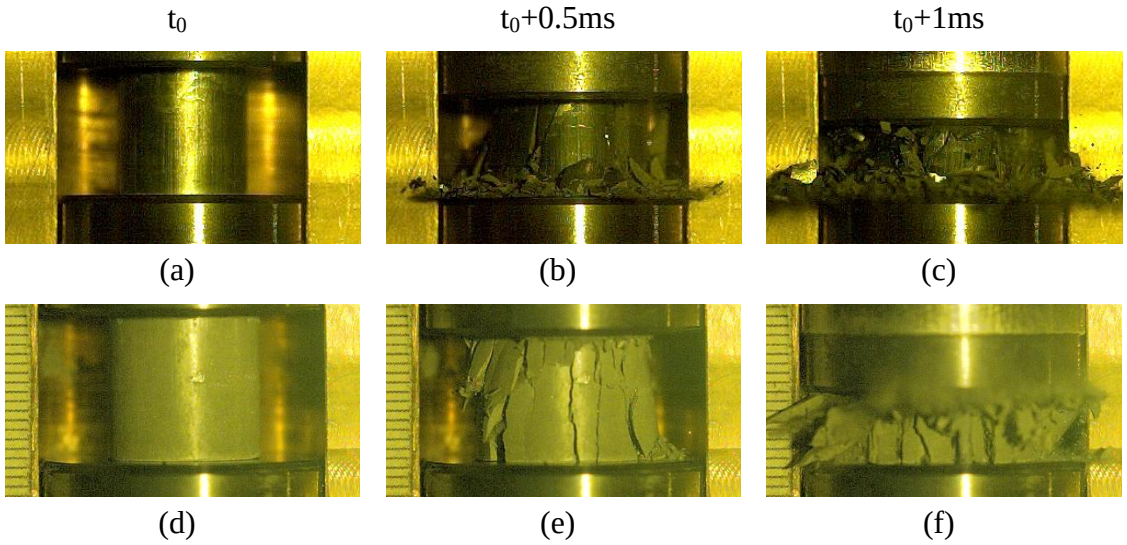

Figure 4.9 Series of high speed images of samples during drop weight tests at 0.5ms interval: (a) to (c): Al-fine W samples and (d) to (f): higher-porosity Al-coarse W samples.

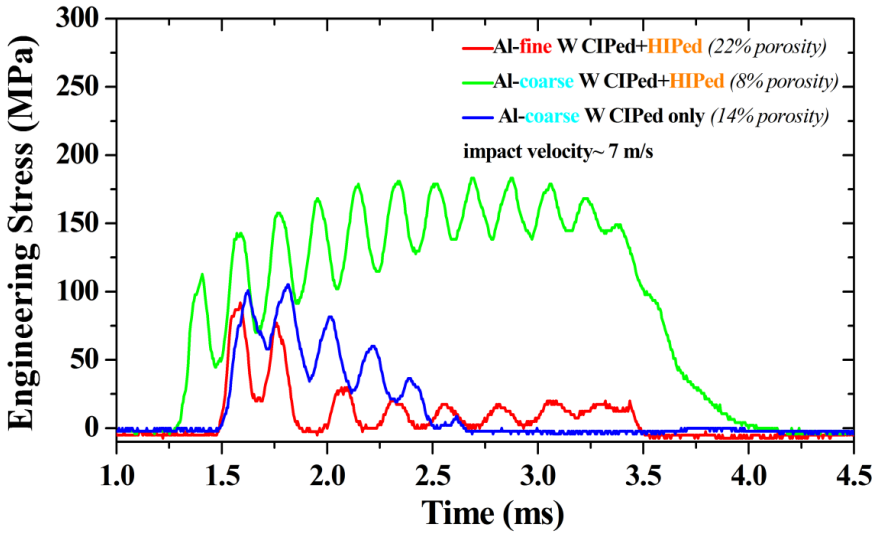

Figure 4.10 Engineering stress and time curves for CIPed+HIPed, coarse and fine W-reinforced Al porous/granular composites and CIPed only, Al-coarse W samples. The drop weight velocity is about 7m/s.

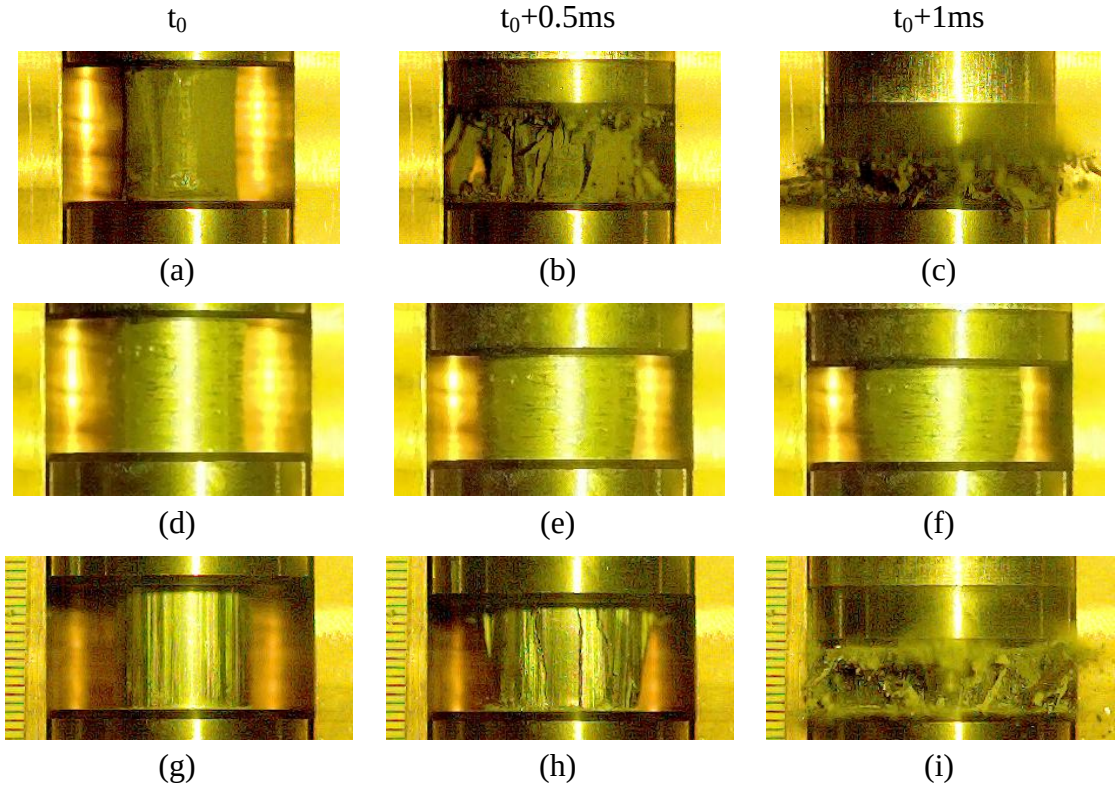

Figure 4.11 Series of high speed images of samples during drop weight tests at the 0.5ms interval: (a) to (c): Al-fine W samples CIPed+HIPed, (d) to (f): Al-coarse W samples CIPed+HIPed, and (g) to (i), Al-coarse W samples CIPed only samples.

Similar to previous tests, CIPed only samples with fine W particles demonstrated higher strength than sample with coarse W particles at the similar porosity. CIPed+HIPed samples showed higher strength than CIPed only samples. This may be due to the lower porosity and increase of Al matrix strength from bonding of Al particles. Similar to Hopkinson bar tests, the fracture of Al-W samples was due to axial cracks. Unlike other samples, Al-coarse W CIPed+HIPed samples demonstrated the uniform deformation, similar to the Al 6061-T6 samples observed in [1] and did not exhibit signs of fracture or shear localization.

Figure 4.12 (a) and (b) shows the SEM micrographs of CIPed only and CIPed+HIPed Al-coarse W samples after drop weight tests, respectively. Macrocracks in the Al matrix can be clearly seen in CIPed only samples. The higher porosity of the CIPed only samples makes the microcracks easier to initiate and propagate from the connection of pores. Some localized microcracks can be observed in CIPed+HIPed samples. But with less porosity and the bonding between Al particles, it is harder for them to propagate and form the global macrocracks. Also in some places, the elongation of the low strength Al particles between the high strength neighboring W particles can be observed (see Figure 4.12 (b)0. This suggests that Al particles are extruded between or squeezed by W particles during the dynamic loading.

Figure 4.13 and 4.14 show the SEM micrographs of CIPed only and CIPed+HIPed Al-fine W samples after drop weight tests, respectively. There is not much difference between CIPed only and CIPed+HIPed samples unlike Al-coarse W samples. This is probably due to localized bonding between Al particles in CIPed+HIPed samples since they are mostly surrounded by the much smaller W

particles. The agglomeration of fine W particles was observed in some areas inside macrocracks. This is explained by the force chains between fine metallic particles which can be responsible for the higher strength of samples with fine W particles [2].

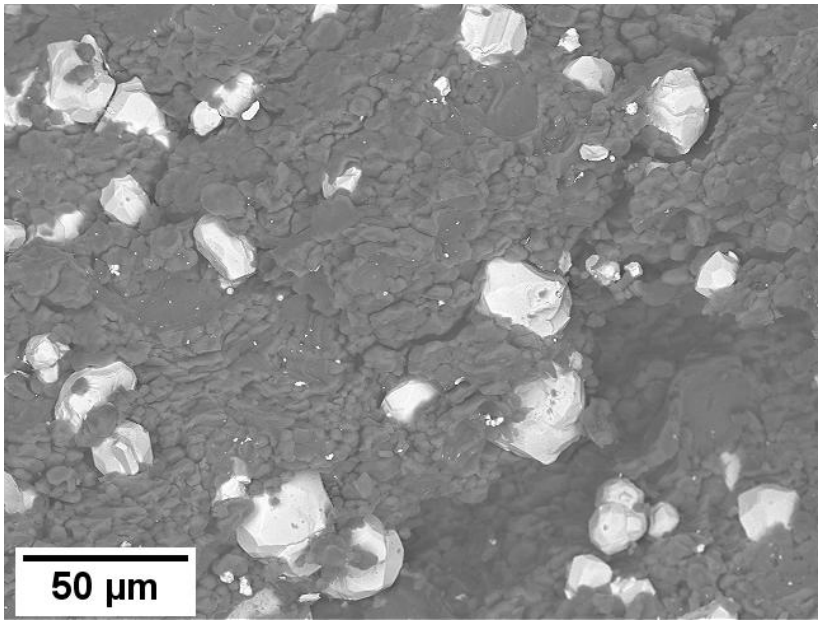

(a)

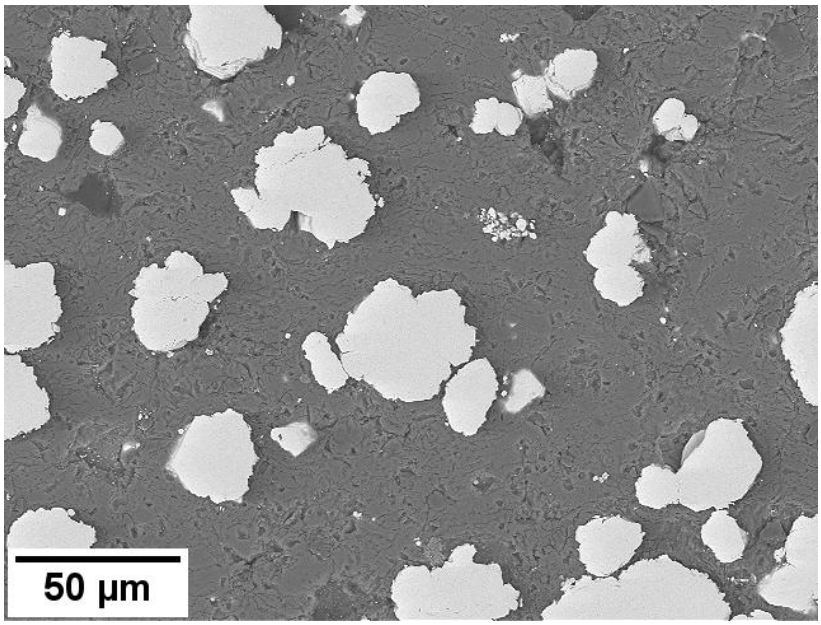

(b)

Figure 4.12 SEM micrographs of Al-coarse W samples after drop weight tests, (a) CIPed only and (b) CIPed+HIPed White particles are W and dark gray particles are Al.

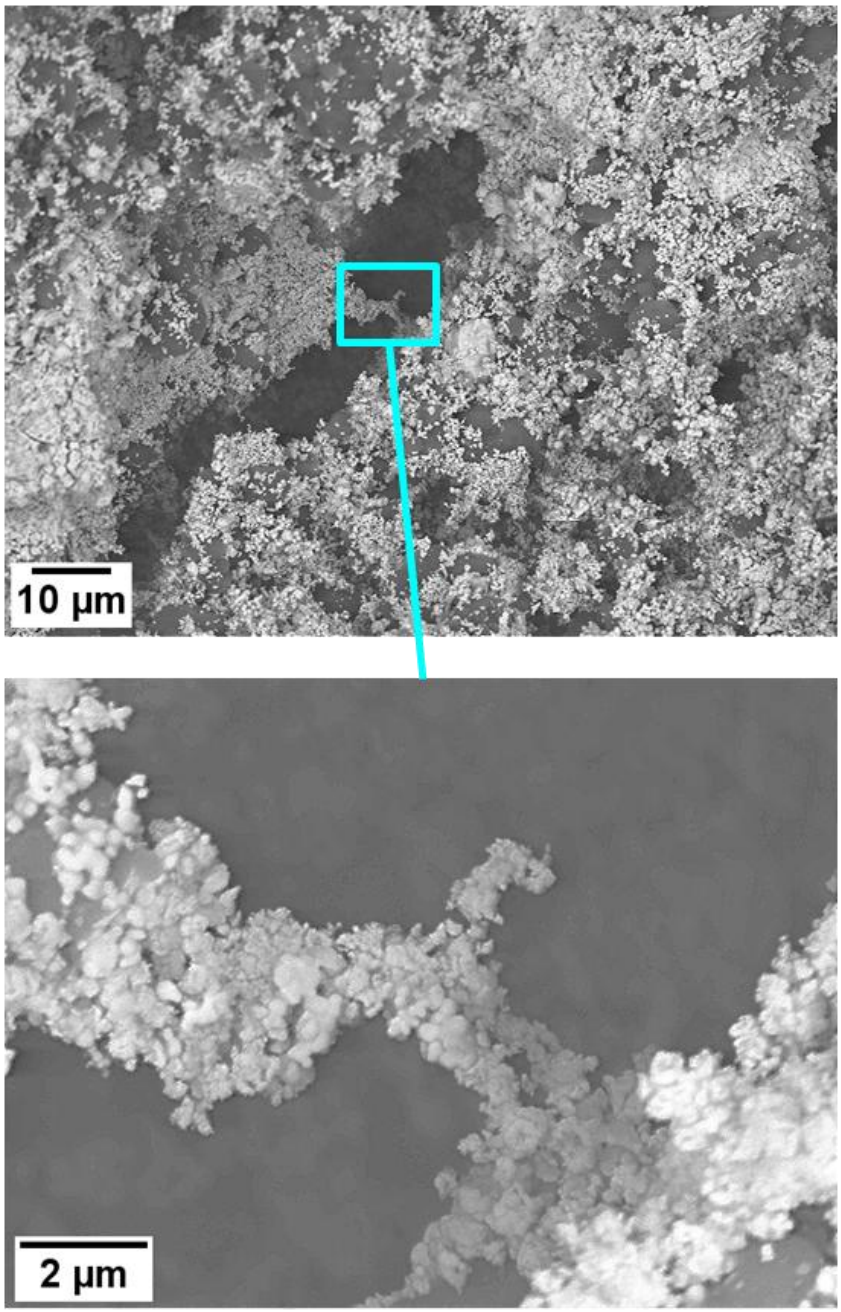

Figure 4.13 SEM micrographs of CIPed only Al-fine W samples after drop weight tests. One of the force chains between the fine W particles observed inside the macrocrack was shown in larger magnification. White particles are W and dark gray particles are Al.

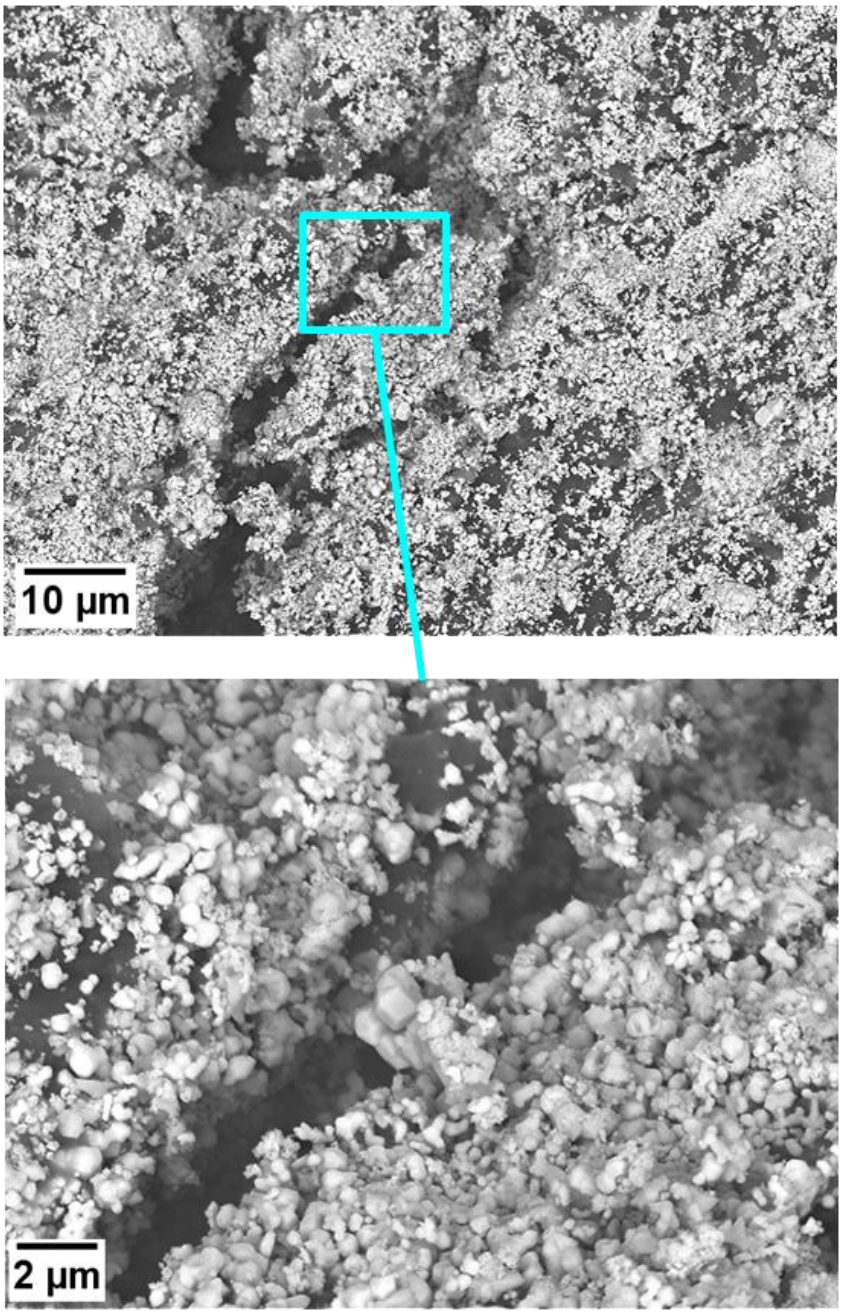

Figure 4.14 SEM micrographs of CIPed+HIPed only Al-fine W samples after drop weight tests. One of the force chains between the fine W particles observed inside the macrocrack was shown in larger magnification. White particles are W and dark gray particles are Al.

4.1.5 Summary

In this Section 4.1, the preparation and testing results (quasistatic and dynamic) of W particulate-reinforced Al granular/porous composites were presented. The following major features are demonstrated: (1) Maximum compressive stress of samples with fine W particles is higher than corresponding stress of samples with coarse W particles at the same porosity of Al matrix in quasistatic and dynamic tests at similar strain rates (compare Figure 4.6, 4.7(a) and 4.8). This can be explained by the influence of the "force chains" created by fine W particles which were less effective with large W particles, similar to the case of PTFE-Al-W granular composites [2, 3]; (2) The "force chains" can also be responsible for the higher resistance of fine W particles to the densification resulting in higher porosity of samples with fine W powder after CIPing; (3) Dynamic fracture of Al-W samples was due to axial cracks; (4) Peak compressive stress in dynamic testing was higher than in quasistatic tests due to *in situ* densification in dynamic conditions prevailing over fracture kinetics. We can see that behavior of samples is determined by the morphology of rigid W particles and the porosity and bonding strength of Al matrix.

4.2 Al-W Fiber-reinforced Composites

4.2.1 Sample Preparation

High density granular/porous composites made from Al powder (-325 mesh, Alfa Aesar) and W wires (200 μm diameter and 4 mm long, A-M system) were cold isostatically pressed at 345 MPa with identical mass ratio as Al-W granular composites described in the previous section (23.8 wt% Al and 76.2 wt% W, by

weight corresponding to the volume ratio 69% and 31%, respectively, theoretical solid density 7.8 g/cm^3). W wires are well mixed with Al powder and randomly distributed inside the sample to ensure isotropic properties and increase strength. After CIPing, some samples underwent subsequent HIPing at 500℃ and 200 MPa to investigate the role of bonding between Al particles. Prior to HIPing, samples were encapsulated in the Al jacket and the whole assembly was vacuum sealed. The density and porosity of samples after processing are listed in Table 4.2. Figure 4.15 (a) demonstrates the same amount of W wires required for one sample randomly distributed inside a glass tube with similar diameter (15 mm) to the actual sample diameter after CIPing. Figure 4.15 (b) and 4.15 (c) shows a samples after CIPing and HIPing respectively.

Table 4.2 Properties of Al-W wires samples after processing.

Sample Type	**CIPing Pressure (MPa)**	**Density (g/cm^3)**	**Porosity (%)**
(a) Al-W wires (CIPed Only)	345	6.88	11.79
(b) Al- W wires (CIPed+HIPed)	345	7.37	5.46

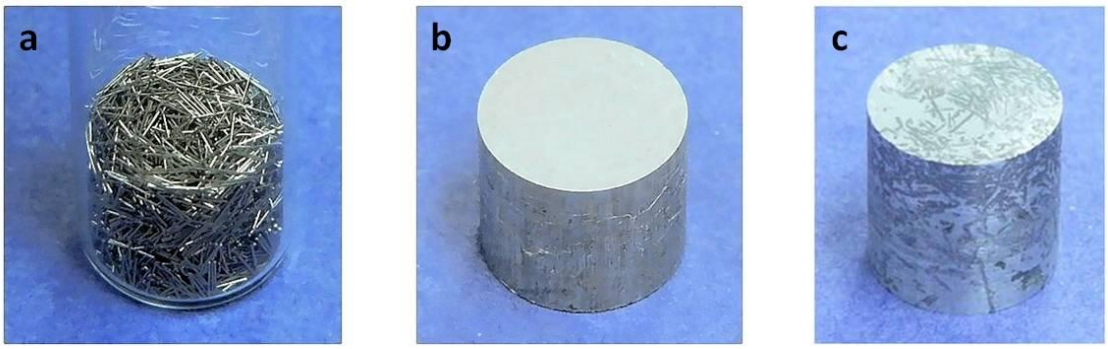

Figure 4.15 (a) Tungsten wires required for one sample randomly distributed inside a glass tube with 15 mm diameter, similar to the sample diameter; (b) sample after CIPing; (c) sample after CIPing and HIPing.

To increase the strength of Al-W composites, solid samples with thin Al tubes and W wires) arranged in axial and hoop direction (close to 50/50 ratio) were

fabricated with the same composition. It should be mentioned that commercially available W mesh does not allow the required volume content of W.

Two thin 6061-T6 Al tubes, served as inner and outer tubes having 0.5 mm wall thickness and different diameters (inner tube with 7.5 mm inner diameter and 8.5 mm outer diameter; outer tube with 9.8 mm inner diameter and 10.8 mm outer diameter) were machined first from the tubes of larger sizes and annealed. A steel rod was placed tightly inside the Al inner tube to prevent the buckling of the tube. 71 W rods with 150 mm length and 200 µm diameter (A-M system) were axially placed around the inner Al tube. The spacing between W rods was 183 µm and a template was used to maintain their periodicity and spacing. After W rods were aligned axially, W wires with 200 µm diameter were wrapped around the aligned W rods and the inner Al tube with spacing along axis of 242 µm. This creates a mesh-like structure wrapping around the inner Al tube. The whole structure was then put into the outer Al tube and encapsulated in a rubber tube for CIPing at 345 MPa to stabilize the sample. After CIPing, the sample was removed from rubber tube and encapsulated in the vaccum sealed Al jacket for HIPing. During the HIPing soft Al (due to high temperature) was pushed from outside to fill empty space in the W structure left after CIPing. After HIPing and removing the Al jacket, another set of W "mesh" was built around the sample with the similar procedure. After second HIPing, the samples were machined to remove the steel inner rod and excessive outer Al jacket. Figure 4.16 demonstrates one of the samples after machining and its corresponding microstructure.

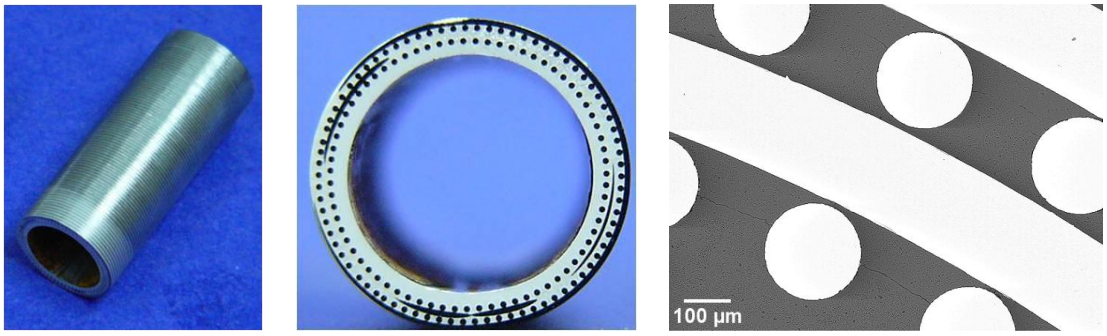

(a) (b) (c)

Figure 4.16 Side view (a), front view (b) and (c) microstructure of the sample after two HIPing cycles. No reaction between Al and W was found after processing

Being HIPed twice, the Al alloy matrix of the samples has been thoroughly annealed and lost the strength characteristic to initial Al6961-T6 alloy. To explore the role of Al matrix hardness under the dynamic tests, three samples (H1, H2 and H3) were heat treated so the Al matrix can regain its T6 condition strength. The standard heat treatment of Al matrix was performed in a tube furnace with nitrogen purging. After water quenching at room temperature from solution treatment at 530℃ for 25 minutes, samples went through artificial aging at 176℃ in vacuum for 480 minutes and then were air-cooled. Another three samples (1, 2 and 3) without heat treatment were used as the control group. Their dimensions and microhardness can be found in Table 4.3. The standard heat treatment resulted in significant increases of the microhardness of Al matrix from about 600 MPa to 1000 MPa, which is comparable to the microhardness of commercial Al6061-T6 alloy.

Table 4.3 Properties of solid Al-W wire mesh samples before dynamic testing.

Sample	Length (mm)	Outer Ø (mm)	Inner Ø (mm)	Weight (g)	Density (g/cm^3)	Al alloy Microhardness (MPa)
1	5.06	9.97	7.52	1.25	7.4	594.6±11
2	5.02	9.99	7.49	1.25	7.3	578.6±16
3	4.95	10.56	7.41	1.34	6.3	588.7±12
H1	5.00	10.11	7.46	1.27	7.0	1035.3±28
H2	5.00	10.14	7.45	1.26	6.8	1008.8±23
H3	4.99	10.12	7.48	1.27	7.1	1020.5±25

4.2.2 Quasistatic Tests

Samples from Al and W wires isotropically placed in the sample (Fig. 4.15), after CIPing and CIPing+HIPing, were axially loaded in compression using Instron 850 universal testing machine at 10^{-3} 1/s strain rate. The results are shown in Figure 4.17. CIPed only samples initially exhibited nonlinear behavior, while CIPed+HIPed samples demonstrated linear behavior with higher initial modulus at low strains. This nonlinear behavior observed in the CIPed only samples is probably due to the *in situ* densification of Al matrix. In these samples, Al particles were not bonded and their porosity was higher than CIPed+HIPed samples (see Table 4.2).

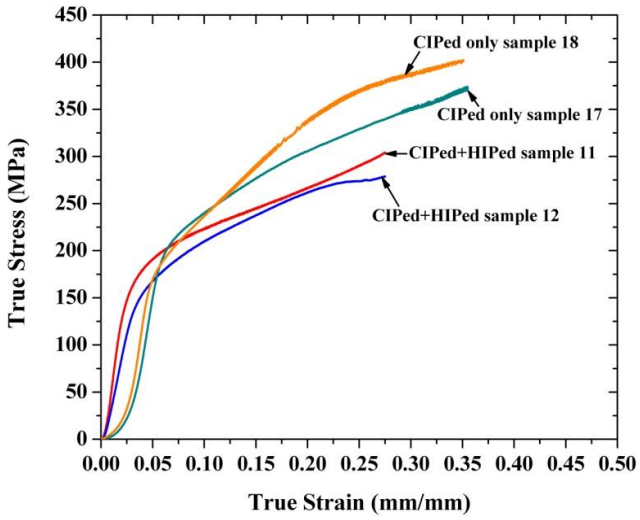

Figure 4.17 Stress-strain curves of Al-W wires composite with CIPed Only and CIPed+HIPed after quasistatic tests.

After the strain reached 0.07, the true stress of CIPed only samples overshoots the strength of CIPed+HIPed samples. The mechanism responsible for this behavior may be related to higher strain hardening of Al powder in CIPed only samples compared to CIPed+HIPed samples demonstrated by measurements of microhardness after the tests. Also Al powderswere annealed during the HIPing resulting in their lower strength. Strain hardening of CIPed only samples can be also caused by densification and rearrangements of W wires which was not possible in CIPed+HIPed samples with solidified Al matrix. After tests CIPed+HIPed samples developed shear cracks, while CIPed only samples did not develop them.

Figure 4.18 and 4.19 shows the CIPed only and CIPed+HIPed sample after quasistatic tests respectively. The dot lines in Figure 4.18(a) and 4.19(a) indicate where the samples were cut by the wire-EDM. These two figures demonstrated that CIPed only samples have better resistance to shear localization under quasistatic deformation than CIPed+HIPed samples.

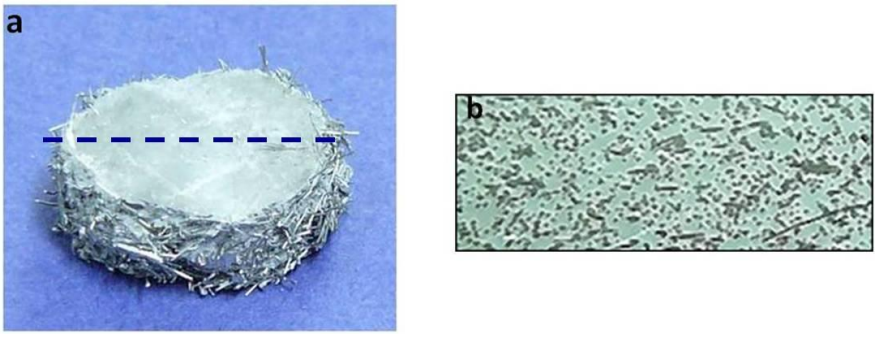

Figure 4.18 (a) The CIPed only sample after quasistatic tests with strain=0.50; (b) the cross section of the sample. No visible shear cracks were developed at this strain.

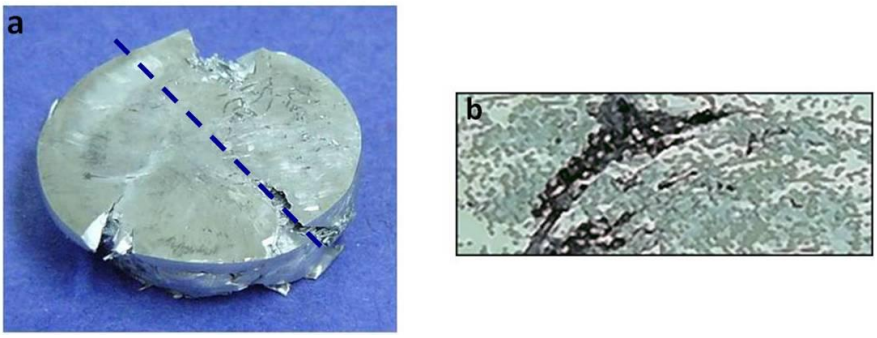

Figure 4.19 (a) The CIPed+HIPed sample after quasistatic tests with strain=0.51; (b) the cross section of the sample. Shear cracks were well developed at this strain in a sharp contrast with the CIPed only sample.

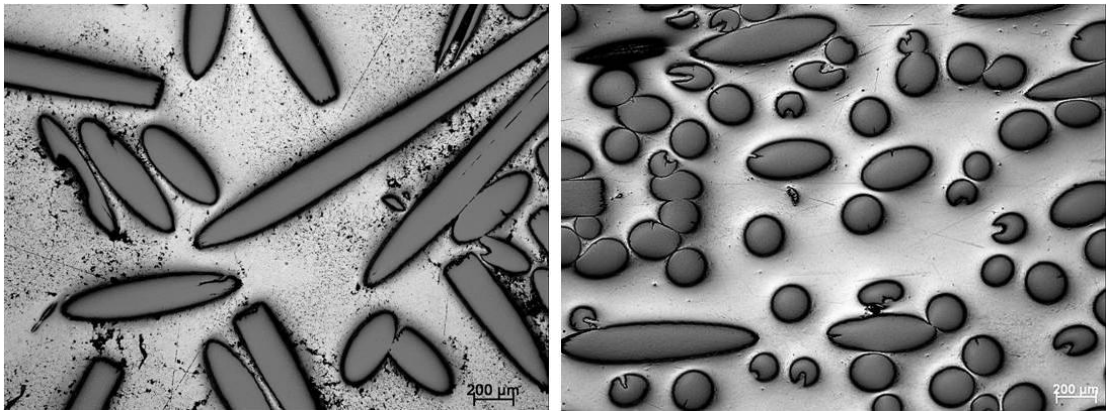

(a) (b)

Figure 4.20 The microstructure of the CIPed only sample (a) before quasistatic tests; (b) after quasistatic tests. Pores inside the Al matrix were compacted and closed, which led to the densification of the sample.

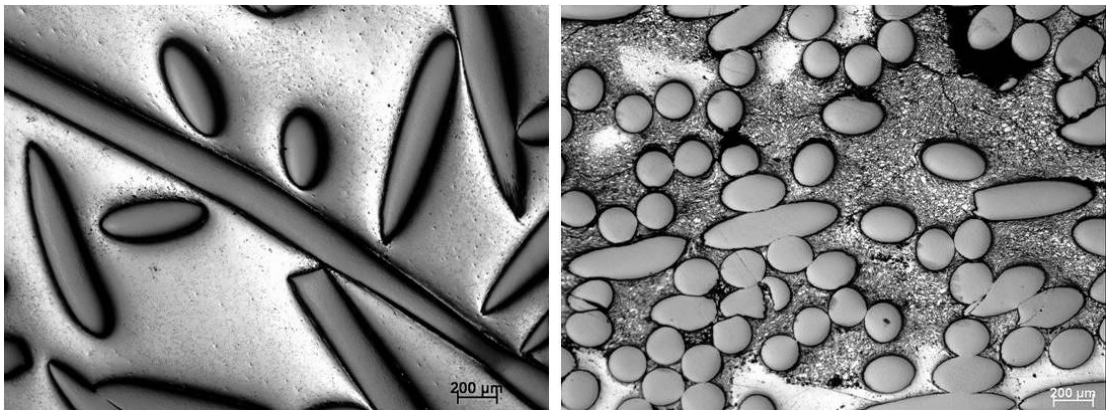

(a) (b)

Figure 4.21 The microstructure of the CIPed+HIPed sample (a) before quasistatic tests; (b) after quasistatic tests. The aluminum matrix was deformed heavily and began to separate, which led to shear cracks.

The change of the microstructure after quasistatic tests can be seen in Figure 4.20 and 4.21. The densification of Al matrix in CIPed only samples and the bulk distributed fragmentation of Al matrix of CIPed+HIPed sample can be observed. The latter resulted in macrocracks in CIPed+HIPed sample. The higher strain hardening in CIPed only sample is the probable explanation to its higher resistance to shear localization than CIPed +HIPed samples.

4.2.3 Split Hopkinson Pressure Bar Compression Tests

Dynamic tests of the CIPed+HIPed Al-W samples wire periodic mesh of W wires placed in axial and hoop directions as described above were performed by Split-Hopkinson pressure bar. The high speed images of each sample are presented in Figure 4.22. The stress-strain and strain rate-strain curves are shown in Figure 4.23 (a) and (b), respectively.

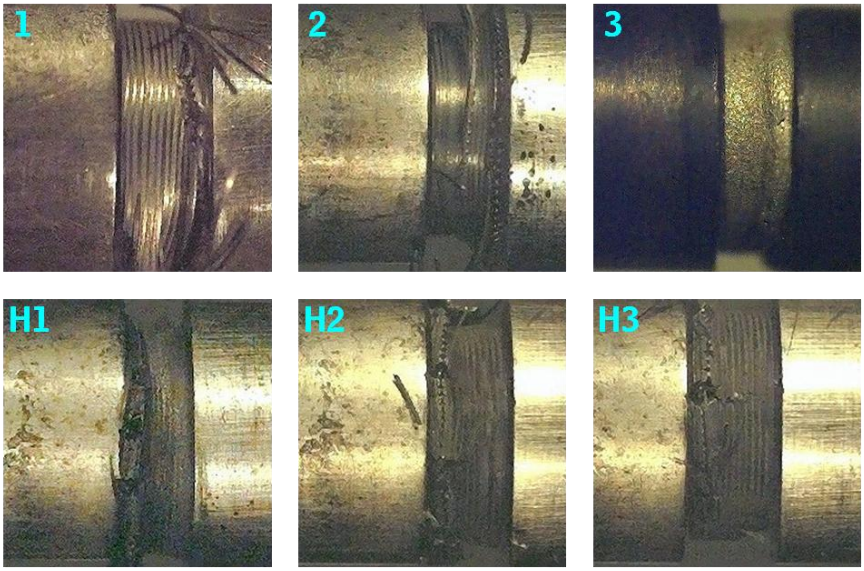

Figure 4.22 High speed images of Samples 1, 2, 3 and Samples H1, H2 H3 samples during Hopkinson Bar Tests.

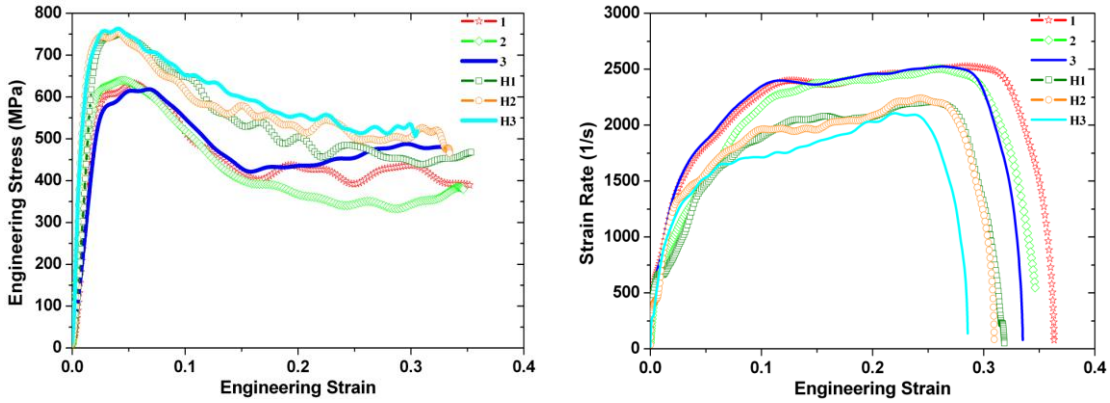

(a) (b)

Figure 4.23 Stress-strain (a) and strain rate-strain (b) curves of Samples 1, 2, 3 and Samples H1, H2 H3 under dynamic loading. Samples with higher hardness of Al matrix (Samples H1, H2 H3) demonstrated higher compressive strength and lower strain rate.

Samples with higher hardness of Al matrix demonstrated higher compressive strength (~19% higher) at slightly lower strain rate (~14% lower) compared to samples without heat treatment. This indicated that the higher dynamic strength of the heat treated samples is not due to the higher strain rates. The results are consistent in three

different tests for each type of samples (heat-treated and non-heat-treated). Lengths of the samples after tests were measured and engineering strain were calculated. Samples with higher hardness of Al matrix have lower engineering strain (0.30) than samples with softer Al matrix (0.34).

4.2.4 Drop-weight Testing

The dynamic strength and fracture behavior were investigated at strain rate 1000 1/s under drop weight tests with drop weight velocity equal to 10 m/s. Instron DYNATUP 9250HV impact test instrument were used along with a Phantom v12 high speed camera. The corresponding experimental setup can be found in Chapter 3.

The stress-time curves are shown in Figure 4.24. The CIPed+HIPed samples demonstrated slightly larger strength and strain hardening rates than CIPed only samples. The corresponding high speed images are shown in Figure 4.25. Pulverization of Al matrix can be observed in CIPed only samples (Figure 4.25, from (a) to (c)) while shear macrocracks can be seen in CIPed+HIPed samples (Figure 4.25, from (d) to (f)).

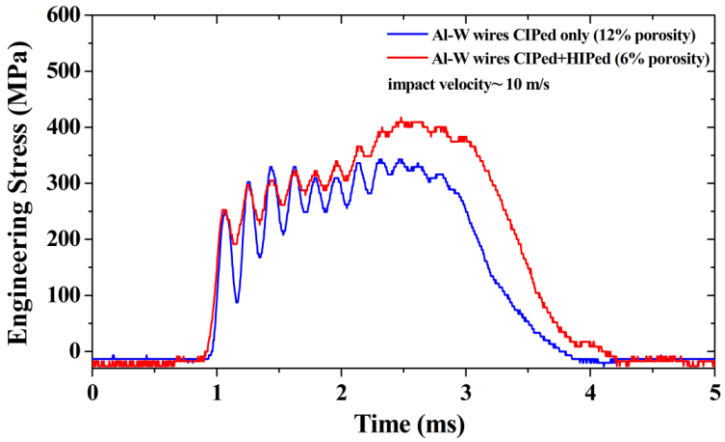

Figure 4.24 The stress-time curve of the CIPed only and CIPed+HIPed samples after drop weight tests.

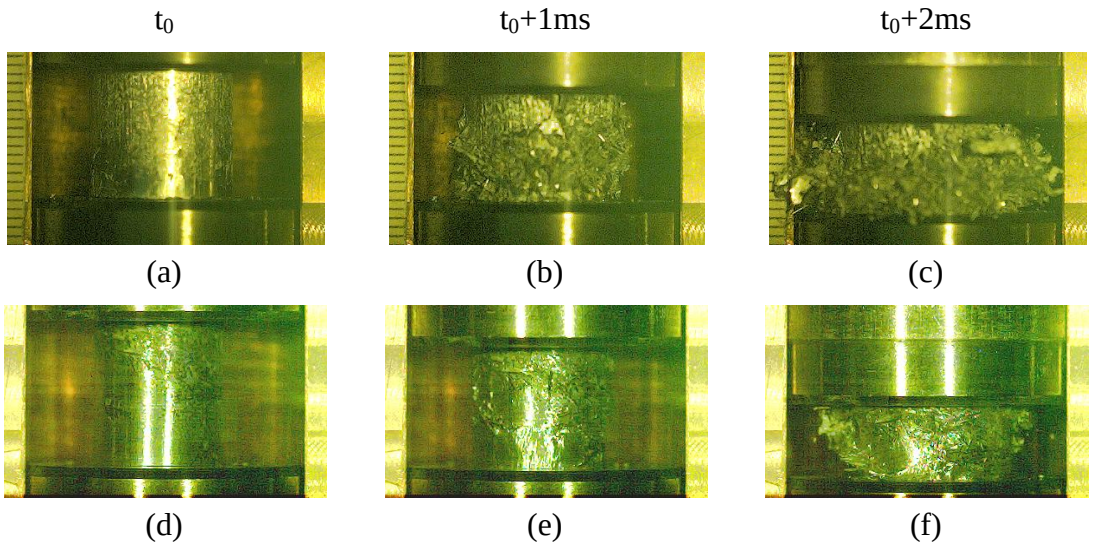

Figure 4.25. Series of high speed images of samples during drop weight tests at 1ms interval: (a) to (c): Al- W wires CIPed only and (d) to (f): Al- W wires CIPed+HIPed samples. Pulverization of Al matrix can be observed in CIPed only samples and shear macrocracks can be seen in CIPed+HIPed samples.

The microhardness of Al matrix was measured at each stage (as-received, after processing, and after testing) and the results are shown in Table 4.4. The Al matrix is annealed during HIPing and thus CIPed+HIPed samples have less strength than CIPed only samples. We can see from the Figure 4.24 that the CIPed+HIPed samples demonstrated tendency to higher strain hardening rates than CIPed only samples. This is probably because the densification of CIPed only samples occurred first before the hardening initiated in these tests.

Table 4.4 Microhardness of the Al matrix at each stage (as-received, before and after testing).

	Microhardness (MPa)
Pure Al Powder (as received)	184.12±6.04
CIPed Only (Post-Processing)	418.42±4.71
CIPed+HIPed (Post-Processing)	314.14±10.93
CIPed Only (Post Drop Weight Test)	510.60±19.07
CIPed+HIPed (Post Drop Weight Test)	518.12±8.52

The CIPed only and CIPed+HIPed samples and their cross sections after drop weight tests are shown in Figure 4.26 and 4.27, respectively. The dot lines in Figure 4.26(a) and 4.27(a) are where the samples were cut by the wire-EDM. Shear macrocracks are well developed in CIPed+HIPed sample (Figure 4.27), while no shear macrocracks are observed in CIPed only sample (Figure 4.26).

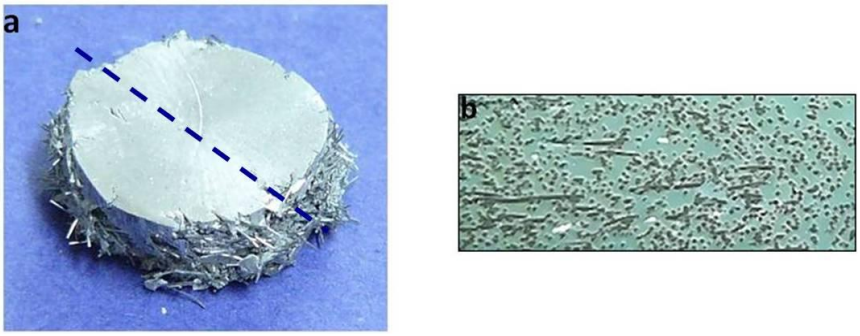

Figure 4.26 (a) The CIPed only sample after drop weight tests with engineering strain 0.46; (b) the cross section of the sample. No visible shear cracks were developed at this strain.

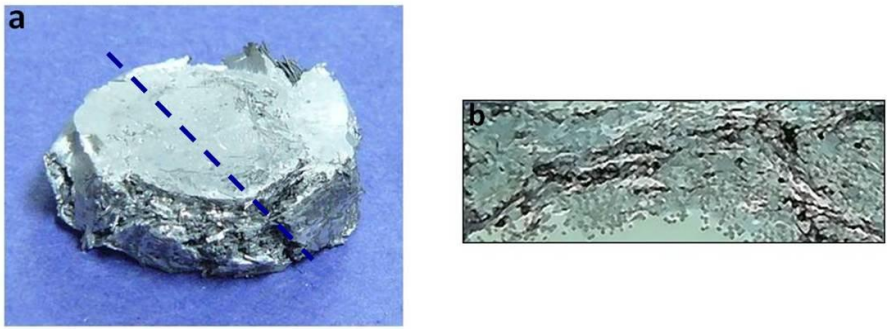

Figure 4.27 (a) The CIPed+HIPed sample after drop weight tests with engineering strain 0.57; (b) the cross section of the sample. Shear cracks were developed at this strain.

The changes of the microstructure before and after tests were investigated using optical kicroscopy with lower magnification (see Figure 4.28 and 4.29 for CIPed only and CIPed+HIPed, respectively) and by SEM with higher magnification to focus on the Al matrix (see Figure 4.30 and 4.31 for CIPed only and CIPed+HIPed,

respectively). The densification of Al matrix for CIPed only samples and the heavy deformation for CIPed+HIPed sample, which led to macrocracks, can be observed in those figures.

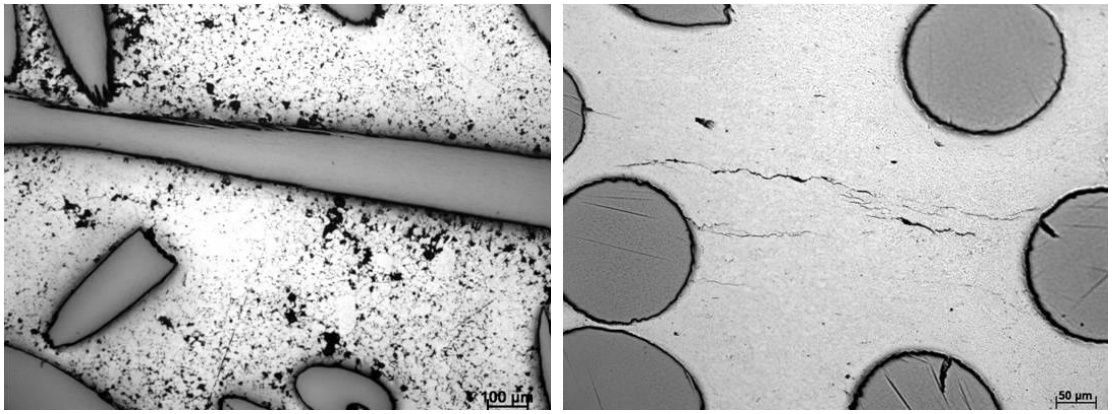

(a) (b)

Figure 4.28 The microstructure of the CIPed only sample (a) before drop weight tests; (b) after drop weight tests. Similar to quasistatic tests, pores inside the Al matrix were compacted and closed, which led to the densification of the sample. Yet shear microcracks began to develop between tungsten rods at this strain (0.46).

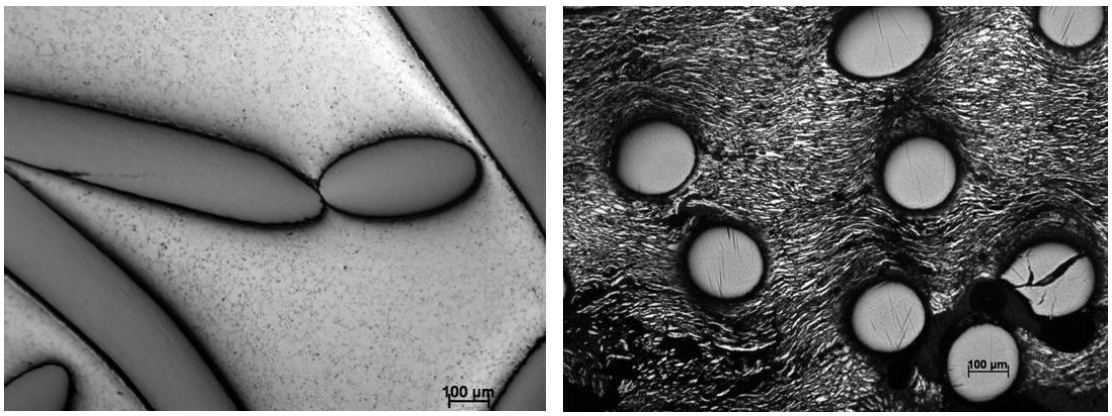

(a) (b)

Figure 4.29 The microstructure of the CIPed+HIPed sample (a) before drop weight tests; (b) after drop weight tests. Similar to quasistatic tests, the Al matrix was deformed heavily and began to separate, which led to shear cracks.

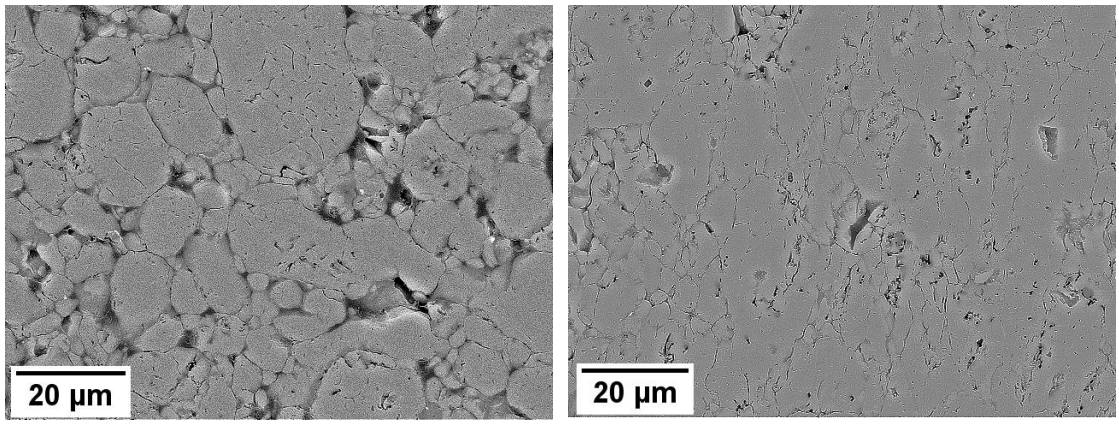

(a) (b)

Figure 4.30 The SEM image of the CIPed only sample: (a) before the drop weight test, and (b) after the drop weight test. Many pores in the Al matrix after CIPing were closed after drop weight tests. Besides the densification of Al matrix, some elongated and deformed Al particles can be observed.

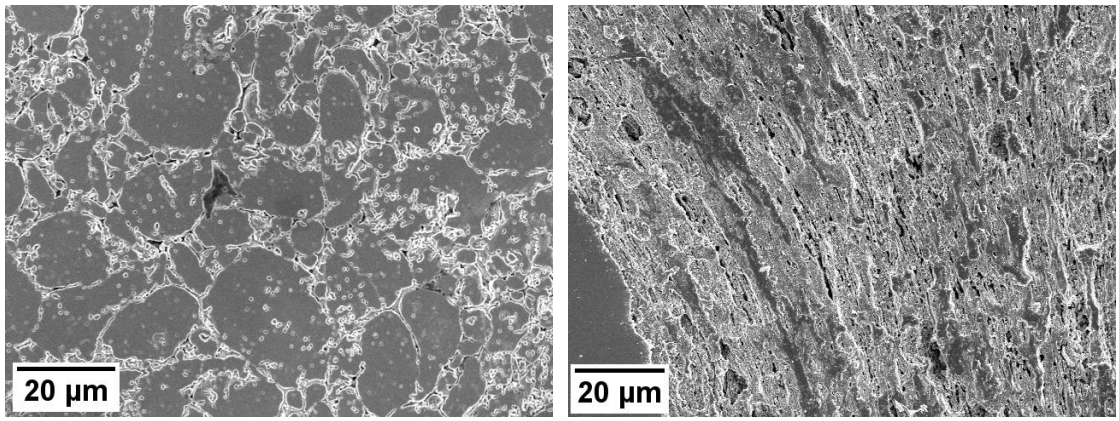

(a) (b)

Figure 4.31 The SEM image of the CIPed+HIPed sample: (a) before the drop weight test, and (b) after the drop weight test. The Al particles were not heavily deformed after CIPing and HIPing in comparison with high strain deformation after drop weight tests.

CIPed only samples with randomly distributed W rods showed the resistance to shear banding during in-situ densification in both quasistatic and dynamic tests. As long as solid density is reached, the shear instability is quickly developed. On the other hand, CIPed+HIPed samples with random distribution of W rods showed the development of shear bands and the formation of macrocracks in both quasistatic and

dynamic tests due to the heavy deformation of Al matrix. The bonding between "soft" Al particles clearly facilitated the shear localization in both quasistatic and dynamic tests.

4.2.5 Explosively Driven Fragmentation Tests

The explosively driven fragmentation tests were conducted in the Cavendish Laboratory, Cambridge University, UK and details regarding the experimental setup can be found in [4] and in the previous chapter. The specimen for this test has to be the shape of a ring so it can be placed around the Cu tube (see Figure 3.12). The same composition of Al-W granular/porous composite rings (24% Al and 76% W by weight, 69% and 31% by volume, and a theoretical density of 7.8 g/cm^3) with 4 mm height, 30 mm outer diameter (O.D.) and 22 mm inner diameter (I.D.) were prepared by Cold Isostatic Pressing (CIPing) at pressure 345 MPa. The mesostructure of the samples were tailored by using different particle sizes of Al powder (coarse: -325 mesh and fine: 4.5~7 μm, both from Alfa Aesar), and different morphologies of W (powder: -325 mesh with polyhedral particles from Alfa Aesar and W rods: 200 μm diameter with 4 mm length from A-M system). We consider that the elongated geometry of W rods may influence the pulverization process of Al due to differences in the dynamic behavior of W rods in comparison to W particles during the fragmentation process. To investigate the role of bonding between Al particles, half of the samples were Hot Isostatically Pressed (HIPed at pressure 200 MPa and temperature 500℃) after CIPing. Samples were pressed to correct dimensions with 8~15% porosity and did not require further machining. An example of a sample after processing is shown in Figure 4.32(a).

Three smaller rings (19 mm O.D. and 13 mm I.D.) with the same height were made from a mixture of fine Al and W powders (CIPed only) and were used in pilot experiments. For comparison, solid rings with similar sizes and densities were manufactured from Stainless Steel (SS) 304.

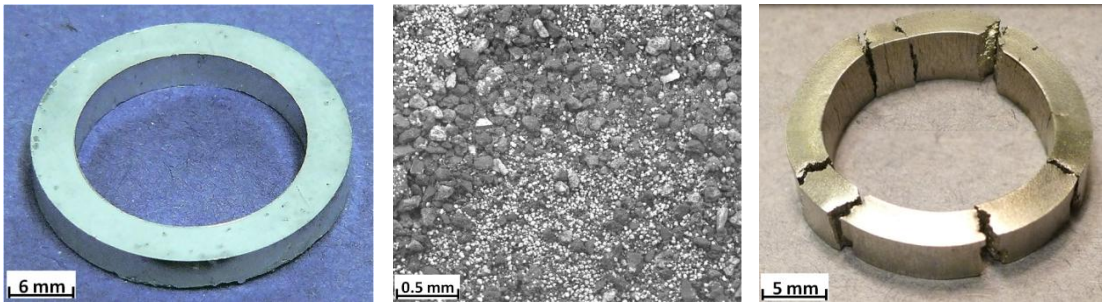

(a) (b) (c)

Figure 4.32 (a) One of the Al-W granular/porous composite rings before the test; (b) The fragments collected from one of the small rings (fine Al-W powder, CIPed only); (c) The SS 304 fragments after the test.

The recovered and cleaned fragments from the pilot experiments can be seen in Figure 4.32(b) and (c). The fragment sizes comparison between these two clearly demonstrates the inner mesostructure of Al/W samples played a major role in the generation of finer debris.

The PDV records of fragments corresponding to the small ring samples and results of numerical simulations are shown in Figure 4.33. The heterogeneous Al-W samples with unbonded Al particles demonstrated a fairly consistent behavior in expansion velocity.

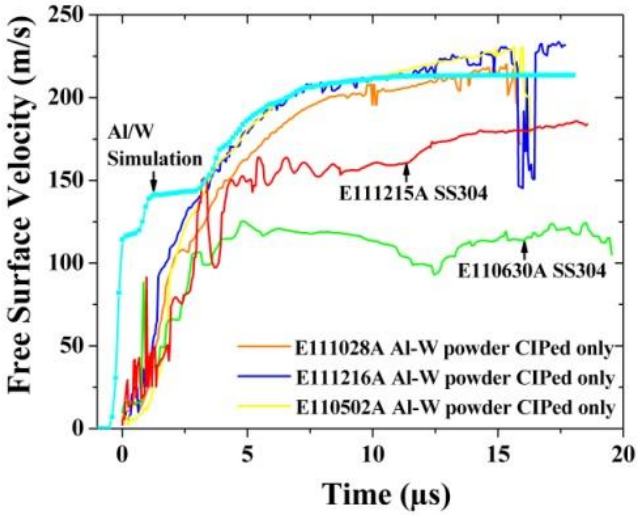

Figure 4.33 The PDV records of the small ring tests with SS304 and the CIPed Al-W samples with fine Al/coarse W powder as well as results of numerical simulations of Al/W samples; and

Particle size analysis of the recovered fragments (including Al and W particles) for the small ring Al-W samples was performed using laser diffraction and is presented in Figure 4.34 (a). This showed that about 90% of fragments were smaller than 100 microns compared to the characteristic fragment size of several millimeters in the stainless steel samples. X-ray Powder Diffraction (XRPD) was also performed on the collected fragment to investigate the possible intermetallic reaction between the Al and W and the results are shown in Figure 4.34 (b). No intermetallic reaction between Al and W was found after tests.

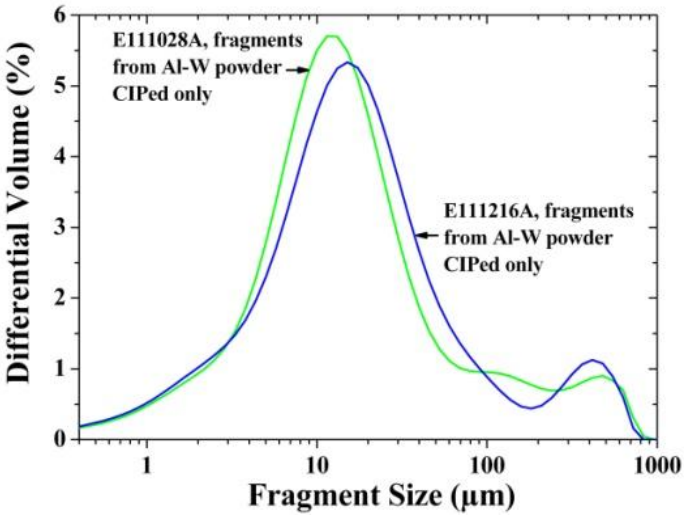

(a)

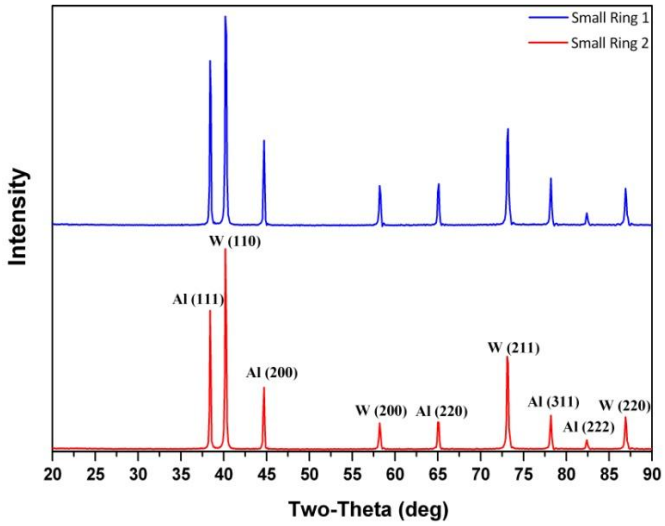

(b)

Figure 4.34 (a) the particle size distribution of the recovered fragments from the small-rings sample 1 and 2 (fine Al/coarse W powder composites). (b) the XRPD results of the small-ring sample 1 and 2. No intermetallic reaction between Al and W was found after tests.

PDV records corresponding to samples made with W rods are shown in Figure 4.35. It is difficult to distinguish between the PDV traces of samples with different particle sizes of Al and bonding. This suggests that the global response of these composites with W rods under this loading condition is not very sensitive to the Al particle sizes or their bonding.

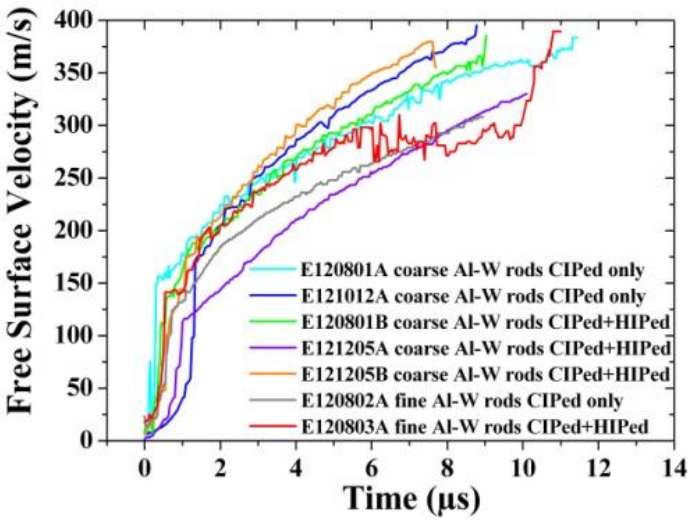

Figure 4.35 The PDV records of samples with Al powder and W rods show similar free surface velocity profiles in all samples.

X-ray Powder Diffraction (XRPD) was performed on the recovered fragments from coarse Al-W wires (Figure 4.36(a)), and fine Al-W wires (Figure 4.36(b)). The results demonstrated that the intermetallic reaction did not occur during the dynamic loading for those samples. In all samples with W rods, Al particles were stripped from the W rods before the particle size analysis. The particle size distribution of the recovered fragments excluding the W rods (Figure 4.37(a) and (b)) showed that nearly all (90-98%) of the fragments were smaller than 100 microns. This is significantly smaller than the fragments generated from solid SS304 samples with similar density [4]. In addition, the as-received coarse and fine Al powder were analyzed in the same manner and the results are also presented in the corresponding figures. An increase in the amount of small size fragments in comparison with the size distribution in initial powders was observed. For example, the percentage of fragments with a size less than 10 microns in the sample with the coarse Al powder samples grew from 22% (initial)

to 28-35% (after test) and the number of fragments with a size smaller than 4.5 microns in the samples with fine Al powder grew from 8% (initial) to 11-15% (after test), indicating that some Al particles were likely fractured during the tests.

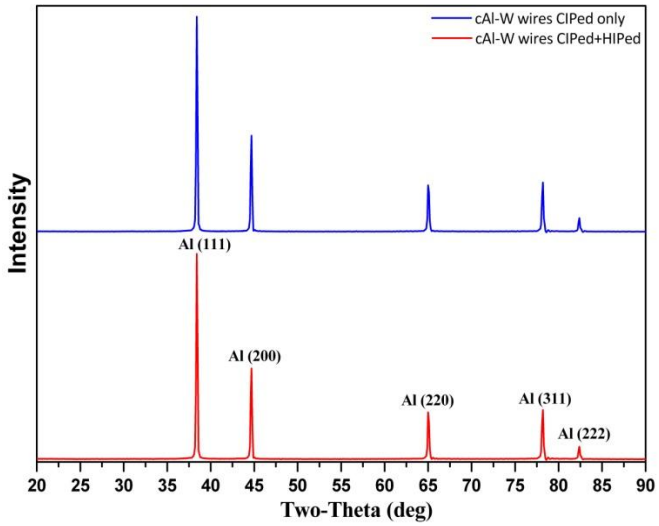

(a)

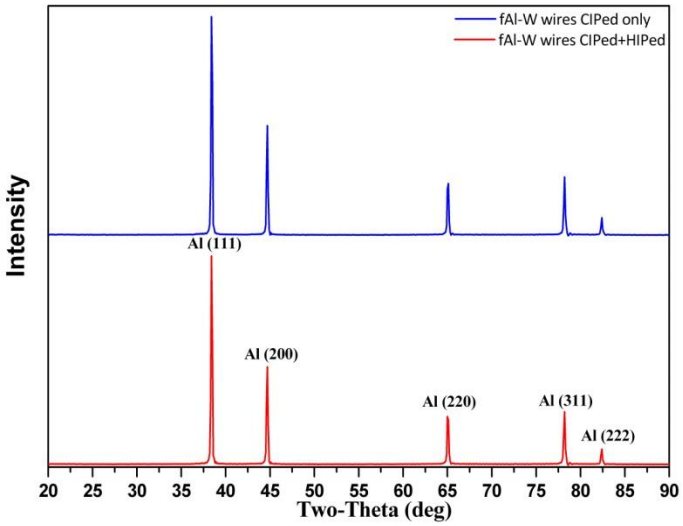

(b)

Figure 4.36 The XRD results of recovered fragments from (a) coarse Al-W wires, CIPed only and CIPed+HIPed; and (b) fine Al-W wires, CIPed only and CIPed+HIPed. They indicated that no intermetallic reaction occurred during tests.

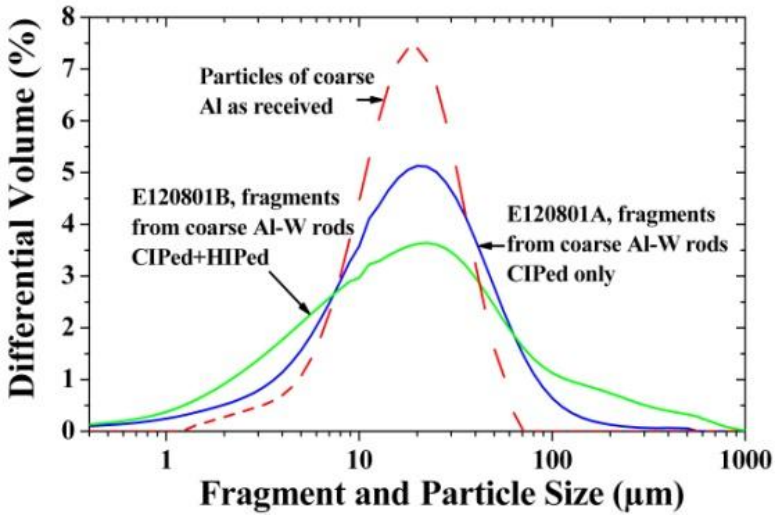

(a)

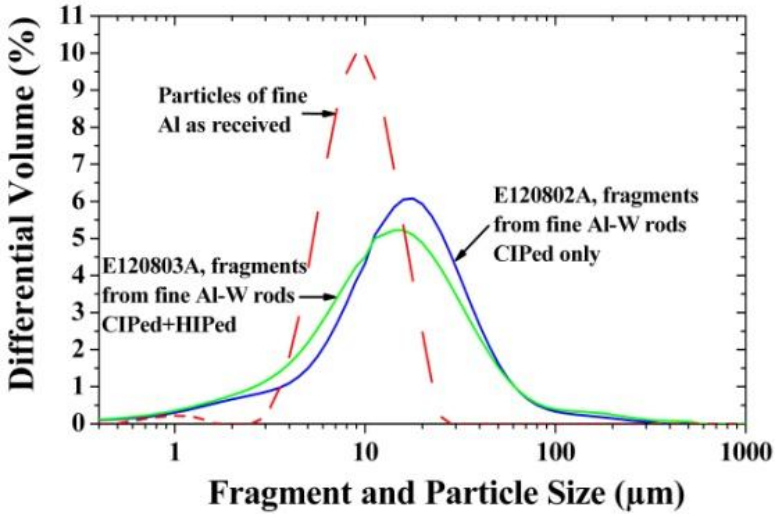

(b)

Figure 4.37 The fragment size distribution of the recovered fragments from samples with W rods and (a) coarse (b) fine Al powder. The as-received coarse and fine Al powder were also analyzed and presented.

Scanning Electron Microscopy (SEM) was utilized to examine the mesostructure of Al-W granular/porous composite rings before the dynamic test and the fragments after the test. Figure 4.38(a) demonstrates that particles in the fine Al/coarse W powder sample after the CIPing process mostly retained their as-received shapes (slightly deformed spheres for Al and polyhedrons for W). Figure 4.38(b)

shows a large recovered fragment polished and mounted in epoxy. Fragments of this size consisted of agglomerated Al and W particles. In the areas away from W particles, Al particles mainly maintained their equiaxed shape. Also observed in some places was the elongation of the low strength Al particles between high strength neighbouring W particles. This suggests that the Al particles underwent plastic deformation during the dynamic loading by either the extrusion of Al between the W particles, or the squeezing of the Al by the W particles.

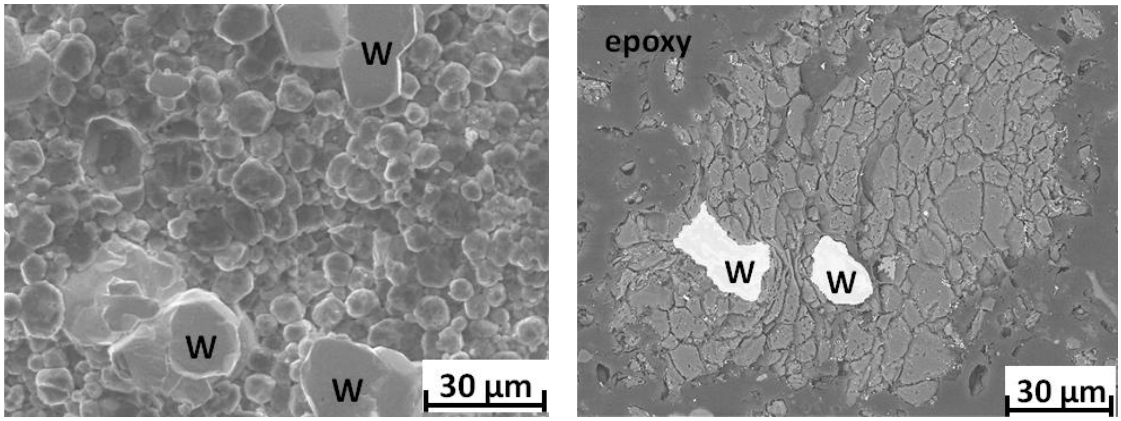

(a) (b)

Figure 4.38 SEM images of the CIPed only fine Al/coarse W powder sample: (a) before the test, and (b) one of the recovered fragments after the dynamic testing of the samples.

A similar phenomenon of localized plastic flow of Al particles was observed in samples with W rods as shown in Figure 4.39, 4.40, 4.41 and 4.42 (coarse Al-W rods CIPed only, coarse Al-W rods CIPed+HIPed, fine Al-W rods CIPed only, and fine Al-W rods CIPed+HIPed, respectively.). It should be emphasized that in the samples with Al powders and the W rods, the Al particles did undergo small alterations to their shape after CIPing and HIPing (subplots (a) in Figure 4.39, 4.40, 4.41 and 4.42), but were heavily dynamically deformed locally during the tests as shown in subplots (b) in Figure 4.39, 4.40, 4.41 and 4.42. The fragments presented in these figures (subplots (b)

in Figure 4.39, 4.40, 4.41 and 4.42) are taken from the area adjacent to the W rod, though this rod is not shown on the pictures. The extrusion of the Al matrix between W particles or rods may assist in the creation of fresh surfaces on the Al particles hence improving their oxidation and subsequent combustion efficiency. Recovered fragments from samples with different Al particles sizes and/or bonding conditions in Al matrix were very similar. This indicates the fragments pattern is not sensitive to the Al particle sizes or their bonding.

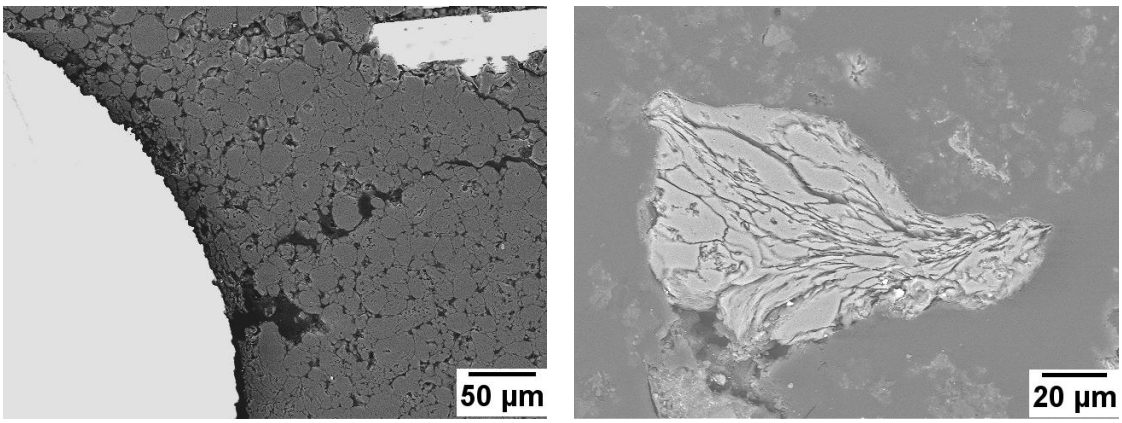

(a) (b)

Figure 4.39 SEM images of the CIPed only coarse Al-W rods sample: (a) before the test, and (b) one of the recovered fragments after the dynamic testing of the samples.

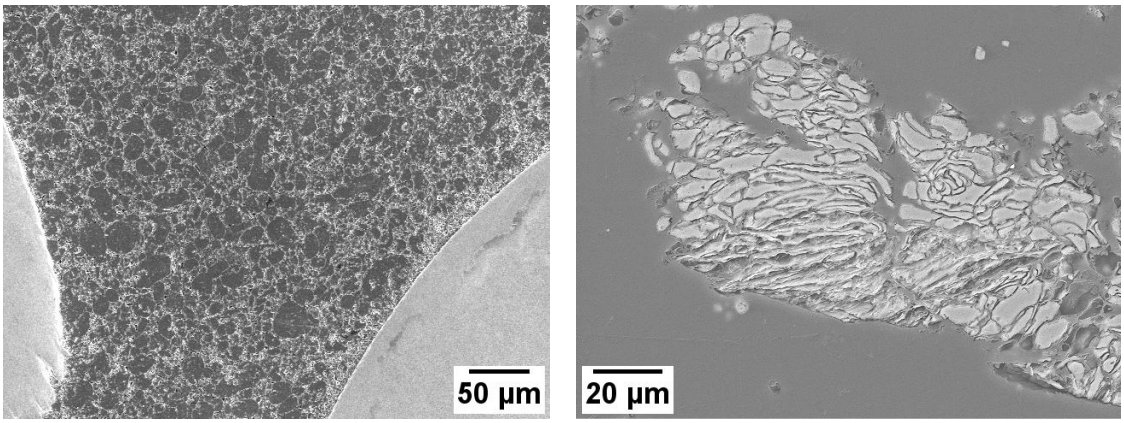

(a) (b)

Figure 4.40 SEM images of the CIPed+HIPed coarse Al-W rods sample: (a) before the test, and (b) one of the recovered fragments after the dynamic testing of the samples.

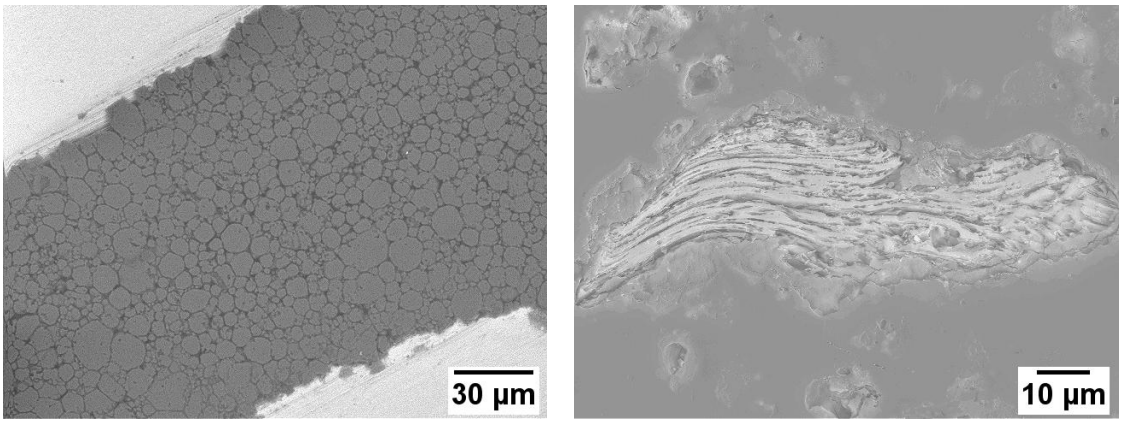

(a) (b)

Figure 4.41 SEM images of the CIPed only fine Al-W rods sample: (a) before the test, and (b) one of the recovered fragments after the dynamic testing of the samples.

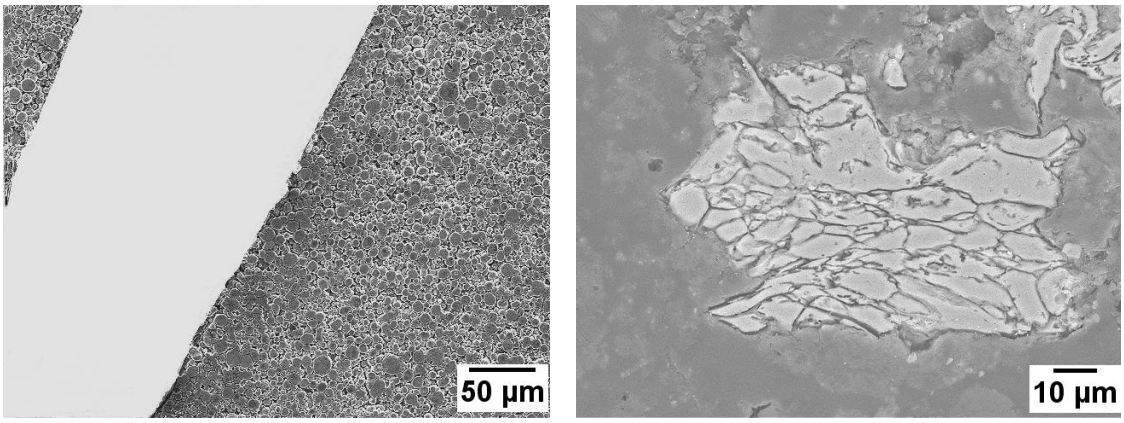

(a) (b)

Figure 4.42 SEM images of the CIPed+HIPed fine Al-W rods sample: (a) before the test, and (b) one of the recovered fragments after the dynamic testing of the samples.

Explosively driven fragmentation experiments were conducted with Al-W porous/granular composite rings with the goal of examining the mechanisms of fragmentation, characteristic fragment sizes and variations of these with respect to the mesostructure (coarse Al vs. fine Al particles, W powder vs. W rods, and bonded vs. unbounded Al particles). The porous/granular samples were mostly pulverized into fragments sizes below 100 micron (above 90%) for all tested mesostructures. A

comparison of initial sizes of particles in the powder and post experiment fragment size distributions indicates that some Al particles may have been fractured during the dynamic loading.

Some of the low strength Al particles were deformed between the rigid W particles, but mainly maintained their equiaxed shape in the areas away from W particles. Al particles were heavily deformed in samples with W rods regardless of the Al particle size and bonding between Al particles. The similar behavior in PDV records for the samples with W rods suggests that the global response is insensitive to the mesoscale properties of the Al. In all of the dynamic experiments, there was no observable intermetallic reaction between Al and W in the recovered fragments.

Numerical simulations were also performed to examine the mechanisms of fragmentation during explosively driven dynamic loading and details about the simulation can be found in [5]. Qualitative similarities between the simulations and experiments were observed. The simulations revealed that the creation and development of numerous sheared zones in granular Al matrix may allow fracture of initial Al particles and the generation of micron-sized Al fragments inside them. The spacing between these sheared zones is much larger than the size of the Al and W particles suggesting that material between them is shielded from mesoscale pulverization resulting in the generation of the large scale fragments of agglomerated Al and W particles. Comparison of fragmentation pattern of Al-W granular composite with fracture of SS304 sample demonstrates that mesostructural features of granular composite dramatically change fragmentation pattern in comparison with solid

material with similar density under identical conditions of explosive loading/strain and strain rates.

4.2.6 Summary

Quasistatic and dynamic experiments with W fiber-reinforced Al composites revealed qualitatively different behavior with respect to shear localization depending on the bonding between Al particles. It was shown that in CIPed only (unbonded Al prticles) samples the Al and W particles rearranged themselves through *in situ* densification during the dynamic deformation, thus creating a strain hardening mechanism, which effectively blocked shear localization. On the other hand, the bonding between Al particles in CIPed+HIPed samples inhibited strain hardening and facilitated shear localization and subsequent growth of the meso/macro shear bands/cracks. Solid Al-W-mesh composites were prepared and dynamically tested (loading in axial direction). The W mesh-reinforced samples showed highest dynamic compressive strength among the investigated Al-W composites. Bringing the Al matrix back to T6 condition can increase the strength by 19%.

Explosively driven expanding ring experiments were conducted with Al-W granular composite rings with different morphologies (W polyhedral particles or W rods with high aspect ratio and bonded/unbonded Al spherical particles with different sizes). In comparison to homogeneous samples with a similar density, these granular/porous composites generated fragments with a significantly smaller characteristic size (less than 100 micron for above 90% of recovered fragments). SEM micrographs revealed that in fragments, Al particles were heavily deformed near W

particles/rods regardless of the Al particle size and bonding between Al particles. The similar behavior in PDV records for the samples with W rods suggests that the global response is insensitive to the mesoscale properties of the Al. There was no observable intermetallic reaction between Al and W in the recovered fragments.

4.3 Concentric Al-Ni Laminates

4.3.1 Sample Preparation

Concentric Ni-Al laminate samples with different thickness were constructed from alternating layers of Ni and Al foils. The processing techniques and mesostructures were varied. The samples have been designated as Sample 1, 2, 3A, and 3B, where samples with the same number have the same nominal layer thicknesses.

Samples 1 were assembled from alternating foils of pure Al (McMaster-Carr Vickers microhardness HV = 251±4 MPa, purity at least 98%, initial thickness 38.1 μm) and Ni (Alfa Aesar, HV = 898±9 MPa, purity 99%, initial thickness 25.4 μm) using a layer-by-layer procedure. Prior to placement, each foil was cut to a length equal to the expected length of circumference of its corresponding position in the final assembly and cleaned with acetone. Each layer was loosely rolled and inserted one at a time into a thin copper tube (wall thickness 0.5 mm) with an inner radius equal to the desired outer radius of laminate sample for the TWC test. Each layer was unrolled by inflating the balloon, inserted into the center of the cavity, causing this layer to fit snugly against the previously placed layer. A total of 24 bilayers were used to construct Sample 1. The composite Sample 1 was then encapsulated in a rubber jacket

and processed using Cold Isostatic Pressing (CIPing) by applying pressure (345 MPa) on the interior surface of the laminate to increase stacking density and preventing the sample from buckling during preparation. After CIPing, the Al and Ni foils were densely packed, but the layers were not bonded. The overall density of the sample was (4.85 g/cc), corresponding to a porosity of about 6% (Figure 4.43(a)).

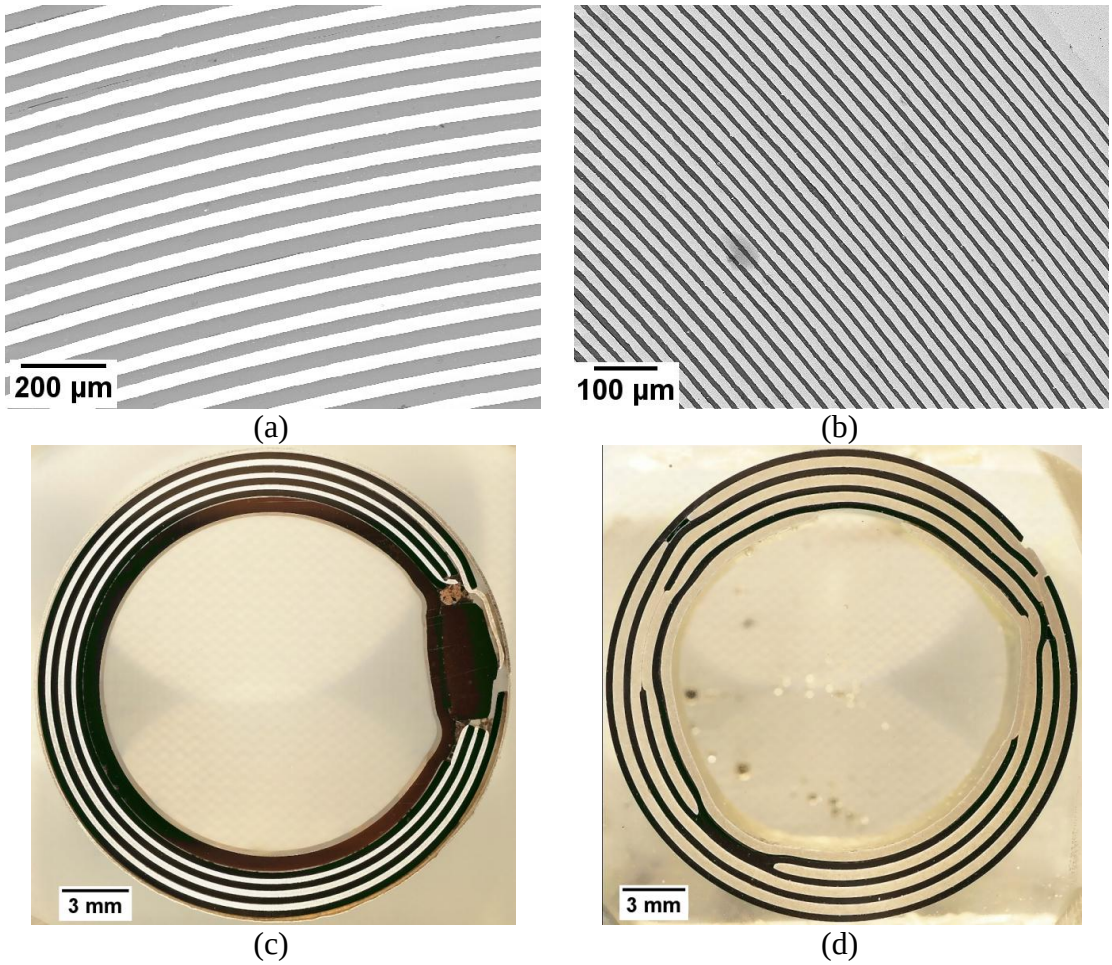

(a) (b)

(c) (d)

Figure 4.43 Al-Ni laminate cylinder samples with different mesostructures after pressure-assisted processing (CIPing) prior to dynamic testing. (a) Al-Ni laminate with thicknesses of layers Al (38.1 µm) and Ni (25.4 µm), corresponding to Samples 1; (b) Al-Ni Sample 2 with thicknesses of layers Al (11 µm) and Ni (7.5 µm); (c) Al-Ni Sample 3A with thicknesses of layers Al (370 µm) and Ni (250 µm). This sample has a copper insert to fill a single gap in the Ni and Al foils arrangement; (d) Al-Ni Sample 3B with thicknesses of layers Al (370 µm) and Ni (250 µm) with axially asymmetric arrangement of layers where parts of Ni (or Al) foils are replaced by Al (or Ni) foils.

Sample 2 was constructed from alternating foils of elemental Ni (American Elements, purity 99%, HV = 852±11 MPa) and Al foils (McMaster-Carr, purity 99%, HV = 213±9 MPa) with very thin foil thicknesses of 7.5 μm and 11.0 μm, respectively. Due to the reduced layer size, the sample was constructed by tightly winding bilayer stacks of foil strips around a copper tube with an outer diameter of 12.0 mm and wall thickness of 0.5 mm. This process was continued until the desired thickness of the sample was achieved (55 bilayers, 2.5 mm total thickness). The sample was then encapsulated in a rubber jacket and two cycles of CIPing (CIPing pressures in each cycle was 345 MPa with pressure applied on the interior surface of the laminates) were performed to increase the stacking density of the laminates. After a second CIPing cycle, the overall density of the sample was 5.09 g/cc corresponding to a porosity of 1.4% (Figure 4.43(b)).

Sample 3A and Sample 3B consisted of 4 Ni-Al bilayers with increased nominal layer thickness of 370.0 μm for Al layers (McMaster-Carr, purity 99%, HV = 306±10 MPa) and 250.0 μm for the Ni layers (Alfa Aesar, purity 99%, HV = 1138±17 MPa). These layers exhibited an increased flexural strength in comparison to the previous samples and the balloon method applied for thinner foils could not be used. Instead, four thin Al 6061T6 tubes with the same wall thickness (370.0 μm) and different diameters (the diameters were smaller for tubes intended for the inner layer of the sample) were machined and annealed to the hardness (HV = 323±13 MPa) similar to the hardness of Al foils. Four Ni foils were cut to suitable length and each foil was wrapped around the corresponding Al tube individually. In Sample 3A, the four Ni/Al bilayers were assembled concentrically and rotated such that all of the layer

edges were aligned. A copper wedge was machined to insert into the gap that was formed during the first CIPing process and the assembly was CIPed from the inside again ((Figure 4.43(c)). After two CIPing cycles, the overall density of the sample was 5.07 g/cc corresponding to a porosity of 1.9%.

For Sample 3B, randomly distributed defects in each layer through the sample thickness were added to the mesostructure by rotating the layers prior to construction (Figure 4.43(d)). After CIPing from the inside, the overall density of the sample was 4.65 g/cc corresponding to a porosity of 10%.

4.3.2 TWC Methods

The sample was enclosed in a copper assembly (see Figure 4.44) for the TWC test. The copper stopper tube had an inner diameter of 10 mm and an outer diameter of 12 mm. The copper driver tube had an inner diameter of 17.1 mm and an outer diameter of 30 mm. The explosive driver for the TWC test was a gelled nitromethane (96% nitromethane, 4% PMMA) diluted 5% by mass with glass microballoons that allowed for the fine tuning of the dynamic loading (explosive density=0.82 g/cc, detonation velocity = 4.8 mm/μs). The diameter of the explosive charge was equal to 58 mm and thickness of PVC container was 7.4 mm.

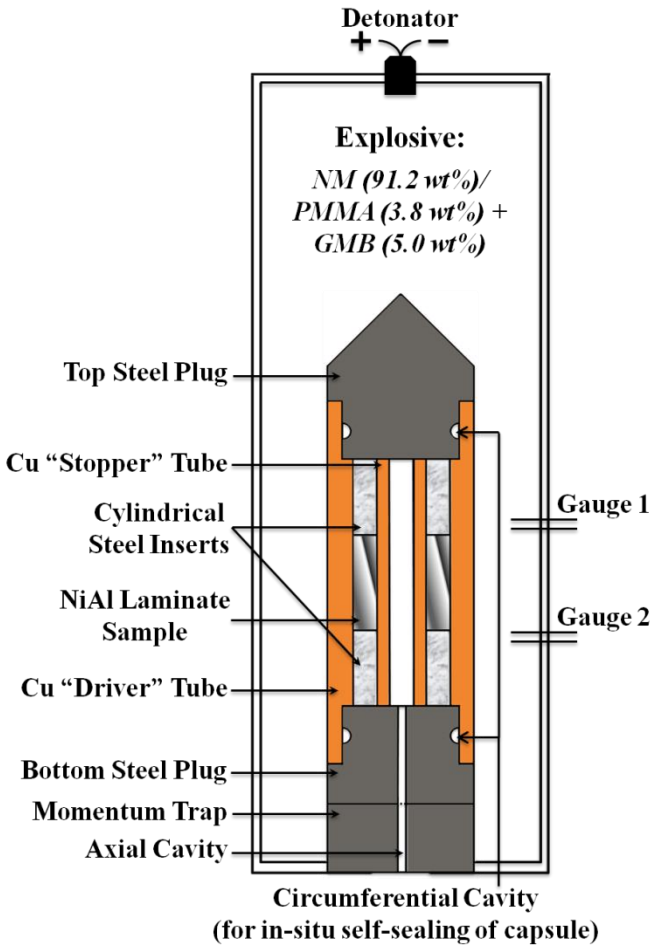

Figure 4.44 Experimental setup for Thick Walled Cylinder Method.

After the TWC test, the samples were cut perpendicular to their axes using electric discharge machining (EDM) to ensure that the Ni-Al laminates would not react during the machining process. This examination of the global response was performed on multiple samples deformed in similar conditions to demonstrate the repeatability and consistency of the experimental results.

Global views of the collapsed Samples 1, 2, 3A, and 3B are presented in Figure 4.45. In all of the experiments, the interface between the sample and the inner copper stopper tube and the outer driver tube retained its cylindrical shape due to the large

thickness of the copper driver tube (Figure 4.45(a) to (d)). All samples showed a complete collapse of the copper stopper tube. Axial jetting originated from its inner surface at the last stages of collapse removed only very small mass of copper (verified by the value of its final radius based on mass conservation. The global effective strains were calculated using Equation 3.10. The global effective strains at the inner surface of the sample, ε_{eff}, for all experiments presented in this paper were 0.68±0.04, demonstrating good repeatability of the tests.

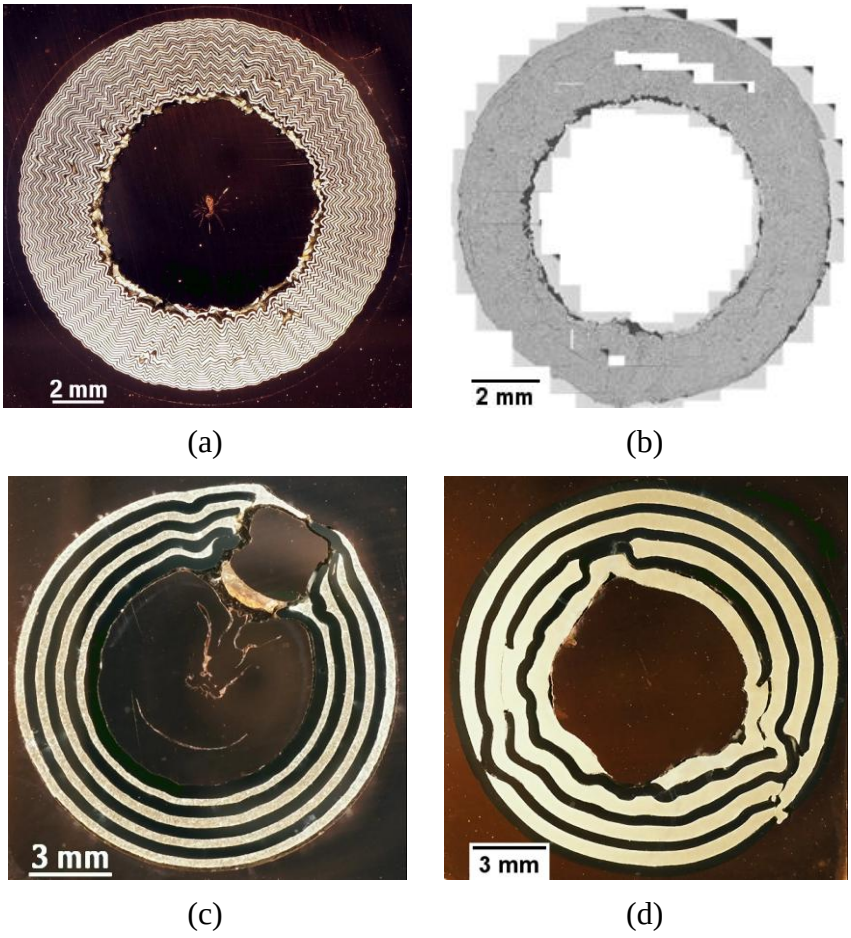

(a) (b)

(c) (d)

Figure 4.45 Global view of collapsed Ni-Al laminate cylindrical samples (a) Sample 1, (b) Sample 2 assembled from SEM images (due to the composite nature of these images, they exhibit artificially sheared layers in some "stitching" places), (c) Sample 3A and (d) Sample 3B. The nearly cylindrical shape of the outer interface was maintained ensuring the global symmetry of plane strain deformation despite large variations in the mesostructures of the various samples.

Examination of the Sample 1 after the TWC test showed that the dominant mechanism of plastic strain accommodation was the cooperative buckling of Ni and Al layers (Figure 4.45(a)). No shear bands were observed in the sample. Based on the pattern of radially-aligned peaks and troughs of the buckles (apices), it may be concluded that the cooperative buckling of individual layers originated in the inner layers (due to higher strains) and propagated outward as the cylinder collapses. Thus the instability mode of the outmost layers is dictated by the buckling mode of the inner layer. This mechanism of plastic strain accommodation in the laminate material is qualitatively different than found in previously investigated homogeneous materials (solid and granular, inert and reactive) subjected to similar loading conditions in the same geometry [6-18].

Numerous areas of reaction were observed in the collapsed sample in areas adjacent to the apices (Figure 4.46). Based on Energy Dispersive X-ray Spectroscopy (EDX) analysis, two types of reaction products were observed, Ni-rich and Al-rich, which were similar to the reaction products observed in References [20-22]. The numerical calculations also demonstrated that the areas near the apices, approximately the size of the layer thickness, were the areas of maximum local strains and temperatures. The typical level of effective plastic strains observed in these areas were about 1.5 corresponding to peak temperatures 550 ℃ for Al and 600 ℃ for Ni. The start of reaction in Al-Ni laminates [22, 23] was observed under static conditions at temperatures 200 - 600 ℃. This indicates that local plastic strains inside apex areas are sufficient to explain observed localized reaction. The ignition temperature for nanolaminates is in the range of 450-900 ℃K [20, 23] indicating that ignition in these

materials can be attained in dynamic conditions similar to our experiment. In addition to the local plastic deformation increase of interface temperatures also can be caused by friction. The role of friction is supported by the smaller localized spots of reaction observed at Al-Ni interfaces away from the apices.

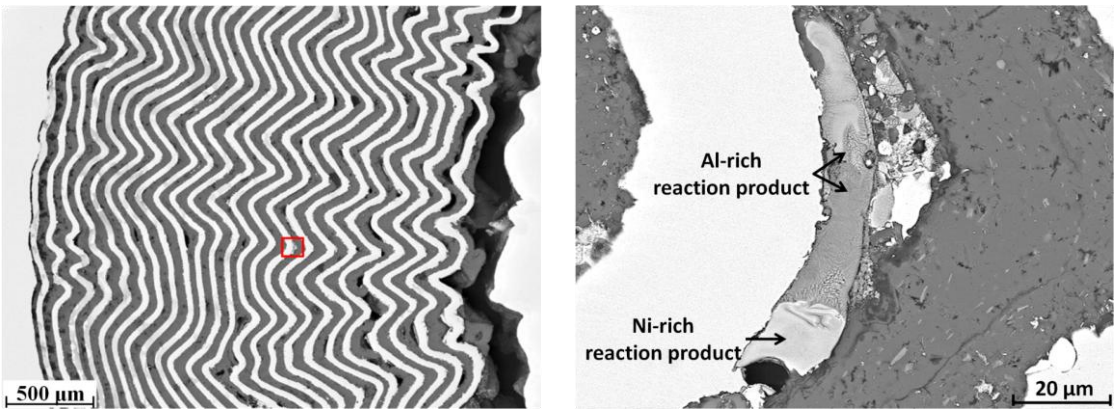

(a) (b)

Figure 4.46 (a) the SEM image of the similar sample after the TWC testing where Ni is white and Al is gray. The red square indicates the area with the local reaction shown at larger magnification in (b). (b) Intermetallic reactions at the Ni and Al interface were observed at the outer apex regions of the buckling Ni foil. EDX results showed two types of reaction products: Ni-rich and Al-rich.

Numerical simulations were used to elucidate the mechanism of the plastic strain accommodation during the TWC experiments. They were conducted under plane strain conditions using a finite-element software LS-DYNA. Details regarding the simulation can be found in [5, 19]. For Sample 1, the geometry of the cylinder at the initial stage of instability demonstrating the initiation of cooperative buckling originating in the inner layers is presented in Figure 4.47(a). The collapsed laminate sample with the fully developed instability is presented in 4.47(b), and the plastic strain distribution in the composite is shown in Figure 4.47(c).

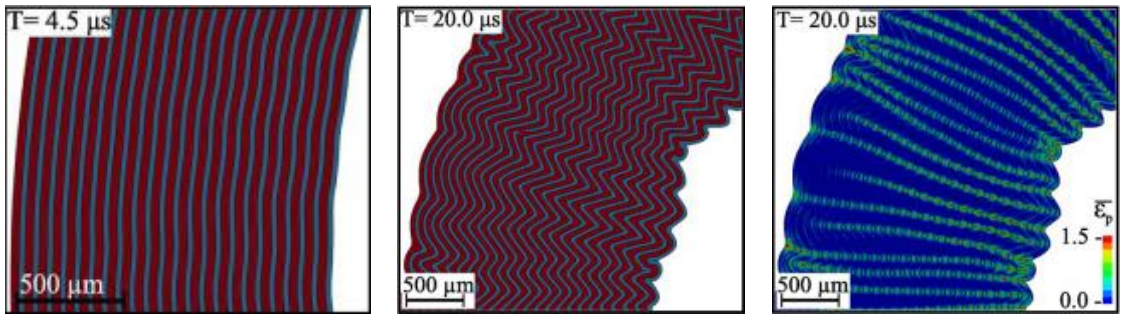

(a) (b) (c)

Figure 4.47 (a) The mesostructure of the simulated partially collapsed concentric Al-Ni sample where Ni is blue and Al is red. It demonstrates the development of the instability in the inner layers; (b) the mesostructure of the laminated collapsed TWC sample (Al (red) and Ni (blue)) generated in the numerical simulations; (c) the effective plastic strain of the same view shown in (b) [19].

It is clear from comparing these results with the experiment (Figure 4.46(b)) that the simulation shows good agreement with the experiment. The number of apices in a single layer in the experiment was 148 while this number in the simulation was 164, a 10.8% difference. Defining a characteristic amplitude of waviness, $\bar{A}_w$, as the average of the differences in the radius of all neighboring apices in the same layer yields an $\bar{A}_w$ of 155.7 μm for 5th Ni layer (about 6 times Ni layer thickness) in the experimental sample while the simulation predicts an $\bar{A}_w$ of 144.2 μm for the 5th Ni layer in the simulation. Simulations with different strain rates of collapse were conducted by altering the explosive properties demonstrated that increasing strain rate results in an increasing number of apices. The difference in number of apices and $\bar{A}_w$ in simulations and experiment is probably due to the difference in the high strain, high strain rate material behavior and due to the role of friction between layers in experiments.

For median thickness samples (Sample 1), the simulations and experiments both clearly show that the cooperative buckling of the layers was the dominant mechanism of plastic strain accommodation in the Al-Ni laminates during collapse. The simulations demonstrate that as the cylinder initially collapses, the individual layers experience compression in the hoop direction with the interior layers experiencing a larger hoop strain than the exterior layers. At a critical strain, the spontaneous buckling of the inner layers occurs and quasi-sinusoidal wave-shaped distortions develop. This initial buckling in the inner layers triggers the cascading geometric instability of neighboring layers extending all the way to the outermost layers. The amplitude of waviness increases to accommodate the change in circumference length with further collapse of the cylinder. The simulations show that this amplitude change is non-symmetric despite the initial symmetric geometry and that additional buckling does not occur on later stages of collapse. This suggests that the increase in amplitude of the initially buckled shape is the favorable mode of plastic accommodation. At the same time, we observed some secondary buckling (Figure 4.46(a) and 4.47(b)), demonstrating that the instability in the outer foil layers may not be completely controlled by buckling in the innermost layer where local conditions may also influence the instability.

SEM micrographs of a representative section of Sample 2 (bilayer thickness 18.5 μm) mesostructure at different magnifications is presented in Figure 4.48(a). The main mechanism of plastic strain accommodation observed in Sample 2 was the development of localized “kink bands.” These kink bands are similar in nature to the shear bands observed in homogeneous and granular materials in that the deformation

is mainly localized to these zones and the material between these sections are dubbed "dead zones" where little to no deformation is observed. However, unlike homogeneous materials, the layers in many of the dead zones showed the development of low amplitude high frequency buckling (see Figure 4.48(a)). Additionally, many of the kink bands were not oriented at a 45°angle to the radius characteristic of shear bands in other materials. Most of the kink bands near the inner surface are radially oriented and begin to depart from the radial orientation 3-5 bilayers into the composite. Once these kink bands depart from the radial orientation they begin to move towards the 45 degree orientation.

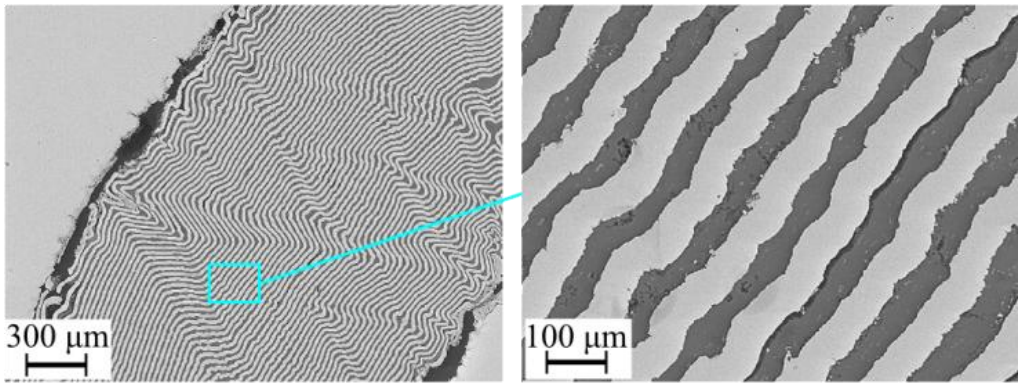

(a)

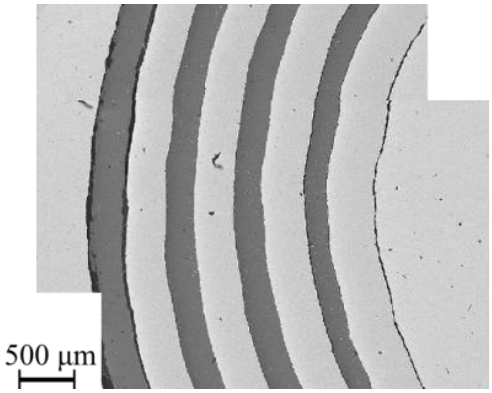

(b)

Figure 4.48 The influence of the layer size on the mechanism of plastic strain accommodation. (a) The mesostructure of Sample 2 with bilayer thickness 18.5 μm at different magnifications. (b) The mesostructure in Sample 3A with bilayer thickness 620 μm.

Examination of the collapsed mesostructure from Sample 3 with much thicker layers (bilayer thickness 620 μm) (see Figure 4.48(b)) demonstrated that the main mechanism of plastic strain accommodation was the uniform plastic flow (radial strains in the layers based on the thicknesses of initial and deformed layers were for Al foil 0.30±0.04 and for Ni foil 0.28±0.04) in addition to the localized buckling of the layers near the large Cu inclusion (see Figure 4.45(c)). Some small amplitude buckling was observed on the innermost layers.

The layers in the region neighboring the Cu wedged inclusion showed significant localized buckling. This localized buckling is due to conditions similar to that observed in a Taylor bar impact experiment where, due to the radial collapse of the tube, compressive hoop strains causes the circumferential movement of the free ends of the Ni and Al layers toward the Cu wedge. As there exists a small initial gap between the layers and the wedge, these tip ends impact at velocities similar to those of the radial collapse. However, no observable influence of this behavior was seen in material approximately 20°from the Cu wedge.

Results of the simulations with fully bonded interfaces between the Al and Ni layers (Figure 4.49) demonstrate that the materials with the thin layers (Figure 4.49(a) and (b)) develop localized kink bands and high frequency buckling in areas between these bands. This behavior is qualitatively similar to the observed in the experiments with double CIPed samples presented in Figure 4.48(a). The laminates with thick layers (Figure 4.49(c) and (d)) show mostly uniform layer deformation with some signs of low amplitude buckling of the first inner layers (compare with Figure 4.48(b)).

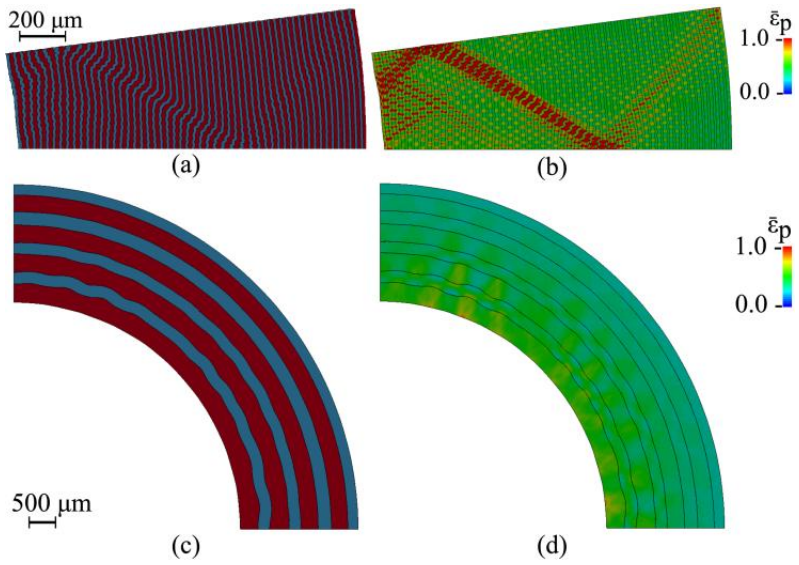

Figure 4.49 Influence of the layer size on the mechanism of plastic strain accommodation in a fully bonded laminate in numerical simulations with the corresponding layer thicknesses similar to Figure 4.48. The deformed geometries are shown in (a) and (c) and the corresponding fringes of plastic strain in (b) and (d).

For Sample 3B, in both experiments and simulations (Figure 4.50), the region of influence of an initial defect was local, i.e., it did not extend beyond the location of the initial defect. In the area where multiple defects are present (Figure 4.50(c)), they act cooperatively to influence the local region more dramatically, however, the size of the area of influence is not significantly increased. This suggests that samples with a mesostructure that is mainly concentric, with some local defects, will accommodate plastic strains similar to the pristine concentric sample.

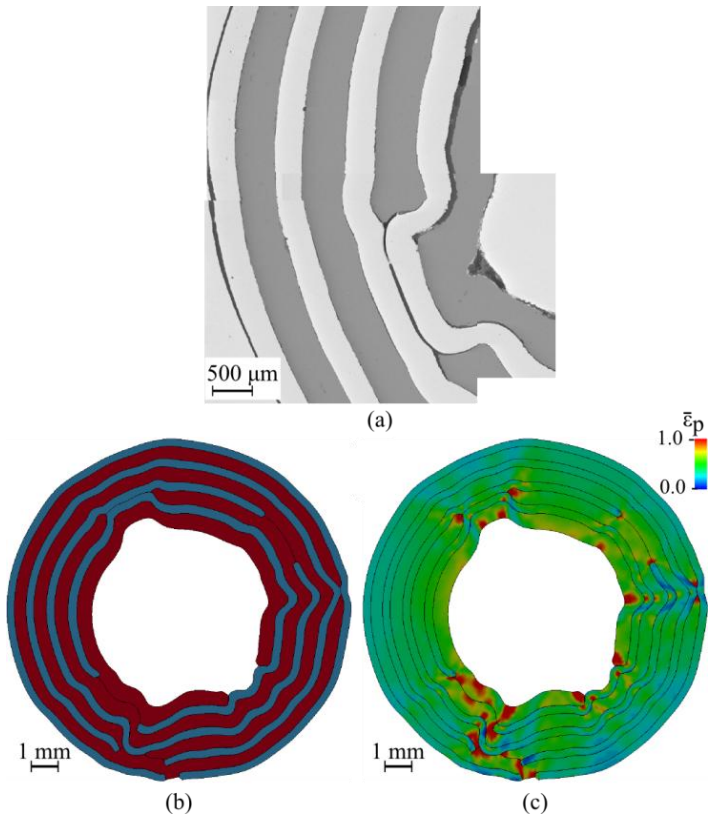

Figure 4.50 (a) The mesostructure of the Sample 3B in the region near one of the defects in the inner layer. The defect has influenced a deformation pattern only local region. Its size is similar to the size of the initial defect which is reflected in the deformed geometry (b) and in the corresponding fringes of plastic strains (c) in the simulated collapse of Sample 3B.

4.3.3 Summary

Mechanisms of plastic strain accommodation were investigated experimentally using the explosively driven TWC test in reactive laminate Ni-Al in a concentric geometry. A dramatic difference in mechanism of buckling at the same global strain and strain rates was observed for samples with different thickness of layers. Numerical modeling was used to elucidate the mechanisms of plastic strain accommodation in the dynamic collapse of Ni-Al laminate materials and it showed good agreements with experimental results. Three main mechanism of plastic strain accommodation

depending on bilayers sizes were observed in the concentric Al-Ni laminates: (1) cooperative buckling for Sample 1 (bilayers thickness = 63.5μm); (2) kink bands with low amplitude buckling in-between for Sample 2 (bilayers thickness = 18.5μm); and (3) uniform plastic flow for Sample 3A (bilayers thickness = 620.0μm). Sample 3B showed randomly distributed defects only had a relatively minor local influence on the order of the layer thickness.

4.4 Corrugated Al-Ni Laminates

4.4.1 Sample Preparation

Alternating layers of Al (30 micron nominal thickness) and Ni (20 micron nominal thickness) were stacked, rolled into a cylinder and then placed into a tubular steel jacket. This jacketed assembly was then swaged using mating tapered dies resulting in cylindrical shaped rods with a corrugated mesostructure. The two rods that underwent 6 and 7 swaging cycles were used to prepare samples tested in this paper, SW-6 and SW-7, respectively. Additional details of the swaging process can be found in [24].

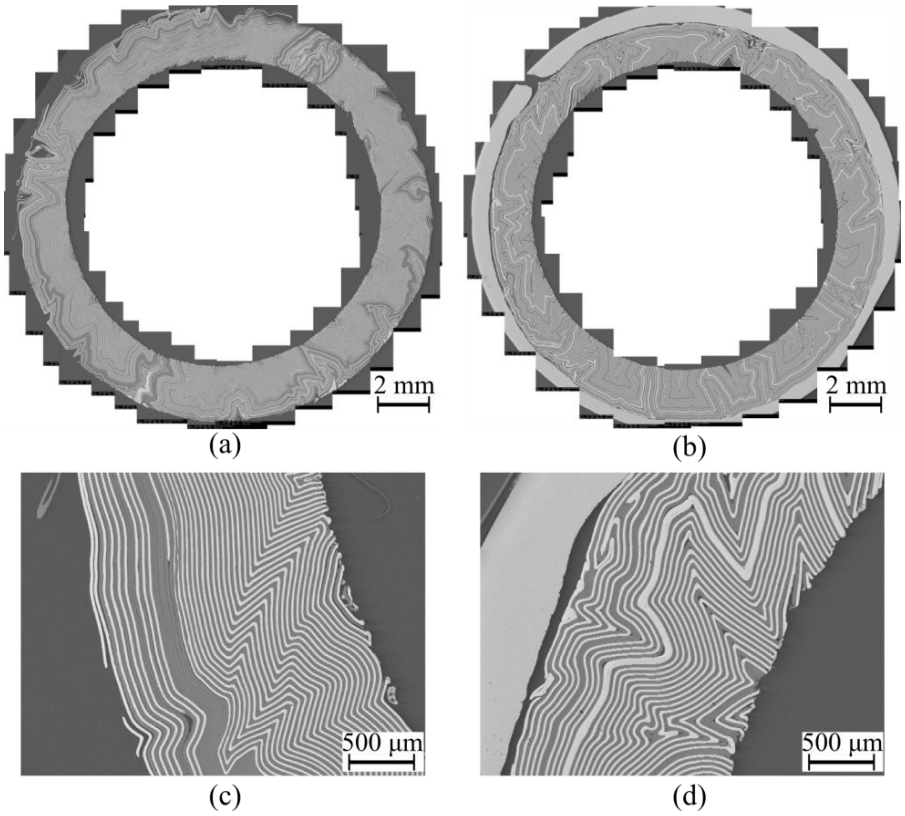

Figure 4.51 Cross-sectional micrographs of the swaged Ni-Al laminate tubes (a) SW-6A and (b) SW-7A before the TWC test. The higher magnification images, (c) and (d), correspond to SW-6A and SW-7A, respectively. The Ni and Al layers had a nominal thickness of 20 and 30 microns, respectively, in each sample and appear as white and dark grey, respectively. Samples SW-7A, B, and C have a thin steel jacket on the exterior of the sample.

Each of the swaged rods (SW-6 and SW-7) was cut into three 30 mm long segments and labeled A, B, and C. Electrical Discharge Machining (EDM) was used to remove the central core of each rod segment to create the hollow cylinders used as samples in the dynamic tests and to ensure that no reaction occurred during the machining of the samples. The initial, corrugated, as-processed Al-Ni samples are presented in Figure 4.51 (a) and (b) and high magnification scanning electron micrographs for these samples are presented in Figure 4.51 (c) and (d). Due to the processing technique used to create the samples, their mesostructures are highly

heterogeneous on two different spatial scales – the size of the layers and the size of the corrugation. In most places in the samples the thicknesses of Al and Ni layers are similar and can be characterized by a nominal thickness. Variations in swaging and machining processes resulted in slightly different inner diameters (I.D.) and outer diameters (O.D.) of the samples (see Table 4.5).

Table 4.5 Dimensions of the TWC samples before the TWC experiments.

	SW-6A	SW-6B	SW-6C	SW-7A	SW-7B	SW-7C
Sample I.D. (mm)	12.08	12.21	12.25	12.20	12.20	12.23
Sample O.D. (mm)	16.21	17.41	17.38	17.06	16.74	16.78

Sample SW-7 retained a thin steel jacket (400-700 μm thickness), which was left on for convenience of sample handling, and did not significantly affect the behavior of collapse during the dynamic deformation because the copper driver tube dominates the dynamic collapse, irrespective of the sample's mesostructure.

4.4.2 TWC Methods

The hollow Ni-Al laminate cylinder samples were placed in the TWC assembly shown in Figure 4.52 (a). The inner diameter and outer diameter of the copper stopper tube in all experiments was 10.0 mm and 12.0 mm, respectively. The dimensions of the copper stopper tube allowed for the precise control of the dynamic global strain imparted to the sample due to the complete collapse of the TWC assembly (see Figure 4.52 (b)). The outer diameter of the copper driver tube was 31.8 mm for all experiments; the inner diameter of the copper driver tube (varied from 16.8 to 17.5 mm) was customized for each sample. The top and bottom steel plugs in the

TWC assembly had grooves (depth and radius equal to 5 mm). They served for *in situ* sealing of the TWC assembly (see Figure 4.52 (c)) during the test to ensure the complete recovery of the test specimen and to prevent the penetration of the detonation products.

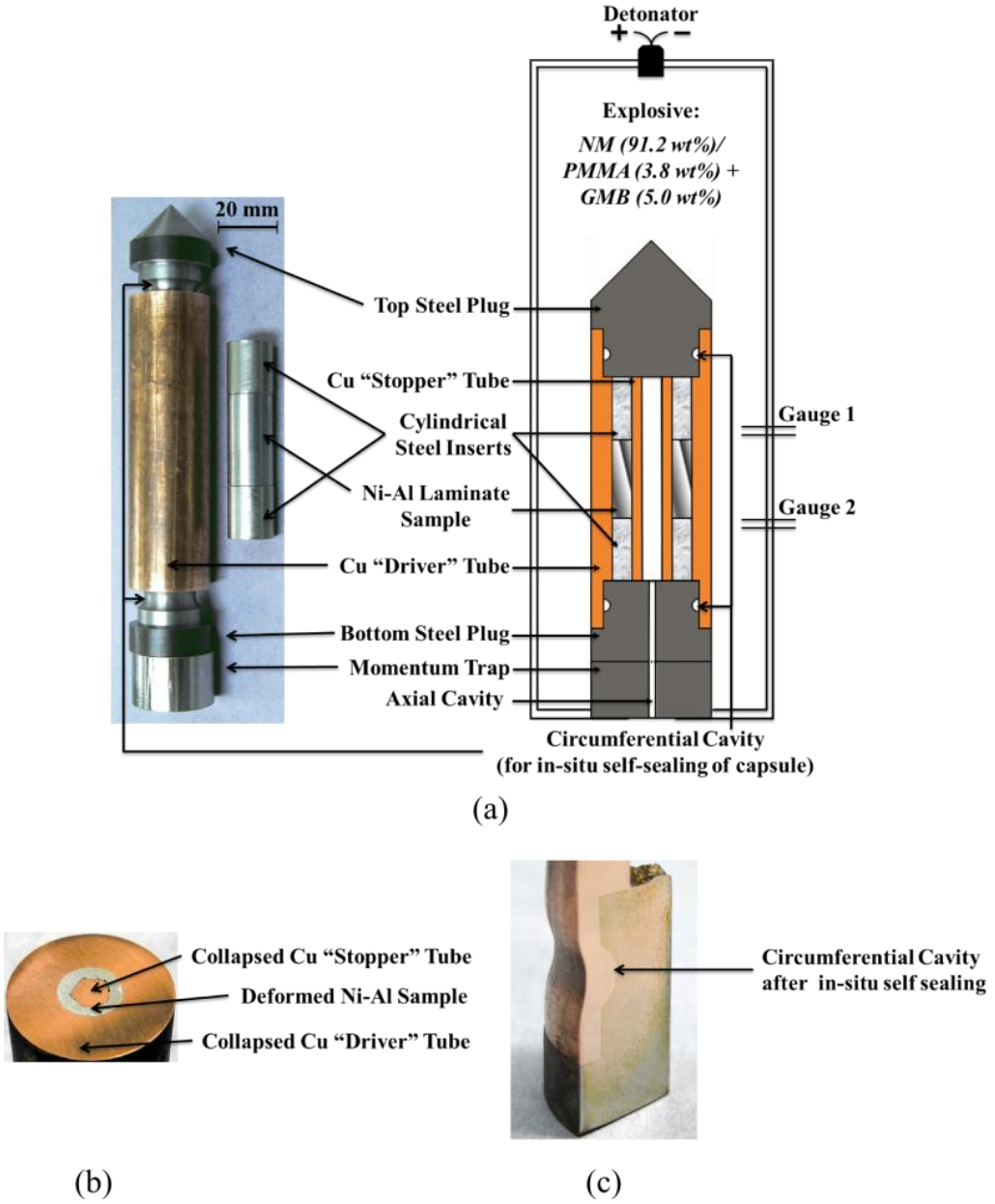

Figure 4.52 (a) The experimental setup for Thick Walled Cylinder Method [19], (b) a detailed view of the collapsed sample, and (c) the explosively sealed cavity.

The TWC assembly was placed in a PVC container with an inner diameter of 58.0 mm and a wall thickness of 7.4 mm. The container was filled with a gelled Nitromethane (96% Nitromethane, 4% PMMA) explosive to drive the collapse of the TWC assembly. Glass microballoons (3M™ Glass Bubbles K1) were used to dilute the explosive 5% by mass, allowing the fine-tuning of the dynamic loading [19]. The detonation velocities in the experiments were measured to be 4.80 ± 0.05 km/s and exhibited good reproducibility.

The recovered self-sealed samples were along planes perpendicular to their axes after the TWC experiments with EDM to prevent any incidental reaction event from occurring during the post-TWC examination process. The dimensions of the samples and the effective strains on the interface with the copper stopper tube are presented in the Table 4.6.

Table 4.6 Dimensions of the TWC samples and effective strains after the TWC experiments.

Sample	SW-6A	SW-6B	SW-6C	SW-7A	SW-7B	SW-7C
Mean sample I.D. (mm)	6.58	7.12	6.82	6.66	6.86	6.62
Mean sample O.D. (mm)	13.02	14.54	14.32	14.28	13.22	13.40
Calculated diameter (mm) of fully collapsed Cu stopper tube based on mass conservation	6.63	6.63	6.63	6.63	6.63	6.63
Calculated effective strains (ε_{ef}) of the inner sample based on mass conservation of inner Cu stopper tube	0.69	0.70	0.71	0.70	0.70	0.71
Measured effective strain (ε_{ef}) of the outer surface of the sample	0.25	0.21	0.22	0.21	0.27	0.26

Microstructural analyses of the cross-sectional axial cuts were performed by using scanning electron microscopy (SEM). The composite images of the medial cuts from all of the tested samples are presented in Figure 4.53 It should be noted that there are variations of the mesostructure through the axial direction of the sample due to the swaging processing. As such, the composite images of the mesostructures for the collapsed samples SW-6A and SW-7A, presented in Figure 4.53, do not exactly correspond to the initial mesostructures presented in Figure 4.51, as they are cut from different axial locations. High magnification images of representative areas of the collapsed mesostructures are presented in Figure 4.53, illustrating that local trans-layer shear bands were common in all samples and generally are located in the interior regions of the sample. Additionally, this figure shows a unique mesostructual behavior - the extrusion of wedge-shaped regions on the inner surface of the cylinder towards the inner copper stopper tube. These wedge-shaped regions directly correspond to the initial corrugation in the mesostructure generated during the swaging process.

The final mean inner diameter of the Al-Ni samples are presented in Table 4.6. The maximum effective global strains at a material point in the sample were calculated using the initial radius of this point (r_0) and the radius after the collapse (r_f) with the Equation 3.10. Due to the highly irregular interior surface of the collapsed TWC samples, the corresponding value of r_f was calculated based on the conservation of mass of the copper stopper tube, assuming a perfect cylindrical geometry of collapse. The mass of a central copper rod with a height 7.8 mm is equal to 2.21 gram and the initial mass of the corresponding segment of copper stopper tube with the same height was 2.32 gram. This suggests that only 0.11 gram was removed from the inside

surface of the collapsed copper stopper tube due to axial jetting or due to axial plastic flow of the sample. This translates to a difference of 7.8×10^{-2} mm (2.4%) for the outside diameter of the collapsed copper stopper tube if we assume that this mass difference is due solely to the removal of central part of copper stopper tube by jetting. If we attribute this difference in mass to axial elongation due to plastic flow of the sample, the upper estimate of axial strain will be 0.047. The global effective strain in all of the samples on the inner surface was between 0.69 and 0.71 while on the outer surface, the strains were between 0.21 and 0.27. The corresponding final inner and outer calculated radii are shown in Figure 4.53 as blue lines imposed over the collapsed samples. The cylindrical geometry of the outside surface of the sample (deformed by a copper driver) was preserved during the collapse process, allowing us to model the heterogeneous deformation of the interior areas assuming a cylindrical exterior geometry, as in the other cases of collapsing cylinders with a complex inner cavity shape [26, 27].

By comparing the mesostructure before and after the TWC test, it is apparent that there are more radially aligned apexes and less locally coaxial areas in the post-experimental samples, suggesting that the mechanism of cooperative buckling, similar to that observed in the concentric mesostructure in [19], is active in regions where the layers are locally concentric. The generation of the apexes in the locally coaxial areas is likely influenced by the initial corrugation of the areas interior to these regions.

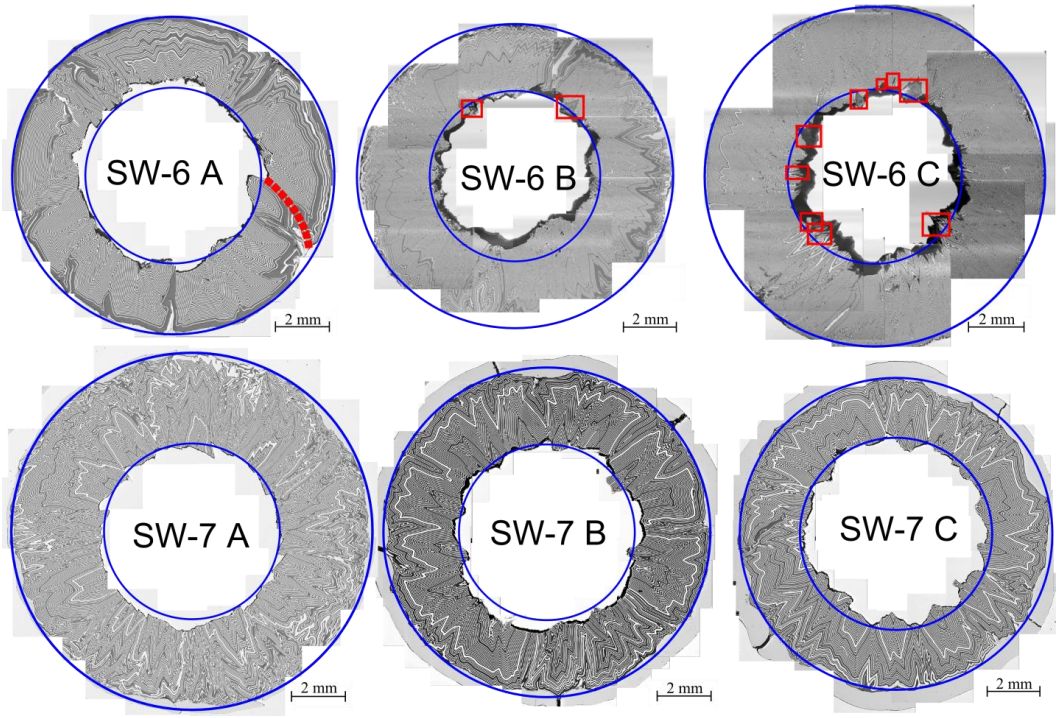

Figure 4.53 Axial slices of the collapsed samples showing axial symmetry of the outside surface of deformed samples, similar maximum strains (0.69-0.71), and similar features on the inner surface (wedge extrusion). The inner blue circles in each of the samples represent the calculated mean inner diameter of the sample based on the mass conservation of the inner copper stopper tube, assuming plane strain geometry of deformation for the copper driver and stopper tubes during the collapse. A global shear band is shown in SW-6A by a dashed line; areas of extruded and reacted wedges in SW-6B and SW-6C are shown by red squares.

The final mean inner diameter of the Al-Ni samples are presented in Table 4.6. The maximum effective global strains at a material point in the sample were calculated using the initial radius of this point (r_0) and the radius after the collapse (r_f) with the Equation 3.10. Due to the highly irregular interior surface of the collapsed TWC samples, the corresponding value of r_f was calculated based on the conservation of mass of the copper stopper tube, assuming a perfect cylindrical geometry of collapse. The mass of a central copper rod with a height 7.8 mm is equal to 2.21 gram and the initial mass of the corresponding segment of copper stopper tube with the same height was 2.32 gram. This suggests that only 0.11 gram was removed from the inside

surface of the collapsed copper stopper tube due to axial jetting or due to axial plastic flow of the sample. This translates to a difference of 7.8×10^{-2} mm (2.4%) for the outside diameter of the collapsed copper stopper tube if we assume that this mass difference is due solely to the removal of central part of copper stopper tube by jetting. If we attribute this difference in mass to axial elongation due to plastic flow of the sample, the upper estimate of axial strain will be 0.047. The global effective strain in all of the samples on the inner surface was between 0.69 and 0.71 while on the outer surface, the strains were between 0.21 and 0.27. The corresponding final inner and outer calculated radii are shown in Figure 4.53 as blue lines imposed over the collapsed samples. The cylindrical geometry of the outside surface of the sample (deformed by a copper driver) was preserved during the collapse process, allowing us to model the heterogeneous deformation of the interior areas assuming a cylindrical exterior geometry, as in the other cases of collapsing cylinders with a complex inner cavity shape [26, 27].

The local trans-layer shear bands (see Figure 4.54), observed in all samples, were limited to the inner areas of the sample and did not create a periodic pattern as in all previously investigated granular and solid materials [8-18, 25]. In general, the local trans-layer shear bands spanned ~3-10 layers in the areas where the Ni and Al layers were approximately radially aligned. This radial alignment obstructed the accommodation of large strain by other mechanisms. For example, the formation of shear localization in the soft Al layers or sliding along non-bonded Ni-Al interfaces, as well as the development of cooperative buckling [19], were less favorable than trans-layer shear localization. These trans-layer shear bands were oriented approximately 45°

from the radial direction corresponding to the maximum global stress. Within these shear band zones, the Ni and Al layers were elongated and fragmented as shown in Figure 4.54 (c). This elongation resulted in a decrease in the layer size in the shear band by nearly an order of magnitude (from approximately 12 microns to approximately 1.2 microns).

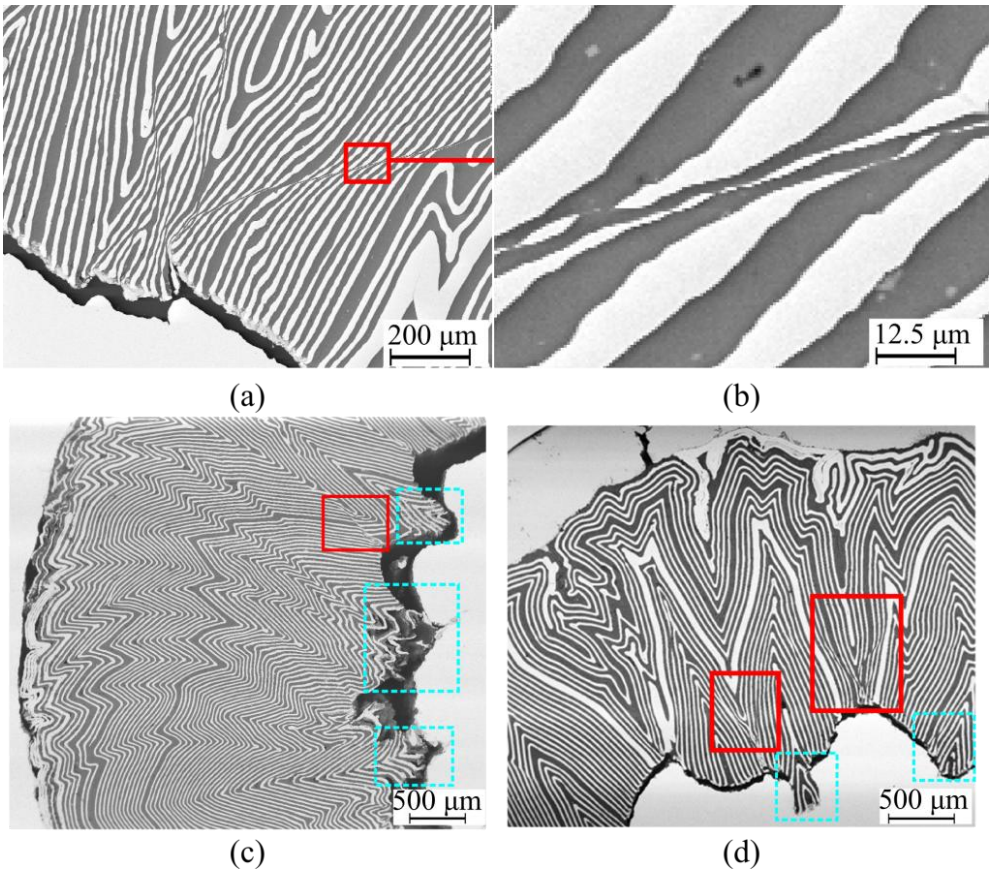

Figure 4.54 Two mesoscale mechanisms of the deformation accommodation in collapsed laminates samples – wedge extrusions and trans-layer shear bands spanning only a few layers are shown in (a), SW-6B and (b), SW-7C; a detailed view of the trans-layer shear band in SW-7A is shown in (c) and (d) and demonstrates the dramatic elongation and subsequent fracture of the Ni and Al layers within the shear zone. The Ni layers appear white and the Al layers appear dark grey.

Intermetallic reaction caused by the high strain plastic flow of Ni and Al within some of the trans-layer shear bands was observed in the areas away from the interface

with the copper stopper tube, as in the sample SW6-B (see Figure 4.55). The possible mechanism of reaction within these trans-layer shear bands consists of several steps. First, the localized high strain shearing within the trans-layer shear band elongates the Al and Ni layers (see Figure 4.54(b)) resulting in a reduction in the layer thicknesses by an order of magnitude. At some shear strain, the instability of the elongation process causes the layers to fragment. This provides a region in these shear zones where a mixture of small, sub-micron fragments of Al and Ni exist which, due to the reduction in bi-layer size, have a significantly lower temperature of ignition, approaching a minimum of 490 °K [20, 28]. Second, the localized heating caused by the high strain plastic flow inside the shear band allows for the reaction to develop. Third, because the Al and Ni layers outside the shear bands are significantly thicker than the elongated and fragmented layers inside the shear band, and since they are relatively cold due to a small strain plastic deformation, the reaction is quickly quenched and does not extend outside of the shear zone.

We did not observe propagation of reaction into the bulk of the laminates. However this dynamic plastic deformation can be used as preconditioning making Al-Ni laminates more susceptible for the bulk reaction initiation by subsequent shock loading.

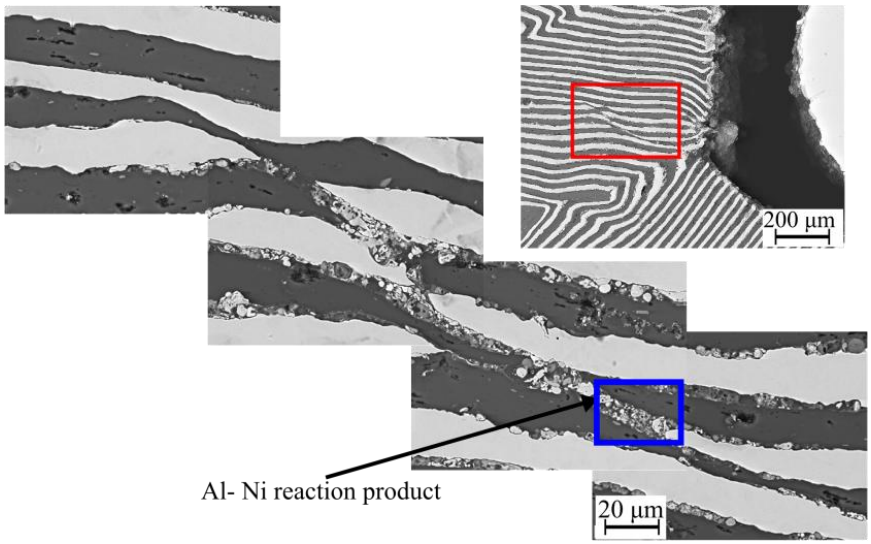

(a)

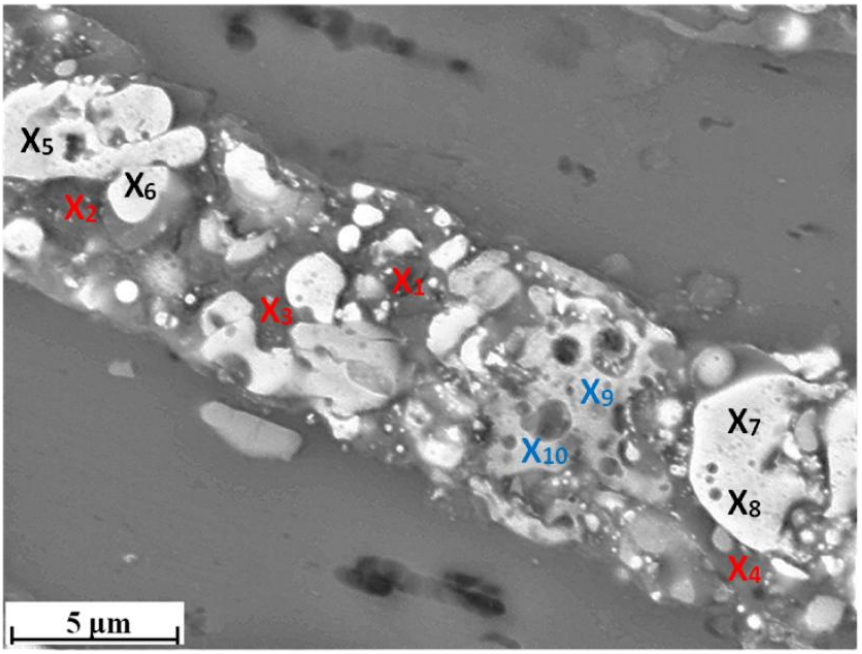

(b)

Figure 4.55 A detailed view of a local reacted trans-layer shear band in sample SW-6B (location is boxed in red). (b) A detailed view of the locations X1-X10 in the sample SW-6B (blue boxed region) where the EDX analysis was conducted showing Al-rich (X1-X4), Ni-rich (X5-X8), and Ni-Al (X9-X10) reaction products.

In addition to the high strain shear induced reaction observed in the trans-layer shear bands, the tips of Ni layers along the sample interface with the stopper tube

showed signs of bending and mushrooming from initially blunt tips with some degree of reaction (see Figure 4.56). This may be due to the presence of the initial gap between the sample and the copper stopper tube. At the initial stage of collapse, the sample closes the small air gap, colliding with the copper stopper tube, and the tips of the layers deformed during this impact in a fashion similar to Taylor bar samples [20, 28], developing localized plastic strain and increasing the local temperatures at the tips. Axial shearing at the sample-copper stopper tube interface may also contribute to the reaction initiation. Lastly, due to the small gap between the sample and the copper stopper tube, a high velocity jet of metals/air could develop, providing additional heating which is favorable for reaction initiation.

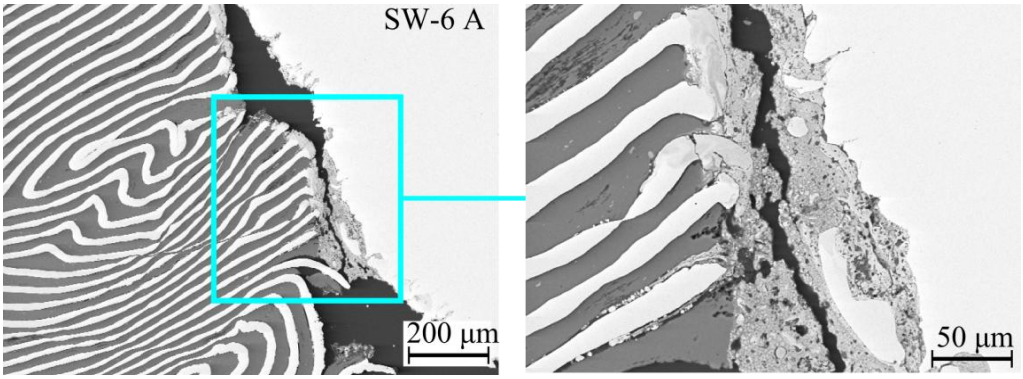

Figure 4.56 Bent and deformed Ni layers (compare the geometry of Ni layers in the initial sample in Figure 4.51 (b)), showing melting and localized reaction at the interface with copper stopper tube.

These mechanisms of reaction at the sample-copper stopper tube interface are the probable causes of full reaction in some of the wedge shaped regions (see Figure 4.57). It is interesting that the quenched reaction front in the wedges were contained within the very specific corrugated mesostructure of each wedge. This suggests that reactions were initiated in the wedges, after they were extruded by plastic flow, and

then they were rapidly quenched by adjacent, cold material. Localized reaction in these interfacial areas were probably due to boundary effects during initial impact and possible friction effects on later stages of deformation. We did not identify significant difference in their plastic deformation during collapse process which may explain their peculiar behavior. This mechanism of reaction initiation in the wedge shaped regions is beyond the scope of this dissertation, which focuses on deformation induced reaction.

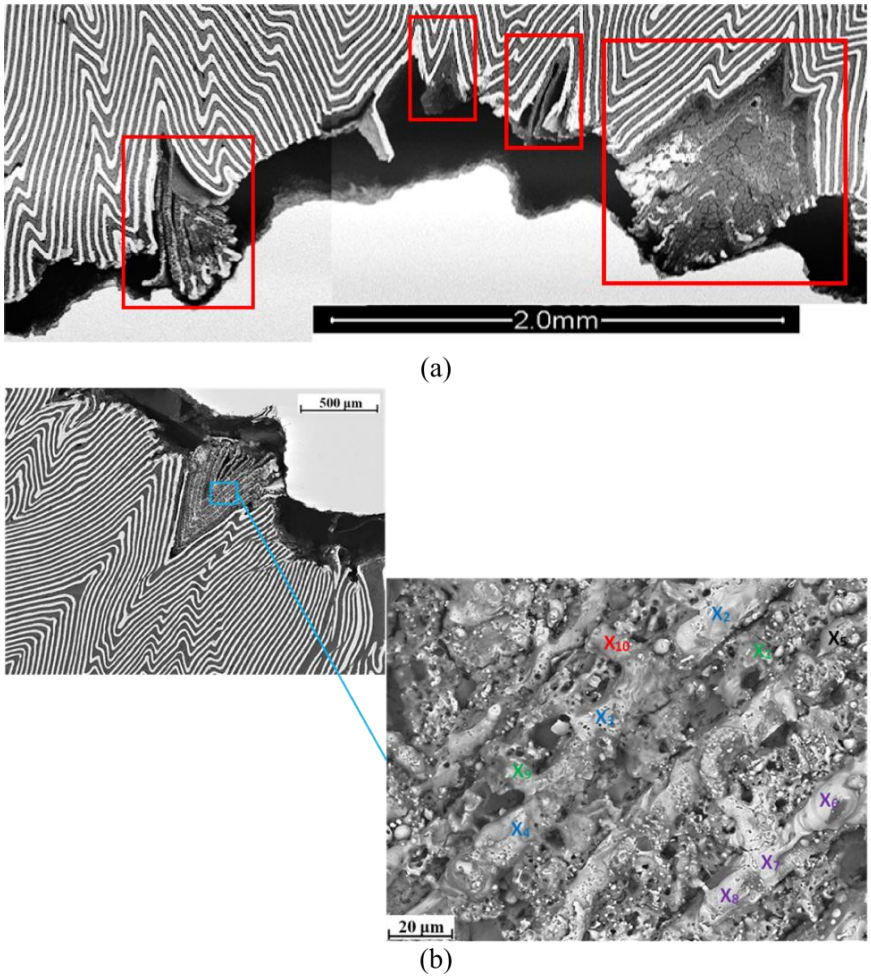

Figure 4.57 (a) Examples of localized reaction in some of the extruded wedge-shaped regions in SW-6 C (regions in the red boxes) showing the presence of an intermetallic reaction and (b) a reacted wedge in SW-6B with locations for EDX analysis identified.

The reactions in the Al-Ni system have been extensively investigated both theoretically and experimentally. Depending on the stoichiometry and morphology of Ni/Al reactants, fabrication methods, and ignition processes and conditions, the first phase to form in Al-Ni reaction has been reported to be Al_3Ni [20-22, 28-31], AlNi [32-34], Al_9Ni_2 [35, 36], or $AlNi_3$ [37, 38].

Energy-dispersive X-Ray spectroscopy (EDX) analysis was performed in the reacted trans-layer shear bands and the reacted wedges to determine the composition of the reaction products (locations examined are shown in Figure 4.55 (b) and Figure 4.57(b)). It revealed that the atomic ratio of Al/Ni varies from 0.3 to 6 in the reaction products in the reacted trans-layer shear bands and the reacted wedges. However, whether the detected elements e.g., Al or Ni, come from the remnants of original foils or belong to reaction products is not possible to identify in this method. X-ray diffraction was used to identify the product phase like Al_3Ni, NiAl, or $AlNi_3$, but the amount of reacted spots was too small to be analyzed.

This shows that both Ni-rich and Al-rich products exist in the reacted areas. In addition to the Al/Ni reaction products, the presence of a small amount of Cu was detected in some of the spots in the reacted wedges. This is likely due to the contact of the sample with the copper stopper tube. In the reacted shear band, significant amounts of oxygen were detected suggesting that an oxide layer formed in these zones. The EDX analysis showed 20~50 atomic percentage of oxygen is presented in the analyzed spots. Since the TWC assembly was not vacuum sealed, the oxygen is most likely come from air trapped during the explosive test.

Numerical simulations were performed using LS-DYNA, a general-purpose finite element program, under plane strain conditions. The geometry of the corrugated laminate used in the simulations was generated from an image of the mesostructure from sample SW-7A, which contains characteristic features representative of the overall corrugated mesostructures (i.e., large amplitude corrugations, interior facing wedge regions, small gaps between copper stopper tube and interior surface of the sample, and some locally coaxial layers). Details regarding the simulations can be found in [5, 39]. The deformed geometry and the temperatures of the simulated Al-Ni corrugated laminate at the moment of complete collapse are presented in Figure 4.58. The simulation captures the main features of plastic strain accommodation - wedge extrusion, trans-layer shear bands, and cooperative buckling.

Examination of the experimental specimens shown in Figure 4.53 and 4.54 and the simulation results shown in Figure 4.58 identified three major mechanisms of plastic strain accommodation – (1) the extrusion of interior facing wedge-shaped regions on the interior surface of the laminate, (2) local/global trans-layer shear bands mainly in areas where the layers were oriented in the radial direction, and (3) the cooperative buckling of layers in layers that were locally concentric. This behavior is dramatically different in comparison with plastic strain accommodation during dynamic deformation of coaxial Ni-Al layers in identical conditions of loading [19].

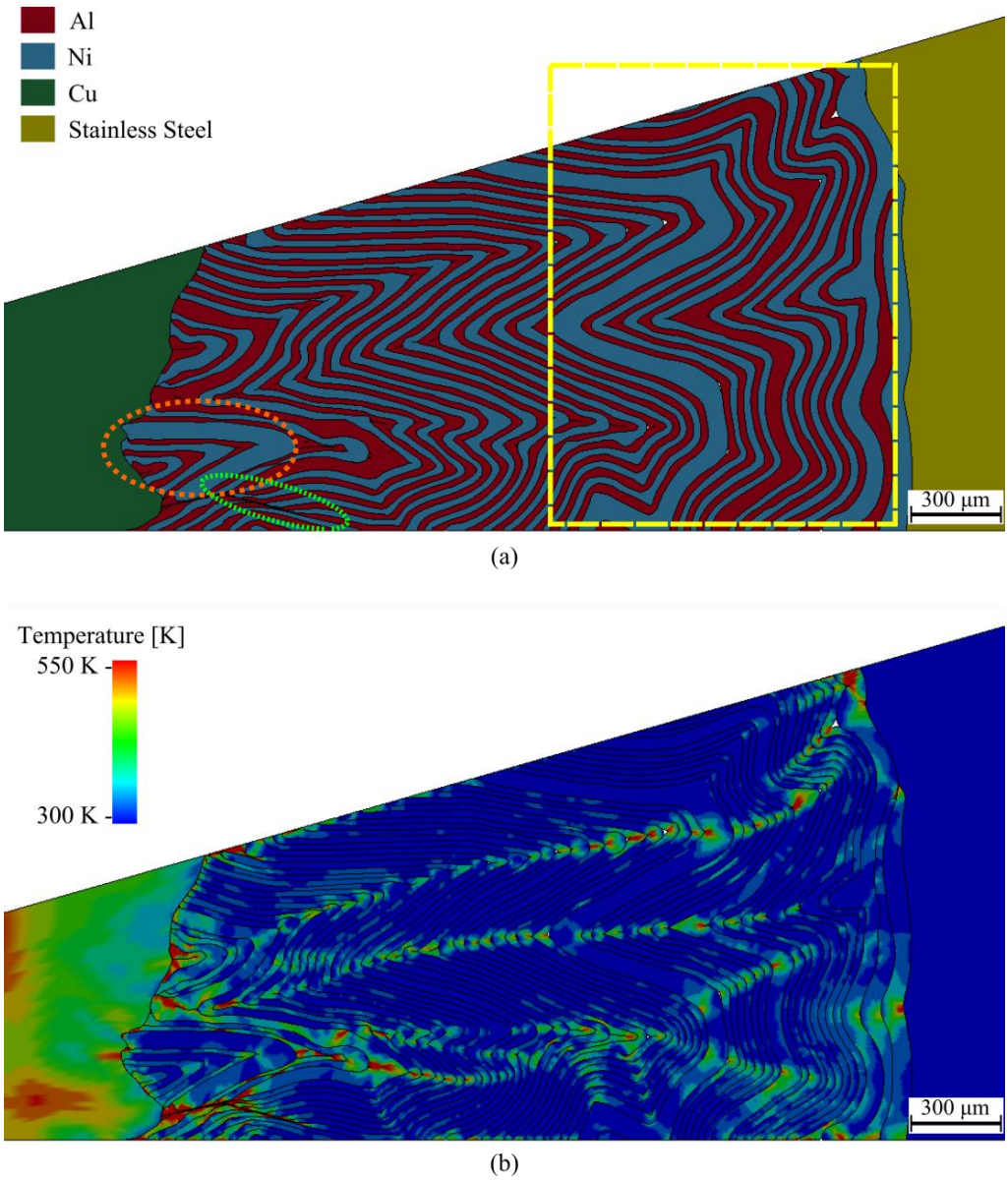

Figure 4.58 The deformed mesostructure (a) showing the three major mechanisms of plastic strain accommodation: (1) the extrusion of wedged shaped regions outlined by the orange dashed line, (2) the development of trans-layer shear bands outlined by the green dashed line, and (3) the cooperative buckling shown in the area outlined by the yellow dashed box. The temperatures at the moment of complete collapse are shown in (b). Elevated temperatures were observed in the apex regions throughout the sample and in the shear band at the bottom of the figure [39].

In the area where the layers on the interior of the sample are oriented more steeply towards the radial direction, a trans-layer shear band forms in numerical

calculations. The detailed view of this shear band in Figure 4.59 (a) shows a reduction of the layer thickness inside the trans-layer shear band similar to the one observed in the experimental sample (Figure 4.59 (b)). In addition, the temperatures in the shear band in the simulation are greater than 550 °K. In nano-sized Ni-Al laminates, reaction has been observed over a temperature range of 490—900 °K [20, 28] and calculated temperatures in the simulated shear bands are inside this range. Thus, we may assume that reaction initiation inside the shear band was deformation induced.

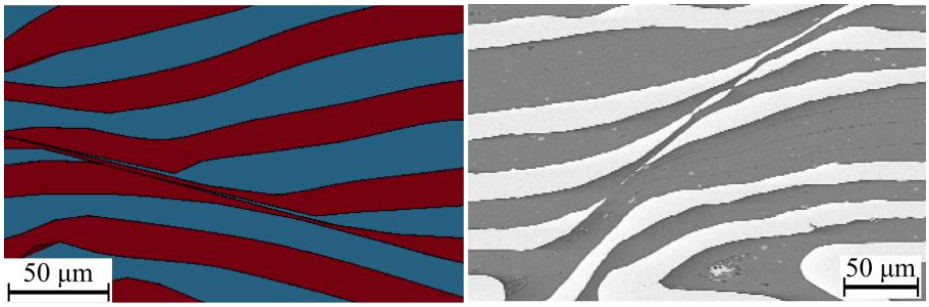

Figure 4.59 Comparison of elongated Al and Ni layers observed inside the trans-layer shear bands in the numerical simulation (a) and the experimental result corresponding to sample SW-7A (b). This elongation process may be the initial stage in the initiation of reaction within the shear bands shown in Figure 4.54(b) and Figure 4.55(a) [39].

The development of the trans-layer shear bands was observed mainly in the exterior facing wedge-shaped regions or in areas where the layers were more parallel to the radius (Figure 4.54). Within the trans-layer shear bands, Al and Ni layers were elongated, reducing their thickness by an order of magnitude (from approximately 15—20 microns to 0.75—1.5 microns), creating localized, fine, and micro-laminates. Additionally, in areas near the interior of the sample where the strains are large, some of these elongated layers fragment into sub-micron fragments. Both the elongation and fragmentation of the Al and Ni layers inside the shear bands provide favorable conditions for reactivity inside the shear bands. The thickness of the shear band is

approximately 10 microns with a shear displacement of approximately 200 microns, thus the shear strain is about 20.

In addition to the local trans-layer shear bands, sample SW-6A contains a global shear band, defined as a shear band that traverses the entire width of the sample (Figure 4.53(a)). In the global shear band, we do not observe any layer elongation or thinning. This global shear band radiates from the interior of the sample with an angle of ~45^{o} with the radial direction. This orientation is similar to the global shear bands observed in homogeneous and granular materials [6].

The simulations provided insight into the other details of the development of the plastic strain accommodation during the TWC tests. As the sample initially collapses, the porosity is squeezed from the sample and the gap between its inner surface and the copper stopper tube is closed. As the collapse progresses, the increase in the compressive hoop strains in the interior of the sample causes the wedge shaped regions, that are oriented at a slanted angle from the radial direction, to become extruded into the inner copper tube due to the slipping of the Ni-Al interfaces and also due to the localized plastic shearing of the Al in the slanted layers.

The extrusion of the interior facing wedges appears to be a unique mesoscale mechanism that accommodates plastic strain in these corrugated laminates. This mechanism of high strain plastic flow accommodation observed in the corrugated laminates is qualitatively analogous to the plastic flow of monocrystals [26, 27]. In both cases, the planes of easy slip were activated first, controlling the overall flow of the material. In the case of Al-Ni laminates, these planes of easy slip were the Al

layers and the Al-Ni interfaces that were at an angle to the radius at a 45° inclination, serving as the boundaries of the extruded wedges.

The temperatures observed in the simulations (Figure 4.58(b)) showed that the layers in the interior wedges adjacent to the inner copper stopper tube had a temperature range of 320-500 ºK for the Ni, 350-590 ºK for the Al, and the maximum temperature on the outside surface of the copper stopper tube was 350-450 ºK. These deformation-induced temperatures due to radial collapse are small in comparison to the temperatures required for the initiation of intermetallic reactions in laminates with similar bi-layer thicknesses under static conditions, 500-900 ºK [22, 23]. As being mentioned above, one of the reasons for this localized reaction may be the interaction of Ni-Al laminates with the copper stopper interface during high strain, high strain rate plastic flow which is suggested by the presence of thin, reacted layers on this interface, as presented in Figure 4.57.

Simulations showed that in layers oriented nearly perpendicular to the radius (locally coaxial geometry), cooperative buckling appears to have been the prevalent mode of plastic strain accommodation, which was the dominant mode during the collapse of coaxial laminates [19]. This mode of deformation was difficult to characterize in the experimental samples due to the variation in the mesostructure in the axial direction, making it impossible to view the initial and corresponding final mesostructure at the same axial locations. However, we did observe some areas of locally coaxial layers in the initial mesostructures while we did not see any locally concentric areas in the collapsed mesostructures. Also, we observed that most of the apices in the collapsed sample were radially aligned similar to the radial alignment

observed in the concentric samples [19] with no evidence of random buckling of individual layers. This suggests that the cooperative buckling mechanism was also active in the corrugated samples. The outer regions of the simulated segment of the laminate sample showed that the dominant mechanism of plastic strain accommodation was similar to the cooperative buckling observed in the concentric laminate composites [19]. The pattern of buckling was heavily influenced by the corrugated mesostructure on the interior of the sample. Like the samples with concentrically aligned layers, the buckles that were generated were nearly radial in nature. In addition, the apex areas of the buckles showed similar increases in localized temperature as in the concentric samples. However, the observed temperatures were less than those observed in the simulations with concentric layers of similar nominal size, probably due to additional mechanisms of plastic strain accommodation present in corrugated laminates.

4.4.3 Summary

Explosively driven Thick Walled Cylinder experiments and their corresponding numerical simulations demonstrate that three main mechanisms of plastic strain accommodation triggered by instabilities, additionally to bulk distributed plastic flow, were active during the collapse of the Ni-Al corrugated laminate composite – (1) the extrusion of interior facing wedge-shaped regions on the interior surface of the laminate, (2) a small number of non-uniformly distributed local/global trans-layer shear bands, and (3) the cooperative buckling of layers that were initially locally concentric. These mechanisms compete with each other in accommodation of

high strain, high strain rate plastic flow and are dependent on the initial mesostructure of the corrugated samples. They acted to block the development of multiple uniformly distributed global shear bands that have been observed in all previously examined solid homogeneous materials and granular materials. The observed mesoscale mechanisms of plastic strain accommodation in corrugated laminates are qualitatively different in comparison with behavior of Ni-Al laminates with coaxial symmetrical layers and showed a correlation with the orientation of layers relative to the sample's radius. Some of the local trans-layer shear bands showed reaction between the Ni and Al enhanced by dramatic elongation and fragmentation of Ni and Al layers and temperature increases due to deformation. A few of the extruded wedge-shaped regions demonstrated reaction between the Ni and Al layers, forming Ni-rich and Al-rich reaction products. The reaction inside extruded wedge-shaped regions with geometry of reaction products coinciding with the geometry of deformed wedges possibly enhanced by a high velocity metals/air jet moving in the gap between copper stopper tube and the sample. The reaction initiated in these spots did not ignite the bulk of material demonstrating that these mesostructured Ni-Al laminates are able to withstand high strain, high strain rate deformation without reaction. Thus the dynamic plastic deformation can be used as preconditioning making Ni-Al laminates more susceptible for subsequent bulk reaction initiated by shock.

In this chapter, Section 4.1 contains materials that appear in DYMAT 9th International Conference on the Mechanical and Physical Behaviour of Materials under Dynamic Loading (2009) by Po-Hsun Chiu and V. F. Nesterenko, Section 4.2 contains materials that appear in AIP Conference Proceedings 1426 (1) (2012) by Po-

Hsun Chiu, C.W. Lee, and V. F. Nesterenko and in Journal of Physics Conference Series 500 (11) (2014) by Po-Hsun Chiu, K. L. Olney, C. Braithwaite, A. Jardine, A. Collins, D. J. Benson, and V. F. Nesterenko, Section 4.3 contains materials that appear in Applied Physics Letters 102 (24) (2013) by Po-Hsun Chiu, K. L. Olney, A. J. Higgins, M. Serge, D. J. Benson, and V. F. Nesterenko, and Section 4.4 contains materials that appear in Philosophical Magazine 94 (26) (2014) by K. L. Olney, Po-Hsun Chiu, A. Higgins, M. Serge, T. P. Weihs, G. M. Fritz, A. K. Stover, D. J. Benson, and V. F. Nesterenko. The dissertation author was the investigator and author of above papers.

References:

1. K. L. Olney, P.-H. Chiu, C. W. Lee, V. F. Nesterenko, and D. J. Benson, *Role of material properties and mesostructure on dynamic deformation and shear instability in Al-W granular composites.* Journal of Applied Physics, 2011. **110**(11): p. 114908.

2. J. Cai, V. F. Nesterenko, K. S. Vecchio, F. Jiang, E. B. Herbold, D. J. Benson, J. W. Addiss, S. M. Walley, and W. G. Proud, *The influence of metallic particle size on the mechanical properties of polytetraflouroethylene-Al-W powder composites.* Applied Physics Letters, 2008. **92**(3): p. 3.

3. E. B. Herbold, V. F. Nesterenko, D. J. Benson, J. Cai, K. S. Vecchio, F. Jiang, J. W. Addiss, S. M. Walley, and W. G. Proud, *Particle size effect on strength, failure, and shock behavior in polytetrafluoroethylene-Al-W granular composite materials.* Journal of Applied Physics, 2008. **104**(10): p. 11.

4. C. H. Braithwaite, A. L. Collins, B. Aydelotte, F. McKenzie, P.-H. Chiu, N. Thadhani, and V. F. Nesterenko, *Advances in the study of novel energetic materials.* Proc. 15th Seminar New Trends in Research of Energetic Materials, University of Pardubice, Czech Republic, 2012: p. 93-99.

5. K. L. Olney, "*The mechanisms of plastic strain accommodation and post critical behavior of heterogeneous reactive composites subject to dynamic*

loading ", Ph.D. dissertation in Department of Mechanical and Aerospace Engineering, University of California, San Diego, 2014

6. V. F. Nesterenko, *Dynamics of Heterogeneous Materials*. First ed. Shock Wave and High Pressure Phenomena. 2001, New York: Springer. 536.

7. J. Stokes, V. Nesterenko, J. Shlachter, R. Fulton, S. Indrakanti, and Y. Gu. *Comparative behavior of Ti and 304 stainless steel in a magnetically-driven implosion at the Pegasus-II facility*. in *Proc. of the 2000 Int. Conf. on Fundamental Issues and Applications of Shock-Wave and High-Strain-Rate Phenomena "EXPLOMET'2000*. 2001.

8. Z. Lovinger, A. Rikanati, Z. Rosenberg, and D. Rittel, *Electro-magnetic collapse of thick-walled cylinders to investigate spontaneous shear localization.* International Journal of Impact Engineering, 2011. **38**(11): p. 918-929.

9. Y. J. Chen, M. A. Meyers, and V. F. Nesterenko, *Spontaneous and forced shear localization in high-strain-rate deformation of tantalum.* Materials Science and Engineering a-Structural Materials Properties Microstructure and Processing, 1999. **268**(1-2): p. 70-82.

10. V. F. Nesterenko, M. A. Meyers, and T. W. Wright, *Self-organization in the initiation of adiabatic shear bands.* Acta Materialia, 1998. **46**(1): p. 327-340.

11. M. A. Meyers, V. F. Nesterenko, J. C. LaSalvia, and Q. Xue, *Shear localization in dynamic deformation of materials: microstructural evolution and self-organization.* Materials Science and Engineering a-Structural Materials Properties Microstructure and Processing, 2001. **317**(1-2): p. 204-225.

12. Q. Xue, V. F. Nesterenko, and M. A. Meyers, *Evaluation of the collapsing thick-walled cylinder technique for shear-band spacing.* International Journal of Impact Engineering, 2003. **28**(3): p. 257-280.

13. C. J. Shih, M. A. Meyers, and V. F. Nesterenko, *High-strain-rate deformation of granular silicon carbide.* Acta Materialia, 1998. **46**(11): p. 4037-4065.

14. C. J. Shih, V. F. Nesterenko, and M. A. Meyers, *High-strain-rate deformation and comminution of silicon carbide.* Journal of Applied Physics, 1998. **83**(9): p. 4660-4671.

15. V. F. Nesterenko, M. A. Meyers, and H. C. Chen, *Shear localization in high-strain-rate deformation of granular alumina.* Acta Materialia, 1996. **44**(5): p. 2017-2026.

16. V. F. Nesterenko, M. A. Meyers, H. C. Chen, and J. C. Lasalvia, *Controlled High-Rate Localized Sheer in Porous Reactive Media.* Applied Physics Letters, 1994. **65**(24): p. 3069-3071.

17. V. F. Nesterenko, M. A. Meyers, H. C. Chen, and J. C. Lasalvia, *The Structure of Controlled Shear Bands in Dynamically Deformed Reactive Mixtures.* Metallurgical and Materials Transactions A-Physical Metallurgy and Materials Science, 1995. **26**(10): p. 2511-2519.

18. H. C. Chen, V. F. Nesterenko, and M. A. Meyers, *Shear localization and chemical reaction in Ti-Si and Nb-Si powder mixtures: Thermochemical analysis.* Journal of Applied Physics, 1998. **84**(6): p. 3098-3106.

19. P.-H. Chiu, K. L. Olney, A. J. Higgins, M. Serge, D. J. Benson, and V. F. Nesterenko, *The mechanism of instability and localized reaction in the explosively driven collapse of thick walled Ni-Al laminate cylinders.* Applied Physics Letters, 2013. **102**(24).

20. E. Ma, C. V. Thompson, and L. A. Clevenger, *Nucleation and Growth during Reactions in Multilayer Al/Ni Films - the Early Stage of Al3 Ni Formation.* Journal of Applied Physics, 1991. **69**(4): p. 2211-2218.

21. K. Barmak, C. Michaelsen, and G. Lucadamo, *Reactive phase formation in sputter-deposited Ni/Al multilayer thin films.* Journal of Materials Research, 1997. **12**(1): p. 133-146.

22. L. Battezzati, P. Pappalepore, F. Durbiano, and I. Gallino, *Solid state reactions in Al Ni alternate foils induced by cold rolling and annealing.* Acta Materialia, 1999. **47**(6): p. 1901-1914.

23. F. Cardellini, G. Mazzone, A. Montone, and M. V. Antisari, *Solid-State Reactions between Ni and Al Powders Induced by Plastic-Deformation.* Acta Metallurgica Et Materialia, 1994. **42**(7): p. 2445-2451.

24. E. P. Degarmo, J. T. Black, and R. A. Kohser, *Materials and processes in manufacturing*. 9th ed. 2003, Hoboken, NJ: John Wiley & Sons.

25. H. D. Espinosa and B. A. Gailly, *Modeling of shear instabilities observed in cylinder collapse experiments performed on ceramic powders.* Acta Materialia, 2001. **49**(19): p. 4135-4147.

26. S. Nemat-Nasser, T. Okinaka, and V. Nesterenko, *Experimental observation and computational simulation of dynamic void collapse in single crystal copper.* Materials Science and Engineering a-Structural Materials Properties Microstructure and Processing, 1998. **249**(1-2): p. 22-29.

27. S. Nemat-Nasser, T. Okinaka, V. Nesterenko, and M. Q. Liu, *Dynamic void collapse in crystals: computational modelling and experiments.* Philosophical Magazine a-Physics of Condensed Matter Structure Defects and Mechanical Properties, 1998. **78**(5): p. 1151-1174.

28. G. M. Fritz, S. J. Spey, M. D. Grapes, and T. P. Weihs, *Thresholds for igniting exothermic reactions in Al/Ni multilayers using pulses of electrical, mechanical, and thermal energy.* Journal of Applied Physics, 2013. **113**(1).

29. A. S. Edelstein, R. K. Everett, G. Y. Richardson, S. B. Qadri, E. I. Altman, J. C. Foley, and J. H. Perepezko, *Intermetallic Phase-Formation during Annealing of Al/Ni Multilayers.* Journal of Applied Physics, 1994. **76**(12): p. 7850-7859.

30. H. Sieber, J. S. Park, J. Weissmuller, and J. H. Perepezko, *Structural evolution and phase formation in cold-rolled aluminum-nickel multilayers.* Acta Materialia, 2001. **49**(7): p. 1139-1151.

31. X. Qiu and J. Wang, *Experimental evidence of two-stage formation of Al3Ni in reactive Ni/Al multilayer foils.* Scripta Materialia, 2007. **56**(12): p. 1055-1058.

32. C. T. Wei, V. F. Nesterenko, T. P. Weihs, B. A. Remington, H. S. Park, and M. A. Meyers, *Response of Ni/Al laminates to laser-driven compression.* Acta Materialia, 2012. **60**(9): p. 3929-3942.

33. C. Michaelsen, G. Lucadamo, and K. Barmak, *The early stages of solid-state reactions in Ni/Al multilayer films.* Journal of Applied Physics, 1996. **80**(12): p. 6689-6698.

34. C. T. Wei, B. R. Maddox, A. K. Stover, T. P. Weihs, V. F. Nesterenko, and M. A. Meyers, *Reaction in Ni-Al laminates by laser-shock compression and spalling.* Acta Materialia, 2011. **59**(13): p. 5276-5287.

35. K. J. Blobaum, D. Van Heerden, A. J. Gavens, and T. P. Weihs, *Al/Ni formation reactions: characterization of the metastable Al9Ni2 phase and analysis of its formation.* Acta Materialia, 2003. **51**(13): p. 3871-3884.

36. M. H. D. Bassani, J. H. Perepezko, A. S. Edelstein, and R. K. Everett, *Initial phase evolution during interdiffusion reactions.* Scripta Materialia, 1997. **37**(2): p. 227-232.

37. O. Arkens, L. Delaey, J. De Tavernier, B. Huybrechts, L. Buekenhout, and J. Libouton, *Dynamic compaction and hot-isostatic-pressing of nickelaluminides.* MRS Proceedings, 1988. **133**.

38. I. Song and N. N. Thadhani, *Shock-Induced Chemical-Reactions and Synthesis of Nickel Aluminides.* Metallurgical Transactions a-Physical Metallurgy and Materials Science, 1992. **23**(1): p. 41-48.

39. K. L. Olney, P. H. Chiu, A. Higgins, M. Serge, T. P. Weihs, G. M. Fritz, A. K. Stover, D. J. Benson, and V. F. Nesterenko, *The mechanisms of plastic strain accommodation during the high strain rate collapse of corrugated Ni–Al laminate cylinders.* Philosophical Magazine, 2014. **94**(26): p. 3017-3035.

CHAPTER 5 CONCLUSIONS

Two types of heterogeneous reactive materials, Al-W composites and Al-Ni laminates with different mesotructures were investigated. Each type of materials has the same composition (23.8 wt% of Al and 76.2 wt% of W for Al-W composites and 31.5 wt% of Al and 68.5 wt% of Ni for Al-Ni laminates) with different mesostructures with the goal to tailor their static, dynamic responses and fracture patterns (e.g., coarse vs. fine W particles, bonded vs. non-bonded Al particles, W particles vs. W wires and concentric vs. corrugated structures). The majority of investigated materials were fabricated in house at UCSD.

For Al-W granular/porous composites, the reinforcing W phase (particles or wires) was randomly distributed in the Al matrix to obtain the isotropic property of materials. The mixture of Al and W powder/fibers was ball milled first to break the agglomeration and after that was consolidated by CIPing to achieve high density and high-accurate dimensions. Subsequent HIPing was carried out to bond the Al particles. The quasistatic and dynamic testing results were presented.

For the W particulate-reinforced Al granular/porous composites, following major features were observed: (1) Samples with fine W powder after CIPing has higher porosity due to the higher resistance of agglomerated fine W particles during the densification; (2) The dynamic fracture of Al-W samples was due to axial cracks; (3) Maximum compressive stress of samples with fine W particles is higher than the corresponding stress of samples with coarse W particles at the same porosity; (4) Peak

compressive stress in dynamic testing was higher than in quasistatic tests due to *in situ* densification in dynamic conditions prevailing over fracture kinetics. Both (1) and (3) can be explained by the influence of the "force chains" created by fine W particles which were less effective with large W particles. Fine W particles are able to maintain the network supporting "force chains" which can rearrange themselves and support the compressive load even on the stage of macrocracking developing in materials.

The W fiber-reinforced Al granular/porous composites exhibited a qualitatively different behavior with respect to shear localization depending on the bonding between Al particles. CIPed only samples showed the resistance to shear localization probably due to in-situ densification and strain hardening of Al particles in both quasistatic and dynamic tests. As long as solid density is reached, the local shear instability starts to develop. On the other hand, CIPed+HIPed samples at similar global strains showed the development of macro shear bands and the formation of macrocracks in both quasistatic and dynamic tests due to the heavy deformation of Al matrix. The bonding between soft Al particles clearly facilitated the shear localization in both quasistatic and dynamic tests.

Solid Al-W-wires "mesh" composites fabricated using CIPing+HIPing from thin Al tubes and W wires periodically oriented in the axial and hoop directions were prepared and dynamically tested. The W mesh-reinforced samples showed highest dynamic compressive strength among the Al-W composites tested. It was experimentally demonstrated that the successful heat treatment of the Al-W composites was possible without the reaction between Al and W. This allowed

bringing the Al matrix back to T6 condition and thus increasing the dynamic compressive strength by 19%.

Another dynamic test, explosively driven expanding ring experiments were conducted with both W particulate- and fiber-reinforced Al granular/porous composite rings. The goal is to examine the mechanisms of fragmentation, characteristic fragment sizes and variations of these with respect to the initial mesostructure (coarse Al vs. fine Al particles, W powder vs. W wires, and bonded vs. unbounded Al particles). The porous/granular samples were mostly (above 90%) pulverized into fragments sizes below 100 micron for all tested mesostructures. Compared to the SS304 rings, which have the similar density, under identical conditions of explosive loading/strain and strain rates, the mesostructural features of granular composite dramatically change the fragmentation pattern. Some of the low strength Al particles were deformed between the rigid W particles, but mainly maintained their equiaxed shape in the areas away from W particles. Al particles were heavily deformed in samples with W rods regardless of the Al particle size and bonding between Al particles. The similar behavior in PDV records for the samples with W rods suggests that the global response is insensitive to the mesoscale properties of the Al. No intermetallic reaction between Al and W in the recovered fragments was observed.

For Al-Ni concentric laminates, a dramatic difference in mechanisms of plastic strain accommodation at similar global strain and strain rates was observed for samples with different thickness of layers. Numerical modeling was used to elucidate the mechanisms of plastic strain accommodation in the dynamic collapse of Ni-Al laminate materials and it showed good agreements with experimental results. Three

main mechanisms of plastic strain accommodation depending on bilayers sizes were observed in the concentric Al-Ni laminates: (1) cooperative buckling for Sample 1 (bilayers thickness = 63.5μm); (2) kink bands with low amplitude buckling in-between for Sample 2 (bilayers thickness = 18.5μm); and (3) uniform plastic flow for Sample 3A (bilayers thickness = 620.0μm). Sample 3B showed randomly distributed defects only had a relatively minor local influence on the order of the layer thickness.

For Al-Ni corrugated laminates, TWC experiments and their corresponding numerical simulations demonstrated that three main mechanisms of plastic strain accommodation are active during the collapse of the Al-Ni corrugated laminate composite – (1) the extrusion of interior facing wedge-shaped regions on the interior surface of the laminate, (2) a small number of non-uniformly distributed local/global trans-layer shear bands, and (3) the cooperative buckling of layers that were initially locally concentric. They are triggered by instabilities in addition to the bulk distributed plastic flow. These mechanisms compete with each other in accommodation of high strain, high strain rate plastic flow and are dependent on the initial mesostructure of the corrugated samples. They block the development of multiple uniformly distributed global shear bands that have been observed in previously examined solid homogeneous materials and granular materials. Some of the local trans-layer shear bands showed reaction between Al and Ni enhanced by the temperature increases due to the dramatic elongation and fragmentation of Al and Ni layers. A few of the extruded wedge-shaped regions also demonstrated reaction between Al and Ni layers, forming Ni-rich and Al-rich reaction products. This is possibly enhanced by a high

velocity metals/air jet moving in the gap between the copper stopper tube and the sample.

The observed mesoscale mechanisms of plastic strain accommodation in corrugated laminates are qualitatively different in comparison with the behavior of concentric laminates. The localized reaction did not ignite the bulk of materials demonstrating that both concentric and corrugated Al-Ni laminates are able to withstand high strain, high strain rate deformation without the global reaction. Thus, the dynamic plastic deformation can be used as preconditioning making Ni-Al laminates more susceptible for subsequent bulk reaction initiated by shock.

Both investigated heterogeneous reactive materials, Al-W composites and Al-Ni laminates, showed promising trends to fulfill our goals. In the case of Al-W composites, soft Al particles were heavily deformed between the rigid W particles/wires during dynamic tests. The localized damages can accumulate and then subsequently grow into the meso/macro shear bands/cracks. Through the bulk distributed fractures, small Al particles with fresh surfaces can be created by the *in situ* fragmentation. In the case of Al-Ni laminates, different plastic strain accommodation mechanisms, which depend on the initial mesostructure, are observed. While they may compete with each other during the plastic deformation, they can all serve as possible "hot spots" for the ignition of intermetallic reactions.

This chapter contains materials that appear in DYMAT 9th International Conference on the Mechanical and Physical Behaviour of Materials under Dynamic Loading (2009) by Po-Hsun Chiu and V. F. Nesterenko, in AIP Conference Proceedings 1426 (1) (2012) by Po-Hsun Chiu, C.W. Lee, and V. F. Nesterenko, in

Journal of Physics Conference Series 500 (11) (2014) by Po-Hsun Chiu, K. L. Olney, C. Braithwaite, A. Jardine, A. Collins, D. J. Benson, and V. F. Nesterenko, in Applied Physics Letters 102 (24) (2013) by Po-Hsun Chiu, K. L. Olney, A. J. Higgins, M. Serge, D. J. Benson, and V. F. Nesterenko, and in Philosophical Magazine 94 (26) (2014) by K. L. Olney, Po-Hsun Chiu, A. Higgins, M. Serge, T. P. Weihs, G. M. Fritz, A. K. Stover, D. J. Benson, and V. F. Nesterenko. The dissertation author was the investigator and author of above papers.